ENCODED HYDROGEL MICROPARTICLES FOR HIGH-THROUGHPUT MOLECULAR DIAGNOSTICS AND PERSONALIZED MEDICINE

by

STEPHEN CLIFFORD CHAPIN

B.S. Chemical Engineering, Yale University (2007)

Submitted to the Department of Chemical Engineering
in partial fulfillment of the requirements for the degree of

Doctor of Philosophy in Chemical Engineering

at the

MASSACHUSETTS INSTITUTE OF TECHNOLOGY

June 2012

Signature of Author_____
Department of Chemical Engineering
May 7, 2012

Certified by_____
Patrick S. Doyle
Professor of Chemical Engineering
Thesis Supervisor

Accepted by_____
Patrick S. Doyle
Professor of Chemical Engineering
Chairman, Committee for Graduate Students

Abstract

Encoded Hydrogel Microparticles for High-throughput Molecular Diagnostics and Personalized Medicine

by
Stephen Clifford Chapin

Submitted to the Department of Chemical Engineering on May 7th, 2012,
in partial fulfillment of the requirements for the degree of
Doctor of Philosophy in Chemical Engineering

The ability to accurately detect and quantify biological molecules in complex mixtures is crucial in basic research as well as in clinical settings. Advancements in genetic analysis, molecular diagnostics, and patient-tailored medicine require robust detection technologies that can obtain high-density information from a range of physiological samples in a rapid and cost-effective manner. Compared to conventional microarrays and methods based on polymerase chain reaction (PCR), suspension (particle-based) arrays offer several advantages in the multiplexed detection of biomolecules, including higher rates of sample processing, reduced consumption of sample and reagent, and rapid probe-set modification for customizable assays. This thesis expands the utility of a novel hydrogel-based microparticle array through (1) the creation of a microfluidic, flow-through fluorescence scanner for high-throughput particle analysis, (2) the development of a suite of techniques for the highly sensitive and specific detection of microRNA (miRNA) biomarkers, and (3) the investigation of new methods for directly measuring biomolecules at the single-cell level.

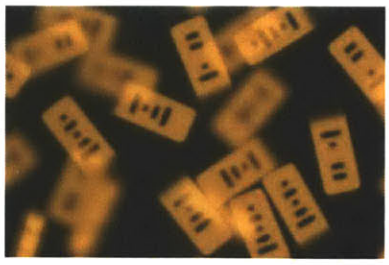

Graphically-encoded hydrogel microparticles synthesized from non-fouling, bioinert poly(ethylene glycol) (PEG) and functionalized with biomolecule probes offer great promise in the development of high-performance, multiplexed bioassays. To extend this platform to applications in high-throughput analysis, particle design was optimized to ensure mechanical stability in high-velocity flow systems, and a single-color microfluidic scanner was constructed for the rapid fluorescence interrogation of each particle's spatially-segregated "code" and "probe" regions.

The detection advantages of three-dimensional, probe-laden hydrogel scaffolds and the operational efficiencies of suspension array technology were then leveraged for the rapid multiplexed expression profiling of miRNA. The graphical encoding method and ligation-based labeling scheme implemented here allowed for scalable multiplexing with a simple workflow and an unprecedented combination of sensitivity, flexibility, and throughput. Through the rolling circle amplification of a labeling oligonucleotide, it was possible to

further enhance the system's sensitivity and resolve single-molecule miRNA binding events on particle surfaces, enabling the first direct detection of low-abundance miRNA in human serum without the need for RNA extraction or target amplification. Finally, by arraying cells and gel particles in polydimethylsiloxane (PDMS) microwells, it was possible to dramatically improve the particles' target capture efficiency and thereby move closer to a regime in which miRNAs and other biological molecules may be directly detected without target amplification from single cells.

Thesis Supervisor: Patrick S. Doyle

Title: Professor of Chemical Engineering

Acknowledgments

A Ph.D. is a long yet rewarding journey that uncovers at least as many truths about one's self as the area of research under investigation. There are oceans of data, valleys of disappointment, deserts of stagnation, and occasionally, oases of success. It would be impossible to negotiate the many obstacles of a Ph.D. without a support network, and I count myself lucky to have been blessed with one of the strongest. I would like to take this opportunity to extend my thanks to the individuals who have played significant roles, directly or indirectly, in my writing of this thesis.

Thank you to my parents, Nancy and Cliff, for instilling within me a drive to succeed but also a sense of perspective, both of which proved indispensable over the last five years. Yvonne, from the summits of volcanoes in Iceland to the bottoms of canyons in Peru, you have been by my side every step of the way during my Ph.D., and your constant encouragement and positive attitude have been integral to my successes. To my extended family, thank you for the support and wisdom you have imparted to me over the years, particularly during holiday meals and the epic dessert sessions that follow.

To Professor Doyle, thank you for the opportunity to work in your group and for the invaluable lessons you have taught me about designing experiments, managing research goals, and analyzing complex problems. I owe a great deal of gratitude to Dr. Daniel Pregibon, who initiated the encoded hydrogel microparticle project and whose early mentorship was absolutely crucial to my development as a researcher. I would be remiss if I did not also extend a heartfelt thank you to Dr. David Appleyard, Dr. Nakwon Choi, and

Rathi Srinivas, whose patience, optimism, and dedication helped to expand the encoded microparticle project and to make 66-053 a better place to work.

Ki Wan, I genuinely enjoyed every minute of our collaborations, and your enthusiasm provided much needed sunshine in our windowless basement laboratory during many long days of experimentation. Our frequent MIT tunnel walks, lab soccer sessions, and paper airplane contests were always wonderful diversions from the challenges of the Ph.D. program. Byron and Justin, thank you for listening to my ramblings during our many lunch meetings, even if you never accepted the reality that the New England Patriots were the best team in the NFL during our tenure in graduate school. Jon, you were a model roommate on Chauncy Street, and I always appreciated your input on all topics that our conversations touched upon. Matt, our two-man trivia teams were a welcome respite every Wednesday night from the hectic workweek. I would also like to say thank you to Josh, Adel, Dae Kun, Gil, Haskos, Defran, Sandeep, Karlo, Gus, and Ralph for being such great friends.

Table of Contents

List of Figures

List of Tables

Chapter 1

Introduction

The work presented in this thesis focuses on the development of a hydrogel-based microparticle array for the multiplexed detection of biological molecules in both clinical and research settings. There is a strong need for flexible biomolecule analysis platforms that can rapidly and precisely quantify low levels of multiple target molecules in a range of biological media for applications in diagnostics and personalized medicine. These systems have the potential to transform existing disease treatment models by enabling researchers to better understand the molecular basis of disease and thereby develop safer, more effective therapeutic interventions. This chapter outlines (1) the existing strategies employed for multiplexed biomolecule detection, (2) the emerging clinical significance of micro-ribonucleic acid (miRNA) profiling, and (3) the microfluidic advances that have enabled the creation of graphically-encoded hydrogel microparticle arrays.

1.1 Multiplexed Biomolecule Analysis

The accurate detection and quantification of specific biological molecules in a complex mixture is crucial in both basic research and clinical settings. The advancement of the emerging fields of personalized genomics and proteomics requires robust technologies that can obtain high-density information from biological samples in a rapid and cost-effective manner [1-6]. High-throughput screening for genetic analysis and clinical diagnostics benefits greatly from multiplexed analysis, which is the simultaneous detection of several different analytes ("targets") in a single test [7, 8]. While this approach significantly

reduces the required assay time, sample volume, and cost, it also introduces the need for an encoding scheme that can be used to identify the multiple types of capture ("probe") molecules employed in the assay. Through such identification, the encoding scheme enables the reporting signal from a given probe to be correlated to the expression level of the appropriate target molecule during post-assay data analysis.

1.1.1 Planar Arrays

High-throughput multiplexed biological assays emerged in the late 1980s with the introduction of high-density oligonucleotide microchips (planar arrays) created using technologies adapted from the semiconductor industry [7, 9]. To profile multiple deoxyribonucleic acid (DNA) targets in a single assay, these arrays relied on a positional encoding scheme in which each probe molecule type was attached to a distinct site on the array using precise photolithographic techniques or robotic spotting. In a typical workflow, after a sample was incubated with the chip and pre-labeled target had bound to the probe molecules, laser confocal fluorescence scanning would be employed to interrogate the molecular binding events at specific sites of the array to provide data on the abundance of hundreds to thousands of different targets of interest. Within the nucleic acid research community, this planar array format quickly replaced conventional assay systems such as enzyme assays and DNA reverse dot blots. The older methods required repetitive manual labor and large amounts of reagents, while the chip-based platform's miniature scale (10^6 synthesis sites/cm^2) and ease of automation enabled cheaper, more rapid analysis.

During the mid-1990s, the explosion in genomic research led to the widespread use of the chip platform in large-scale DNA sequence analysis. As a result, the format has been thoroughly studied and many steps have been taken to optimize the duplex formation of oligonucleotides on solid microchips as a means to increase the efficiency and accuracy of sequencing by hybridization (SBH), gene expression analysis, and mutant diagnostics [10, 11]. By varying probe design, immobilization chemistry, and hybridization conditions, researchers sought to minimize the amount of input sample required for reliable target detection (high sensitivity) and to minimize the capture of unintended targets by immobilized probes (high specificity). In addition to fluorescent reporting schemes, nanomechanical [12], surface plasmon resonance (SPR) [13], and colorimetric [14] strategies have been employed for target quantification on microarrays for a range of applications (Figure 1.1). Through the attachment of antibody probes and other binding motifs such as DNA and RNA aptamers, the platform has also been successfully adapted for numerous applications in protein profiling and screening [15-17].

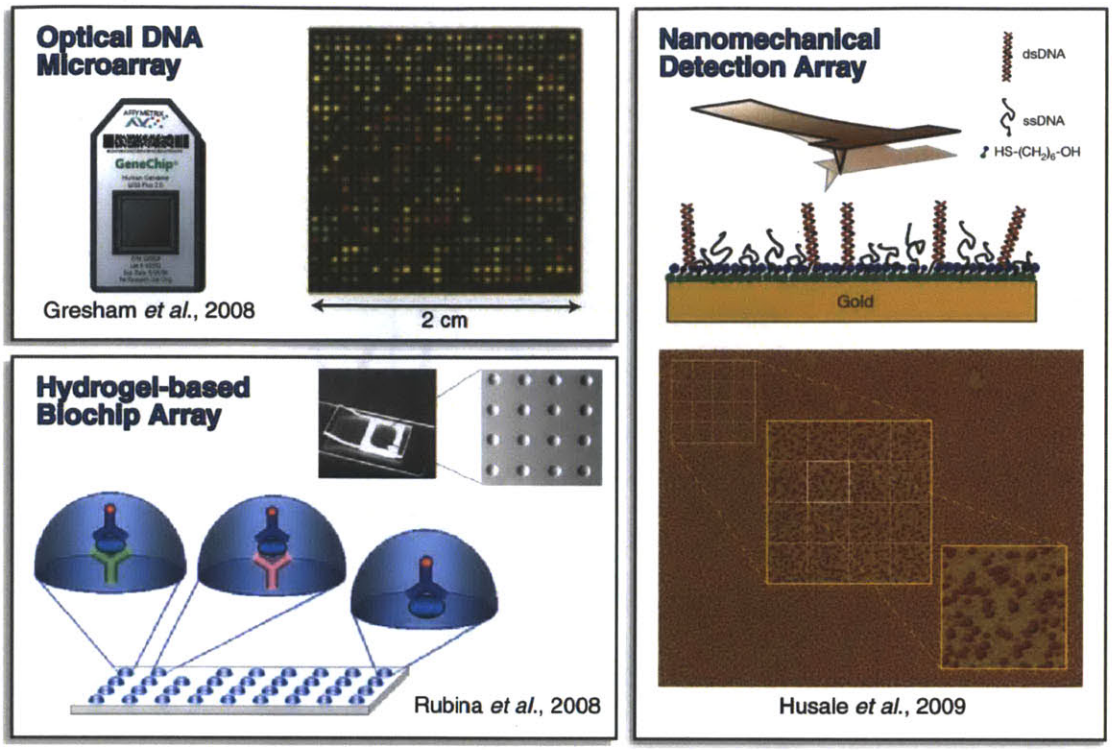

Figure 1.1: *Examples of planar array formats used for biomolecule detection. The DNA microarray with fluorescence readout is the most common implementation [18]. A range of other formats have also been developed, including arrays with hydrogel-based detection pads [19] and ultrasensitive arrays that can detect single-molecule binding events with nanomechanical measurements [12].*

The most significant factor in determining the sensitivity and specificity of a detection system is the dissociation constant (K_d) of the target-probe complex, which is dictated by the nature of the molecules that form the complex as well as the local environment in which the binding takes place. The dissociation constant for a system with target T, probe P, and target-probe complex TP is the ratio of their concentrations at equilibrium:

$$K_d = \frac{[T][P]}{[TP]} \qquad \text{Equation 2.1}$$

It is well known that biomolecule probes immobilized on solid surfaces such as those used in conventional microarrays exhibit less favorable (higher) dissociation constants than probes that are allowed to bind to targets in solution. This is primarily due to the additional energy cost incurred for the transfer of target molecules into the dense probe "forests" that are formed on the solid surface. To improve binding affinity researchers have tested a variety of different "spacer" sequences for probe immobilization and have also developed locked nucleic acid (LNA) probes, which are modified oligonucleotides containing a bridge between the 2' oxygen and the 4' carbon that is designed to augment target-probe complex

stability [20]. In a more radical departure the Mirzabekov group introduced hydrogel-based immobilized microarrays of gel elements (IMAGE) [10, 21-23]. These modified arrays achieved higher sensitivity and specificity than solid microarrays by using hydrated, three-dimensional gel pads to increase probe loading capacity and provide a more solution-like (and thus more thermodynamically-favorable) environment for target capture (Figure 1.2).

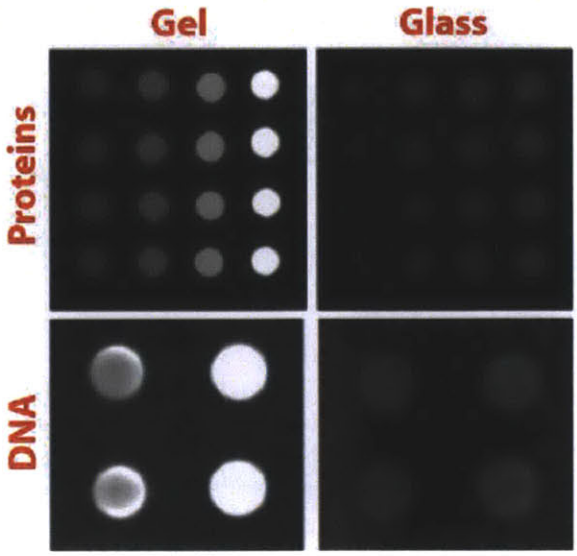

Figure 1.2: *Comparison of gel-based and glass-based microarrays for the detection of protein and DNA targets [24, 25].*

While the microarray platform and its variants have proven useful for large-scale screening and ultra-high-density discovery applications, their limitations have become apparent as researchers and clinicians push towards an era of cost-effective diagnostic and therapeutic practice tailored to the genetic signatures of individual patients. The high degree of multiplexing capacity available on a microarray is not always necessary, particularly when interrogating small, focused target panels for medical applications. The long incubation times (12–24 h) required for highly sensitive results on microarrays can also be difficult to integrate into workflows designed to process hundreds of samples per day. Furthermore, the complexity of array fabrication and the high cost associated with deploying the platform can often prevent its adoption in low-resource research and clinical environments.

1.1.2 Particle Arrays

Suspension (particle-based) arrays have been developed in recent years as an alternative to planar arrays for situations in which a modest number of targets (<1000) need to be detected over large populations of patients or for applications in which rapid probe-set modification is required [26]. The use of micrometer-sized particles for detection has many advantages over planar microarrays, including the ability to use smaller sample volumes,

faster probe-target binding kinetics due to mixing during incubation, and more efficient separation and washing steps. Microparticles can be quickly and inexpensively produced in large numbers and with high reproducibility to limit batch-to-batch variations in assay performance. Suspension arrays can use optical (spectrometric) [27, 28], chemical [29], graphical [30-35], radio frequency [36], shape [37-39], or physical [26] encoding schemes to carry out multiplexed analysis, and additional targets can be detected in a sample simply by adding microparticles bearing an appropriate code and probe molecules to the hybridization mixture (Figure 1.3). The incorporation of the same probe on many different microparticles in a single assay allows for thorough statistical scrutiny and ultimately provides high quality results. In contrast, the complex, often slow fabrication of planar arrays results in a lower degree of reproducibility and prevents the rapid design of new sets of probes for additional assays.

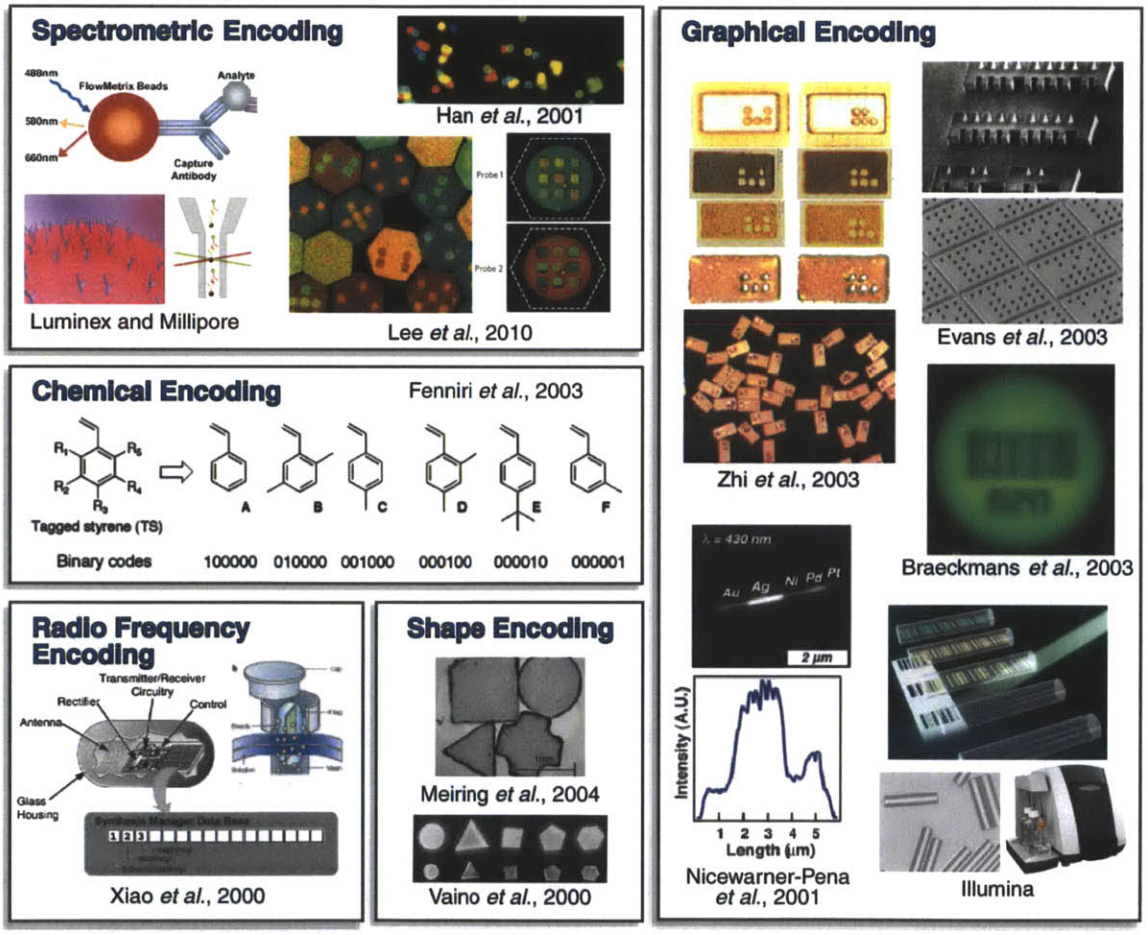

Figure 1.3: *Examples of encoding techniques for the multiplexed measurement of biomolecules on particle-based arrays. The methods shown here include spectrometric [28, 40-42], graphical [31-35], chemical [29], radio frequency [36], and shape [37-39] encoding.*

1.1.2.1 Fundamental Principles and Current Systems

For applications involving a low to medium density of targets (1–1000) and requiring high-throughput processing of samples, particle-based arrays offer many advantages over the more conventional planar arrays. This range of multiplexing is commonly required in clinical diagnostics and drug discovery, and over the last decade, several particle-based assays have been developed to detect and quantify soluble analytes in biological fluids [8, 27, 43-48]. The ideal particle is made of a low-density material that can be maintained in suspension without rapid settling so as to promote efficient interaction with soluble analytes. Furthermore, the ideal particle is small enough that a large collection of particles does not occupy more than one percent of the working volume during hybridization. However, it must be sufficiently dense and large to facilitate easy washing and separation by simple methods like centrifugal precipitation and filtration. Magnetic separation methods have also been employed [49]. The particle must be significantly larger than the reporter/probe molecules used in the assay to ensure sufficient loading of the particle for signal generation. In addition, the perfect microcarrier for the array would be able to be inexpensively and reproducibly manufactured in large batches using common reagents and materials.

The vast majority of particles used in suspension arrays are optically encoded latex microspheres with diameters between 0.3 and 10 μm that can be interrogated and decoded with laser-based flow cytometry [27, 50, 51]. Optical encoding is accomplished by swelling (or "doping") the latex spheres with fluorescent organic dyes with different emission spectra. It should be noted that there are several limitations to the number of distinct codes that can be achieved using this strategy. First and foremost, the dyes must be compatible with the solvents used in the swelling procedure and must be incorporated uniformly and reproducibly from batch to batch. Second, the excitation wavelengths of the reporter dyes need to be compatible with the excitation lasers available. Moreover, the encoding dyes must be chosen so that their emission spectra do not overlap with the spectra of the reporter dyes used to generate the optical signal used for quantification of analyte; such overlap can result in radiative and/or nonradiative energy transfer, thus increasing the difficulty of resolving encoding signals and requiring the employment of more sensitive and expensive decoding equipment [52].

The most prevalent commercially-available particle-based assay platform is the xMAP array technology sold by Luminex Corp (Austin, TX) [27]. This platform utilizes 5.6-μm diameter polystyrene microspheres doped with three dyes to generate 500 distinct sets of particles. Using this technology and associated flow analysis instruments (Luminex 100/200, FlexMAP 3D), researchers have reported successful multiplexed assays of single nucleotide polymorphisms (SNPs) [53], human cytokines [51], biological warfare agents [54], and kinases [55], with analyte concentrations as low as 100 attomolar able to be detected. While this system was the first particle-based array to truly challenge the dominance of microarrays, its current format suffers from several technical drawbacks,

including poor reproducibility, difficulty in utilizing the full coding capacity due to spectral overlap, and significant capital costs associated with the decoding and quantification instrument. It should be noted that a range of other commercial particle-based products have become available in the past decade, but the vast majority fail in at least one major way to achieve truly high-throughput analysis of medium density samples. For example, the Becton Dickinson Cytometric Assay is compatible with several conventional flow cytometers but is only capable of a 10-plex assay [56, 57]. Nanoplex Technologies, Inc. produces metal nanorods with gold and silver stripes that serve as a graphical code for multiplexing [33]. As mentioned earlier, the high density of the rods leads to rapid settling in solution and thus requires the rods to be vigorously mixed during assays, a procedure which can damage fragile biological molecules like antibodies. SmartBead Technologies Ltd markets graphically encoded aluminum rods that suffer from the same drawback [58].

Perhaps the most promising commercially-available particle system is Illumina's BeadXpress technology, which uses probe-laden glass cylinders (240 μm long, 28 μm in diameter) for high-throughput analysis with sensitivities that surpass those achieved with other solid bead systems [35, 59]. A 24-bit holographic code is embedded in each cylinder for probe identification, providing ultra-high coding capacity for multiplexing and for tracking samples and reagents used. The system has been extensively employed by a number of leading laboratories in recent years for genotyping, gene expression analysis, methylation analysis, and protein-based assays [35]. An accompanying analysis instrument (BeadXpress Reader) maneuvers the beads into microchannels that can then be scanned with a translating laser, providing the ability to interrogate particles after assay at a rate of 80 samples/h for a 96-plex trial or 120 samples/h for a 10-plex trial [35].

1.1.2.2 Flow Cytometry for Particle Analysis

Many researchers have turned to flow cytometry for the efficient processing and decoding of the microparticles used in multiplexed biomolecule assays. Flow cytometry is the measurement of the physical and chemical properties of micron-scale bodies as they are carried past a detector in a fluid stream. The strength of cytometric analysis is its capacity to interrogate cells or particles on an individual basis rather than measuring the average values displayed by larger populations. Developed in the 1940s, the earliest cytometers were expensive, bulky, and largely confined to the research laboratory for the purpose of counting blood cells [60]. Improvements in micromachining and signal processing facilitated gradual reductions in size, and the current generation of instruments is able to fit on the bench top. In the past two decades flow cytometry has emerged as a crucial analytical tool in clinical laboratories for the high-throughput (40,000 objects/s) quantification of various characteristics of viruses, bacteria, cells, and microparticles. Researchers have employed cytometers to diagnose disease, characterize immunological states, monitor response to treatment, interrogate cell surfaces, and even detect and sort rare cell types [61].

Despite their impressive track record in the clinical setting, conventional cytometers have several drawbacks. They require relatively large sample and reagent volumes, time-consuming sample pre-treatment techniques, and specialized personnel for their daily operation [61]. Miniaturized microfluidic flow cytometers fabricated from silicon/glass and poly(dimethylsiloxane) (PDMS) elastomer were developed in response to these issues. The small dimensions of the microfluidic channels greatly reduce the required sample and reagent volumes, making the system ideal for applications such as the diagnosis of fetal genetic disorders and the screening of infant blood. The tight confinement of the fluids also ensures high surface-to-volume ratios for increased reaction times and can even aid in the detection scheme used to interrogate the objects of interest. Furthermore, many of the elastomer-based miniature cytometers are portable and inexpensive to manufacture on a large scale. As a result, several disposable cytometers have been developed and marketed for human immunodeficiency virus (HIV) screening and monitoring, cell screening assays, and blood analysis [60].

The primary challenge in flow cytometry is confining, or focusing, the cells and particles under investigation to a small region of the flow chamber for efficient and accurate detection (Figure 1.4). The simplest and most common method employs the pressure-driven flow of sheath fluids to hydrodynamically focus a central particle-bearing stream to a width comparable to the dimensions of the particles [62, 63]. A stream width larger than this will lead to the passage of multiple particles through the detection zone at the same time, thus complicating signal processing. Meanwhile, smaller stream widths are also unfavorable, as agglomeration of particles can occur. Since standard PDMS microfabrication methods employ two-dimensional patterns (in the x-y plane), the confinement of particles to a small length along the "z-axis" has often been problematic and has limited throughput. However, two different groups have reported the fabrication of PDMS microchannels capable of three-dimensional hydrodynamic focusing. Simonnet *et al.* used this advanced degree of focusing to create both a high-throughput device (17,000 particles/s) and a high-resolution device from a single cast of PDMS [62, 64]. Chang *et al.* cleverly configured two separate casts of PDMS to develop an even more robust three-dimensional focusing channel loosely based on Simonnet's results [65]. Because sheath strategies can lead to undesired sample dilution and higher waste volumes, silicon-based chips utilizing embedded fiber optic reflection probes rather than sheath streams have also been created [66]. Additional focusing methods employ vacuum pumps [67, 68], settling due to gravity [69], and electroosmotic-induced flow [70-72].

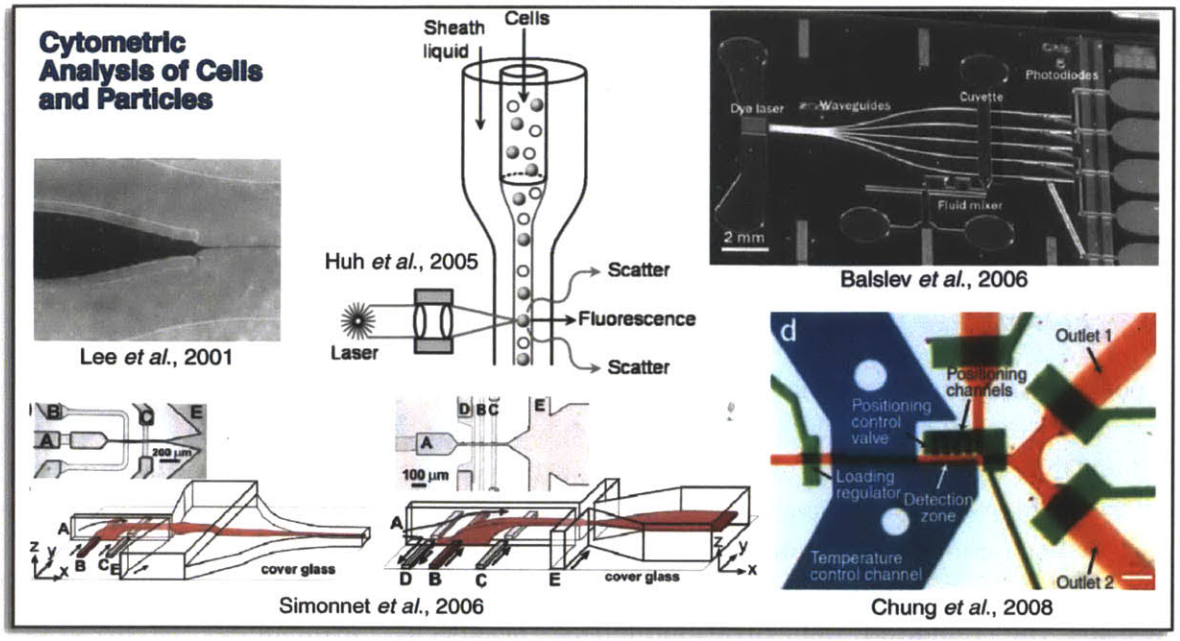

Figure 1.4: *Summary of cytometric systems used for the focusing and analysis of micron-scale bodies. Hydrodynamic focusing is commonly used to manipulate cells and microparticles into well-ordered flows so that they may be interrogated on an individual basis with scattered light or laser-induced fluorescence [61, 62, 64, 73]. Compact "lab-on-a-chip" devices employ integrated optical detection elements to monitor the characteristics of passing particles [74]. A recently developed microfluidic analysis system allows for the automated manipulation, phenotyping, and sorting of Caenorhabditis elegans specimens at rates of several hundred worms per hour [75].*

The schemes used to analyze the focused, particle-bearing stream are typically based on the detection of scattered light, fluorescence, or electrical signals. Most systems, such as the Luminex FlexMAP 3D instrument discussed earlier, employ optical detection. The simplest scheme analyzes the forward scattering, large angle scattering, and extinction of a laser beam focused on the particle-bearing stream [76]. Laser-induced fluorescence (LIF) offers a higher level of sensitivity, with the more complex approaches employing optical waveguides for both laser excitation and fluorescence detection [77]. A compact cytometer (50 cm × 30 cm × 15 cm) with a single photon counting avalanche diode (SPAD), diode laser, and digital data acquisition board was assembled by Niehren *et al.* [78]. In separate work, nanoparticles as small as 26 nm were detected using a relatively inexpensive Ar-laser/photomultiplier tube (PMT) optical setup [79]. Schemes that integrate detection elements into the microfluidic chip are far more costly and difficult to produce, but they eliminate the need to precisely align optical detectors like SPADs and PMTs. Impedometric detection also avoids this difficulty by using embedded electrodes that flank the focused stream to measure the spectral impedance of individual particles [80]. A recent advance in impedometric detection was made by Chun *et al.* with the introduction of embedded

polyelectrolytic salt bridge-based electrodes (PSBEs) [81, 82]. Photolithographic techniques were used to fabricate gel plugs that function like a salt bridge to size-selectively count passing particles as well as measure their velocities. Despite this recent advance, optical detection remains the most popular cytometry scheme because of its ability to extract more information on particle morphology and velocity. Currently, the vast majority of impedance-based systems can only serve as conventional counters.

1.1.3 Polymerase Chain Reaction Methods

The polymerase chain reaction (PCR) is perhaps the most powerful tool in molecular biology. First discovered in the early 1970s, the technique enables the creation of millions of copies of DNA from a single target sequence, a process with powerful implications for the detection of biomolecule species [83]. In its most conventional form, PCR utilizes a heat-stable DNA polymerase, deoxynucleoside triphosphates (dNTPs), and short complementary primer sequences to amplify the number of target sequences in solution. Thermal cycling allows for the repeated denaturation/melting of species, attachment of primers and polymerase to the target, and extension of the primers via incorporation of dNTPs. Most methods use between 20 and 40 cycles to generate a sufficient number of amplicons. Although primarily used for the amplification and detection of DNA targets, the process has been modified in a multitude of ways to enable the analysis of single-nucleotide polymorphisms (SNPs) [84], methylation points [85], RNA targets (reverse transcription PCR or RT-PCR) [86], and even protein species [87]. Quantitative PCR (qPCR) is a particularly powerful variant that offers the ability to measure the copy number of specific nucleic acids, often in real-time [88]. In this process the amount of amplified product is determined by quantifying a fluorescent signal that arises from the generation of amplicons. By monitoring the number of cycles required to bring the fluorescent signal above a predetermined threshold, it is possible to calculate how many target molecules were present in the starting mixture.

The ability of PCR to augment the number of target molecules in a sample leads to better sensitivity than that which can be achieved with standard planar and particle arrays. For example, for the detection of short RNA targets, the limit of detection of most PCR-based methods is 10^3-fold lower than conventional microarrays and 10^5-fold lower than solid-particle systems. While this enhanced sensitivity offers many advantages for the detection of rare targets in small, clinically-valuable samples, it should be noted that multiplexed sensing with PCR-based approaches generally requires more optimization and preparation steps than with multiplexing systems that do not amplify the number of target molecules. The amplification process almost always requires a purified input sample that is devoid of proteins and other factors that can interfere with the activity of the polymerase. For multiplexing approaches in which multiple primer sets are added into a single PCR mixture (typically contained within a snap-top tube), it is crucial to ensure that the annealing and melting temperatures of all involved complementary sequences are compatible with the cycling conditions and that the primer sets produce amplicons of distinct lengths that can

be distinguished from one another when run on an electrophoresis gel. Optimization of these parameters can become difficult for even modest levels of multiplexing, and as a result, optimized reagent mixes are often commercially-available for targets of significant clinical or research interest.

Applied Biosystems' TaqMan multiplexing technology consists of 96- and 384-well microfluidic cards, with each well containing a primer set for a specific target of interest [89]. While the spatial segregation of primer sets allows for easier readout of amplicon amount, this method typically requires larger input sample amounts and restricts the multiplexing flexibility by requiring the target to be covered by a commercial primer library. Furthermore, the cost of analyzing a single sample with the method is higher than for commercially available planar and particle arrays. The need to incubate the cards in an expensive temperature-cycling instrument also limits the processing throughput (number of samples per day) of the system, making this approach less than ideal for diagnostic and screening applications which require the analysis of hundreds of samples on a daily basis (Figure 1.5).

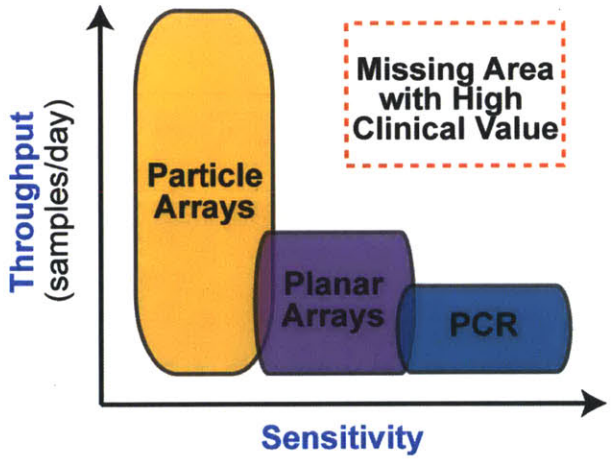

Figure 1.5: *Comparison of sample throughput and detection sensitivity for the three most common multiplexing platforms. The ideal system for clinical applications would enable high-volume processing while only requiring small amounts of easily accessible input sample.*

1.1.4 Single-cell Analysis

As the TaqMan card technology illustrates, the development of micro- and nanofluidic technologies has greatly expanded analysis capabilities, enabling the massively parallel interrogation of hundreds to thousands of tiny sample aliquots in a single trial on small, disposable chips. The ability to rapidly segment samples in nanoliter and picoliter volumes

with automated liquid handling and other injection techniques offers tremendous advantages in rapidly extracting information from precious samples. In addition to consuming less reagent and sample, smaller incubation chambers typically provide faster capture kinetics and localize/concentrate reporting signal for improved signal-to-noise ratio during post-assay analysis [90, 91]. One area of research that has greatly benefited from these features is single-cell analysis (SCA), which can broadly be defined as the interrogation of the genetic, proteomic, or metabolic profile of isolated cells to identify and characterize the heterogeneity of expression produced by stochastic cellular processes [92]. In the past a lack of suitable analysis technologies forced researchers to interrogate cell ensembles, a practice which cannot effectively identify "outlier" cells and which can often mask the true dynamics of the individual cells that make up the ensemble [93]. There are numerous examples of gene expression studies in which the ensemble average fails to accurately describe the expression levels of the individual cells, preventing the discovery of significant bifurcation behavior that can be indicative of disease development [92, 94]. In addition, the ability to measure molecular profiles with single cell resolution allows for the efficient analysis of rare or precious sample types such as embryonic cells and circulating tumor cells (CTCs) [95].

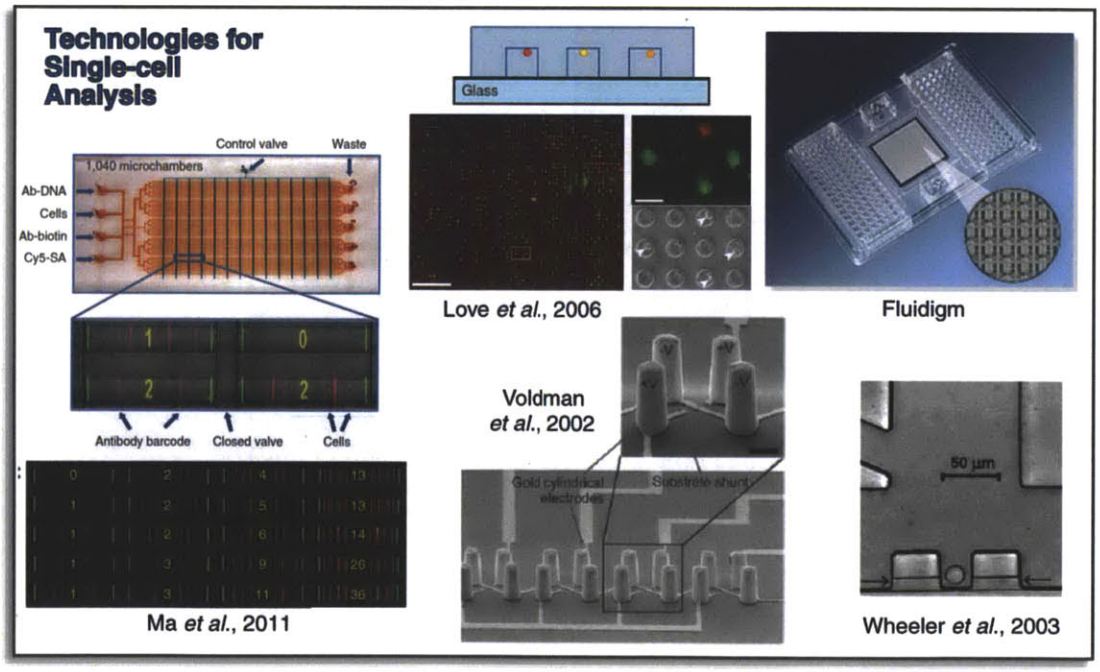

Figure 1.6: *Single-cell analysis techniques. Examples shown include the single-cell barcode chip (SCBC) [96], microengraving [97], dielectrophoretic cell trapping [98], Fluidigm's 96.96 Dynamic Array [99], and hydrodynamic cell trapping [91].*

The advent of technologies for SCA (Figure 1.6) has the potential to improve medical diagnostics and disease treatment by enabling the targeting of specific cell populations of interest in order to more clearly understand signaling pathways and the ways in which

those pathways influence the development of cells destined to effect disease. For example, by elucidating the characteristics of individual cells, it becomes easier to isolate the aberrations and heterogeneities within a network that give rise to tumor initiation, progression, and metastasis [92]. Furthermore, SCA can provide valuable insight into the susceptibilities of cancer stem cells, allowing for the rational design of therapeutic interventions [100]. The isolation and analysis of single cells from growing embryos also has powerful implications for the creation of diagnostic tests for genetic diseases and developmental abnormalities [101].

A significant amount of progress has been made in the design of systems for the manipulation and arrangement of single cells. To facilitate analysis, researchers have generated arrays of cells through the use of physical trapping structures [97, 102, 103], hydrodynamic traps [91, 104], holographic optical tweezers [105], dielectrophoretic traps [106], electroactive microwells [107], and emulsions [108]. The Quake lab's pioneering work with large-scale integration and on-chip PCR has enabled several high-throughput studies in which cells could be rapidly isolated and analyzed [109, 110]. A commercial venture (Fluidigm Corporation) spun out of these techniques now markets the Fluidigm Dynamic Array™, which is a microfluidic chip capable of measuring the expression level of 96 different mRNA transcripts in 96 individual cells [99]. Meanwhile, in "microengraving" approaches, cells are deposited in subnanoliter wells and their secreted products are captured on probes immobilized on a cover glass that is used to seal the wells for incubation [97]. In addition to providing high sensitivity in protein secretion assays (experimental limits of detection ranging from 0.5 to 4 molecules/s), this method allows for the 4-plex analysis of up to 10^5 cells/assay as well as the recovery of intact cells that exhibit interesting secretion profiles [111]. This ability to screen large populations and isolate atypical cells has led to applications in monoclonal antibody discovery [112]. The microengraving concept has also been extended to the massively parallel detection of gene expression in single cells [113].

The single-cell barcode chip (SCBC) is another microfluidic-based technology that enables the multiplexed measurement of secreted proteins. Originally designed for the multiplexed analysis of proteins in whole blood [114], the barcoded chip has recently been modified to facilitate the loading of thousands of cells per assay into 3-nL chambers [96]. The bottom surface of the chip consists of a polylysine-coated glass slide that has been microfluidically patterned with strips of spatially segregated capture probes. When the PDMS isolation chambers are properly registered with these strips, the chip enables 12-plex analysis of the secretions of the individual cells, with limits of detection as low as 100 molecules. The SCBC was recently utilized to measure functional heterogeneity in phenotypically similar T cells [96]. Ongoing modification of the chip and its loading valves should also enable the lysis of the entrapped cells, allowing for the analysis of various nucleic acid targets as well.

1.2 MicroRNA Profiling

A biomarker can generally be defined as a substance that indicates the biological condition of an organism and/or its susceptibility to therapeutic intervention. The degree to which molecular diagnostics is able to transform the medical landscape in future years depends as much on the identification of quality biomarkers with strong predictive power as it does on innovation in detection technology. The successful correlation of disease diagnosis, prognosis, and treatment efficacy to the expression patterns of a select set of molecular entities is crucial for the development of an era of predictive and personalized medicine. MicroRNAs (miRNAs) are short, non-protein-coding nucleic acids that have recently been shown to exert a significant amount of control over the translation of proteins from mRNA, and as a result, they have rapidly become a focal point in the search for effective biomarkers.

1.2.1 Biological Importance of MicroRNAs

Despite their abundance and their widespread influence over gene expression in both plants and animals, miRNAs were only recently discovered in 1993, during a study of the developmental timing of *Caenorhabditis elegans* larva by the Ambros lab [115]. Subsequent research uncovered that these non-protein-coding RNAs function as negative gene regulators either by directing the cleavage of mRNAs or by repressing mRNA translation through attachment to the 3' untranslated regions (UTRs) of their targets. The mechanism of posttranscriptional regulation depends on the degree of complementarity that exists between the miRNA and its target. The biogenesis of miRNAs begins in the nucleus of the cell, where pri-microRNA (pri-miRNA) transcripts produced by RNA polymerase II are separated into pre-microRNA (pre-miRNA) segments by the RNase III enzyme Drosha and the double-stranded-RNA-binding protein Pasha (Figure 1.7) [116-118]. These ~70 nucleotide precursors are then exported into the cytoplasm and processed further by the RNase III enzyme Dicer, producing a double-stranded RNA duplex typically between 21 and 25 nucleotides in length. Upon association with a ribonucleoprotein structure known as the RNA-induced silencing complex (RISC), one strand (termed the "mature" strand) is retained and used to target transcripts, while the other strand (termed the "passenger" strand) is degraded.

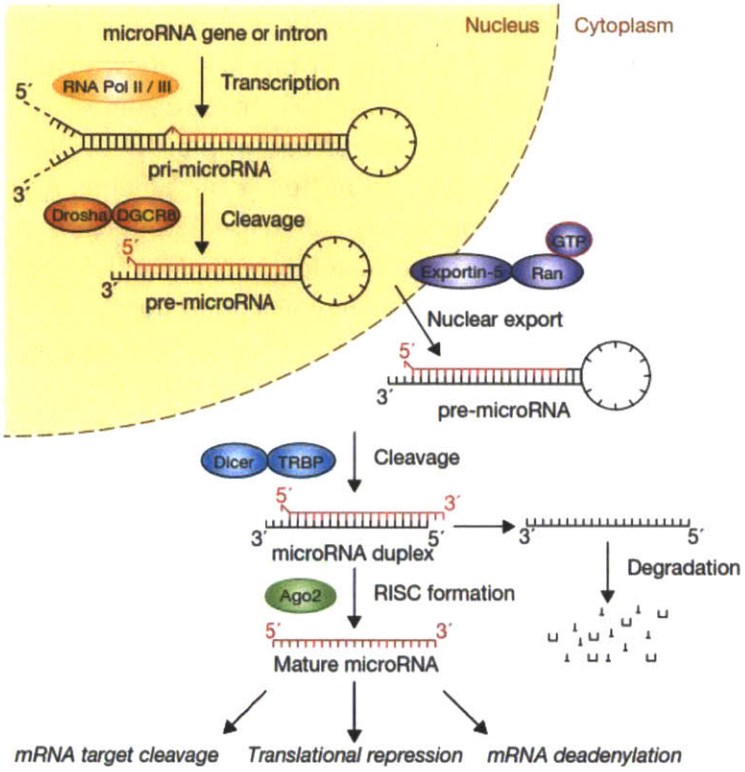

Figure 1.7: *Schematic description of the biogenesis and post-transcriptional regulatory function of microRNA. Adapted from [119].*

By regulating the expression of approximately half of all gene-encoding mRNAs, miRNAs play a crucial role in physiological as well as pathological processes. Most notably, this class of molecules has been implicated in the development and progression of various types of cancers including breast, lung, ovarian, cervical, prostate, colorectal, and liver cancers [117]. In addition to serving as oncogenes and tumor suppressor genes, miRNAs have also been identified as significant agents in the development of HIV/AIDS, cardiovascular diseases, neurodegenerative diseases, and herpesvirus infections [120-124]. This connection between aberrant expression of miRNAs and the emergence of disease states has led many researchers to look upon the ~1,000 known human miRNAs as a biomarker set that can be analyzed for diagnostic and prognostic purposes. Early efforts have demonstrated that profiling select sets of miRNAs offers a surprising wealth of information on the developmental lineage and differentiation state of tumors and provides more accurate diagnostic predictions than simply measuring transcript (mRNA) levels. For example, in one set of studies, the expression profiling of only 200 miRNA targets provided a better classification of cancer (12 of 17 correct) than a dramatically larger set of >16,000 mRNAs (1 of 17 correct) [125, 126].

The stability of miRNAs in a wide range of biological contexts is another significant factor in their emergence as a new class of biomarker. It has been shown that their small size and association with both ribonucleoprotein complexes and exosomes can protect them from degradation by RNases [127]. In recent years, circulating miRNAs have been discovered in several readily accessible biological fluids including serum, plasma, and urine. Correlations between disease state and expression levels of these circulating species suggest that miRNAs could be strong candidates for the development of noninvasive biomarker screens for the early, asymptomatic detection of tumorigenesis and for the monitoring of treatment response [128-131]. Further studies of the exosome-mediated transfer of miRNAs between cells indicate that the measurement of circulating miRNAs could have important implications for understanding cancer metastasis as well as intercellular communication between cells of the immune system [132, 133].

1.2.2 Current MicroRNA Detection Technologies

Despite tremendous advances in technologies for the multiplexed assay of nucleic acids, it has proven challenging to accurately and efficiently profile miRNAs [134, 135]. Their small size, wide range of abundance, secondary structure, and high degree of sequence homology have made it difficult to adapt existing quantification strategies originally developed for the detection of long DNA and mRNA sequences. MicroRNA profiling applications in the discovery and clinical fields require a detection platform that offers high-throughput processing, large coding libraries for multiplexed analysis, and the flexibility to develop custom assays.

Microarray systems provide high sensitivity and sufficient multiplexing capacity to probe the full set of human miRNAs in a single assay. During an initial preparation step, the total RNA in a sample is isolated and then the purified small RNA fraction is either enzymatically labeled with fluorophore in an overnight step ("direct labeling") or it is reverse transcribed and the resulting cDNA is labeled with a dye ("indirect labeling") [136]. As described in Section 1.1.1, the labeled entities are then hybridized to the array in a 12–24 h incubation step, and the fluorescence pattern of the array is interrogated with a scanning instrument and software, enabling quantification. Due to the short size of the miRNA targets, there is significant variability in the melting temperatures (T_m's) of the hundreds of different target-probe complexes formed on the surface of the microarray, which can lead to challenges in accurately determining the amount of target initially present in the starting sample [137]. This problem can be alleviated through the optimization of probe design (*i.e.*, subtracting bases or varying attachment spacer) or by the use of specialized capture probes such as LNAs. From a workflow perspective, microarray strategies for miRNA detection are relatively low-throughput and inflexible due to the fixed design of the probe-set, cumbersome preparation steps, and the long incubation times required for sensitive analysis. Furthermore, the mass-labeling of all species prior to hybridization introduces the possibility of labeling biases and can be prohibitively expensive for the high-volume sample analysis involved in clinical applications [137, 138].

Current particle-based platforms for miRNA profiling offer more versatility, greater reproducibility, and higher processing speeds than microarrays, although they are not nearly as sensitive (Table 1.1) [137]. The encoded polystyrene and glass particles produced by Luminex (50-plex) and Illumina (735-plex), respectively, are selectively added to samples (usually isolated total RNA) to create a custom multiplexing panel for each experiment performed. This modular design to multiplexing enables more efficient consumption of reagents. In general, miRNA assays with particle platforms are faster than those with microarrays due to the enhanced mass transfer provided by particle mixing during incubation and the high-throughput particle scanning systems capable of analyzing hundreds of samples per day. The Illumina BeadArray system boasts the best performance characteristics, with a dynamic range of four logs, an enzyme-assisted labeling scheme that improves detection specificity, and the ability to profile almost the entire set of human miRNAs in 100–200 ng of total RNA [35, 59]. In contrast to microarray protocols which often take two full days, the Illumina technology can process over 100 samples per day from start to finish. The Luminex system offers a similar throughput but requires larger total RNA inputs and provides a smaller coding library [41].

	Microarray [134, 138]	**qRT-PCR [134, 139]**	**Luminex Beads [41, 59]**	**Illumina BeadArray [35, 59]**
Limit of Detection	0.2 amol	10s–100s of copies	200 amol	1 amol
Recommended Total RNA Input (ng)	100–1000 for 950-plex	500 for 754-plex	500–2000 for 50-plex	10–200 for 735-plex
Throughput (samples per 8-h day per machine)	1	2	150	500
Total Assay Time (h)	24–48	6	5	6
Multiplexing Capacity	10^6	754	50	735
Dynamic Range	4 logs	7 logs	3 logs	4 logs
Target Amplification Step?	No	Yes	No	Yes

Table 1.1: *Comparison of platforms for multiplexed miRNA detection.*

Quantitative real-time PCR (qRT-PCR) currently provides the highest degree of sensitivity for miRNA profiling, with as little as 25 pg of total RNA required for multiplexed assay. Initial efforts to adapt PCR to the detection of clinically-relevant mature miRNAs were hampered by the small size of the targets and by the presence of pre-miRNAs. An innovative stem-loop primer design was introduced in 2005 to markedly improve discrimination between mature and precursor sequences and to augment amplification efficiency of the short miRNA targets [136, 139]. Further proof-of-concept work has combined the stem-loop primer strategy with additional stages of target/cDNA amplification to boost sensitivity to a level that allows for the 220-plex and 384-plex expression profiling of single cells [140-142]. Although these single-cell protocols can take up to seven days and require extensive reagent optimization to prevent amplification biases, they are powerful methods that underscore the analytical advantages of target-

based amplification. Commercial vendors have sought to balance the need for exquisite sensitivity with the end-user desire for an efficient, semi-automated workflow that delivers reliable quantification. Microfluidic cards that employ carefully optimized stem-loop primers and the TaqMan fluorescent labeling scheme are now commercially available for the simultaneous assay of fixed panels of 384 human miRNAs. While this TaqMan miRNA platform offers tremendous sensitivity (limits of detection between 10 and 100 copies), dynamic range (7 logs), and specificity (high discrimination efficiency for single-base mismatches), it requires dedicated, expensive instruments for assay and analysis, which can limit sample processing throughputs. A single PCR machine, for example, can process only two samples in an eight-hour workday. The high cost of the qRT-PCR reagents also makes it less than ideal for high-volume sample analysis in clinical and research settings [136].

In addition to microarrays, particle systems, and qRT-PCR, a range of other specialized methods have been employed for the multiplexed detection of miRNA, including Northern blotting [143], isotachophoresis [144], nanomechanical arrays [12], nanopore sensors [145], electrochemical genosensors [146], silver nanocluster probes [147], and cation exchange-based fluorescence amplification (CXFluoAmp) [148]. Deep sequencing efforts have also expanded considerably within the miRNA community in the past few years, with new technologies increasing the throughput and decreasing the cost of such analysis [149]. Although current approaches require large amounts (1–10 μg) of highly purified input RNA and time-consuming preparation steps, sequencing does not require knowledge of target identity and can thus be utilized for the discovery of unknown small RNAs, a powerful feature that distinguishes it from other techniques [149]. As technological advances further improve the efficiency and lower the cost of this method, it is expected that sequencing will become an increasingly common method for miRNA analysis in biological samples.

1.3 Flow Lithography

Over the last 20 years, microfluidic technologies have transformed how researchers approach challenges in clinical diagnostics and disease treatment. Although the greatest amount of attention has been reserved for integrated "lab-on-a-chip" technology and other complex devices that promise "sample in, answer out", there have been equally impressive advances in the use of microfluidics for the production of high-value biomedical products and tools [150-152]. A prime example of this innovation is the flow lithography (FL) procedure, a high-throughput microfluidic process capable of generating chemically and geometrically complex microparticles with physical properties that can be tuned for a range of applications.

1.3.1 Operational Principles

The FL procedure combines the advantages of microfluidics (low reagent consumption, laminar co-flow properties, continuous processing capability) with the flexibility and

precision of lithographic patterning to create polymeric microparticles and colloids. The first version of the process (continuous flow lithography, CFL) involved the injection of a polymeric precursor liquid into a simple PDMS microfluidic channel that had been bonded to a glass slide coated with a thin layer of PDMS [153, 154]. The precursors typically contained a monomer species as well as an appropriate photoinitiator, and upon irradiating the precursor flow with a shutter-controlled burst of UV light, gelation would occur within the stream and produce a free-floating polymeric particulate that was advected along with the flow towards an outlet port for harvesting. The use of a PDMS device and a PDMS-coated substrate allowed for the penetration of oxygen into the synthesis chamber; this thin oxygen inhibition zone served to terminate the polymerization at the liquid-PDMS interfaces and facilitated the creation of flowing particles rather than structures affixed to the surfaces of the synthesis chamber [155].

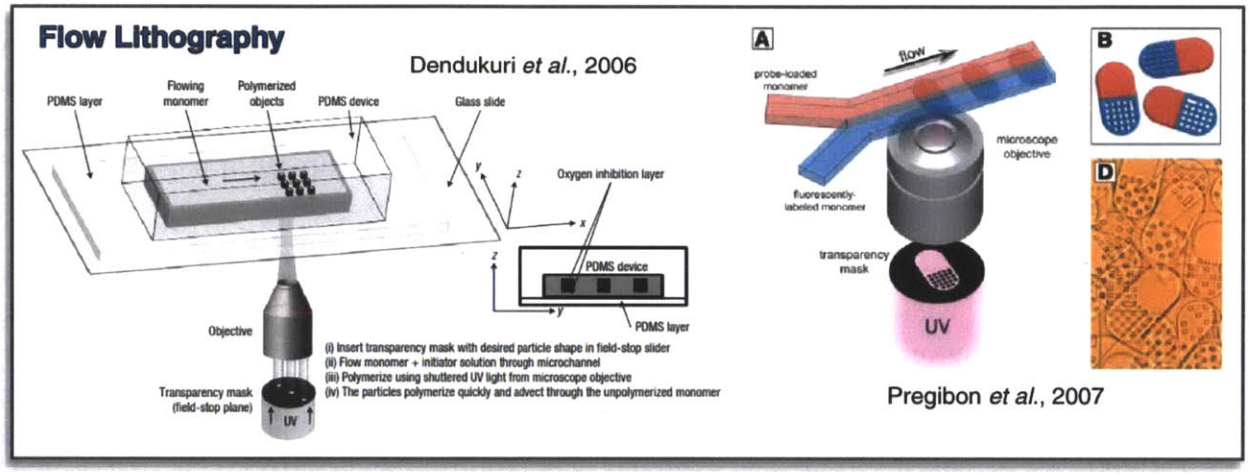

Figure 1.8: *Flow lithography for the synthesis of chemically and geometrically complex gel microparticles. Laminar co-flowing streams of photoreactive monomers are periodically exposed to bursts of UV light through a transparency mask to create free floating particulates of arbitrary two-dimensional shape that can then be advected out of the synthesis zone for collection and use [52, 153].*

When the synthesis device was mounted on a standard inverted microscope with a UV illumination source, a transparency mask with a desired set of features could be inserted into the field stop of the microscope to physically limit the passage of the UV light, thereby selectively gelling only certain portions of the stream and allowing for the creation of polymeric particles with arbitrary two-dimensional designs (Figure 1.8) [156]. This photolithographic printing of particles represented a new paradigm in continuous microparticle synthesis in microchannels because it afforded unprecedented control over particle size, morphology, and chemistry [157, 158]. Previous flow-synthesis methods relied on the dispersion of a precursor fluid in an inert continuous phase, a strategy which limited the microparticle geometry to a sphere or a deformation of a sphere and which significantly

complicated efforts to impart chemical anisotropy [157]. The microfluidic nature of the CFL process also enabled the laminar co-flow of several precursor streams so that anisotropic particles could be created with multiple distinct chemistries adjacent to one another. This aversion to stream mixing was the result of the small length scales of the synthesis devices (typical cross-sections of 200 μm × 30 μm) and the low injection velocities of the precursors, which together produced low-Reynolds number (low-Re) flows dominated by viscous rather than inertial forces [153, 159].

Although the continuous process of CFL afforded many advantages, it was necessary to limit flow velocity to ensure that particle interfaces would not be smeared during the UV exposure step. To address this resolution issue and to augment the production rate of particles by allowing for higher flow velocity, the semi-continuous stop-flow lithography (SFL) procedure was developed [160]. Leveraging the rapid response time of a pressure-driven flow control system, the precursor flow in SFL was quickly pulsed and synchronized to a computer-controlled shutter for precise UV dosage [161]. In the cyclical procedure, flow was automatically initiated, stopped, subjected to a UV burst, and then re-initiated to remove particles from the synthesis zone. Depending on particle complexity, SFL synthesis throughputs as high as 10^5 particles/h could be achieved, with a minimum feature size of 6 μm when using a 20× objective for the photolithographic exposure [160].

Since its introduction, SFL and technical variants of SFL have been employed extensively for the creation of a wide range of chemically complex polymeric particles, including some with anisotropy along multiple dimensions [40, 49, 162-171]. Perhaps the most active area of SFL research has been the synthesis of hydrogel microparticles, which are composed of hydrophilic polymer chains that characteristically retain water. Although many materials are available for the synthesis of such particles, poly(ethylene glycol) (PEG) precursors have proven especially useful due to their compatibility in biological applications. PEG-based hydrogels are both bioinert and non-fouling and thus can be inserted into biological contexts without significantly perturbing the environment and without non-specifically adsorbing biological molecules. These features make them ideal for biosensing applications in which probes need to be immobilized on passive substrates that will selectively capture only those targets they are designed against. Furthermore, PEG oligomers can be obtained in a variety of molecular weights and with a range of functionalities, making it straightforward to tailor the chemical, physical, and material properties of the gels produced [172]. For example, PEG-diacrylate (PEG-DA) oligomers can be polymerized with nucleic acids functionalized with an acrylate group to produce a gel network with covalently bound DNA or RNA. The porosity and cross-link density of the resulting gel can also be controlled by adjusting the relative amounts of PEG-DA, photoinitiator, and an inert species such as aqueous buffer or PEG [173].

1.3.2 Hydrogel Microparticles for Biomolecule Analysis

Despite the dramatic advances in multiplexing technology over the last 30 years, it has become clear that the current paradigm of surface immobilization of probe species in both microarrays and particle systems is suboptimal [4, 23]. The attachment of probes to the surfaces of slides and beads inevitably leads to steric hindrance of probe-analyte interactions, nonideal kinetics, and slow approaches to equilibrium. As described earlier in Section 1.1.1, microchips featuring oligonucleotides immobilized throughout a porous, three-dimensional hydrogel were developed by Mirzabekov *et al.* in the early 1990s for SBH and later extended to the detection of DNA polymorphism, proteins and even whole cells [10, 21-23]. In addition to boasting high probe incorporation efficiencies and short hybridization times, the novel three-dimensional platform reduced molecular crowding, thereby providing a thermodynamically more favorable environment for biomolecule capture.

Nearly two decades after the initial work of Mirzabekov, the SFL process was used to combine the advantages of gel-based immobilization with suspension array technology to create multifunctional, graphically-encoded hydrogel microparticles for biomolecule analysis [52]. Using precursor mixtures containing PEG-DA, PEG, Darocur 1173 photoinitiator, and Tris-EDTA buffer, tablet-shaped microgel particles were simultaneously synthesized, encoded, and functionalized with DNA capture probes in a single step at rates up to 10^4 particles/h (Figure 1.8). Utilizing SFL's ability to polymerize across laminar co-flowing streams, each particle consisted of multiple chemical sections, with one "code" region and one or more "probe" regions. In the code region, a fluorescently-labeled acrylate molecule was added to the precursor, and unpolymerized holes in the wafer structure of the particle (created with an appropriate transparency mask) were used to construct a 20-bit graphical code. This code was then used to identify the acrylate-modified DNA probe(s) added to and covalently incorporated within the other region(s) of the particle. The physical separation of code and probe regions on each particle enabled the use of a common wavelength for all optical signaling purposes, thus avoiding the spectral issues and cumbersome equipment requirements of other particle systems. In addition, although the tablet-shaped microparticles were larger (200 μm long × 60 μm wide × 30 μm thick) than the more commonly used latex microspheres, they exhibited higher sensitivity, superior specificity, and shorter hybridization times than the solid spheres in initial assays of model DNA sequences [174].

1.4 Outline of Thesis

The purpose of this work is to enhance the utility of graphically-encoded hydrogel microparticles so that they may be employed for the sensitive, specific, and high-throughput detection of microRNAs and potentially other medically-relevant biomolecules. The organization of this work is as follows:

Chapter 2 describes the materials and methods employed in the synthesis, use, and analysis of the gel particles.

Chapter 3 details a parametric study of the factors that govern the flow alignment of soft gel microparticles in microfluidic devices.

Chapter 4 describes the construction of a microfluidic particle scanner, as well as the development of a 12-plex assay for a panel of clinically significant miRNAs.

Chapter 5 details the creation of a signal-amplification scheme that enables the visualization of single-molecule binding events on the surface of the gel particles. The development of a serum-based miRNA assay is also described.

Chapter 6 describes the development of lysate-based miRNA assays and a microwell approach to analyze the miRNA profiles of single cells and small groups of cells.

Chapter 7 summarizes the findings of this thesis and discusses future work.

Chapter 2

General Materials and Experimental Methods

This portion of the thesis provides a consolidated overview of the various chemicals, buffers, and methods frequently used in experiments. The materials and general techniques described here are referenced throughout the thesis, and in the event that alterations were made to these protocols during the course of research, those changes are explicitly detailed in the appropriate chapter.

2.1 Materials

2.1.1 Chemicals and Buffers

For the sake of brevity, acronyms and chemical trade names will be used throughout the thesis instead of full chemical names. The abbreviations are given in Table 2.1 below.

Oligomers and Elastomers	
PDMS	Polydimethylsiloxane (Sylgard 184, Dow Corning)
PEG_{200}	Poly(ethylene glycol), n = 200 g/mol (Sigma)
PEG_{400}	Poly(ethylene glycol), n = 400 g/mol (Sigma)
$PEG\text{-}DA_{700}$	Poly(ethylene glycol) diacrylate, n = 700 g/mol (Sigma)

Fluorescent Molecules	
Rhodamine-acrylate	Methacryloxyethyl thiocarbonyl rhodamine B (Polysciences)
SA-PE	Streptavidin-R-phycoerythrin (Invitrogen)

Miscellaneous Chemicals	
Darocur 1173	2-hydroxy-2-methylpropiophenone (Sigma)
SDS	Sodium dodecyl sulfate (Invitrogen)
Tween-20	Polyoxyethylenesorbitan monolaurate (Sigma)
PK	Proteinase K (New England Biolabs)

Buffers	
TE (1×)	10mM Tris pH 8.0 (USB) and 1mM EDTA (USB) in nuclease-free water
TET	1× TE buffer with 0.05% Tween-20
PTET	5× TET buffer with 25% PEG_{400}
PBST	Phosphate buffered saline (PBS, Cellgro) with 0.05% Tween-20 (pH 7.4)
NEB2	New England Buffer #2 (New England Biolabs)
R50	TET with 50mM NaCl

Prepolymer Mixtures	
DA20	20% PEG-DA_{700}, 40% PEG_{200}, 35% 3× TE, 5% Darocur 1173
DA30	30% PEG-DA_{700}, 30% PEG_{200}, 35% 3× TE, 5% Darocur 1173
Code Monomer	35% PEG-DA_{700}, 20% PEG_{200}, 40% 3× TE, 5% Darocur 1173
Inert Monomer	35% PEG-DA_{700}, 20% PEG_{200}, 40% 3× TE, 5% Darocur 1173

Table 2.1: *List of frequently used acronyms and chemical trade names. All percentages represent v/v concentrations.*

2.1.2 Oligonucleotides

All oligonucleotides used in this work were purchased form Integrated DNA Technologies (IDT) and stored in buffers prepared from nuclease-free water. There are two main classifications for the oligonucleotides used: (1) "probes" are DNA oligonucleotides that are covalently incorporated within particles for the capture of specific biomolecules and (2) "targets" are the DNA or RNA oligonucleotides that are to be detected by the particles in solution. DNA probes were purchased as lyophilized films in 250 nmol quantities with HPLC purification. They were ordered with an Acrydite™ modification on the 5' end to facilitate incorporation into the hydrogel network and with an inverted dT modification on the 3' end to prevent incidental ligation of labeling sequences to the untethered end. After suspending and appropriately diluting the DNA in 1× TE, the oligonucleotide probes were stored at -20°C in snap-top 0.65-mL tubes in aliquots of 5 μL at either 500 μM or 1 mM in labeled cardboard sample boxes. Meanwhile, targets were purchased as lyophilized films in 250 nmol quantities with RNase-free HPLC purification. Targets were suspended in the stock tube in 1× TE at a concentration of 100 μM, and then at least four 100-μL "mini-stocks" were created at a concentration of 10 μM in separate 0.65-mL snap-top tubes. One of these mini-stocks was then used to create aliquots of 5 μL at 10 μM. All targets were stored at -20°C in labeled cardboard sample boxes. To maintain integrity, all aliquoted targets and probes remained frozen at -20°C until 10–20 min prior to use in experiment.

2.2 Equipment Setup

2.2.1 Configuration of Microscope for Polymerization

PDMS synthesis devices were mounted on a Zeiss Axio Observer microscope equipped with a Zeiss Plan Neofluar 20× objective (NA 0.50) and a Chroma 11000v3 UV filter. A UV source (Lumen 200 at 100% setting, Prior) was connected to a VS25 Uniblitz shutter system, which in turn was attached to the rear port of the microscope either directly or via a switching mirror box. Two neutral density filters (OD 0.05 and OD 0.4) were inserted in series into a slider bar and placed in the aperture slot of the microscope to reduce UV intensity to a level that enabled high-resolution polymerization with exposure times between 50 and 100 ms. A power meter (Newport, Model 1815-C) and appropriate adjustment of exposure time were used to ensure a consistent UV intensity. Transparency masks with a diameter of 2.5 cm were ordered from Fineline Imaging and placed into a second slider bar, which was inserted into the field stop slot of the microscope. To ensure the transparency was flush with the back of the slider bar, the mask was sandwiched between a circular cover glass (25 mm, VWR) and a blue spacer ring. A rubber o-ring was then inserted to hold the spacer ring down. The automated flow/stop/expose cycles required for SFL were controlled by a custom-written Python script. A compressed-air flow control system provided rapid dynamic response and precise control of multiple inlet streams; the construction and operation of this system has been described extensively elsewhere [161].

2.2.2 Acquisition of High-speed Flow-focusing Movies

Flow devices with two inlets and one outlet were mounted on an inverted microscope (TE2000U, Nikon) for visualization with 10× and 4× objectives. Prior to being loaded into the flow device, particles were removed from the refrigerator, rinsed 4 times in PTET, and allowed to sit at room temperature for 90 min. PTET was used to obtain better density-matching between the particles and the liquid medium in order to minimize the effects of sedimentation in the loading process. The PTET was sonicated for 1 min before use to eliminate polymer agglomerations that could disrupt particle flow. Once the particles were diluted to the appropriate concentration (10–20 particles/μL) with PTET, 20–30 μL of the mixture was loaded into a pipette-capped length of Tygon tubing, and the pipette was inserted into the central port of the device. Particle types were never mixed together; each flow trial consisted of particles of identical shape and composition. A modified Eppendorf tube containing a 2% (v/v) solution of food coloring in PTET was connected to the outer inlet port via metal tubing. Tygon tubing was inserted through a hole in the Eppendorf cap to provide driving pressure. The tubing from the inlets was then attached to two separate pressure regulators (Omega) to provide independent control over the two streams. Flow devices were able to be reused up to 25 times without any decrease in performance. The compressed air source used to drive the flows was a plastic canister with a hand pump. Upon sufficient pumping, a two-way valve connecting the canister with the regulators was opened, thereby inducing flow. Pressures of 9 psi were able to be maintained for more than

a minute using this simple setup. A high-speed Phantom camera (Vision Research) captured images at rates ranging from 4,000 to 15,000 frames/s. Still images from the movies were analyzed using the Phantom Cine Viewer software (2.24 μm/pixel for 10× and 12.44 μm/pixel for 4×). Detection zone measurements of velocity, position, and alignment were made 750 μm from the outlet to ensure consistency.

2.2.3 Configuration of Microscope for High-throughput Scanning

PDMS focusing devices were mounted on a Zeiss Axio Observer microscope equipped with a Zeiss Plan Neofluar 20× objective (NA 0.50) and an Omega XF101-2 filter (Figure 2.1). A chrome-coated soda-lime glass mask (Advance Reproductions) was fitted into an iris slider bar and inserted into the field stop of the microscope to limit the beam spot of a 100-mW, 532-nm laser (Dragon Lasers) to a thin excitation window of 4 × 90 μm in the scanning plane. Prior to each scanning session, laser alignment was calibrated with a power meter (Newport, Model 1815-C). Using images captured from a Clara Interline CCD camera (Andor Technology), the excitation window was oriented such that its long dimension was aligned perpendicular to the flow direction approximately 750 μm from the exit port of the device. A switching box on the side port of the microscope was used to alternate between the CCD and a photomultiplier tube (PMT, Hamamatsu H7422-40) used to record fluorescence signatures of passing particles. The output current of the PMT was conditioned using a homemade amplifier with a low-pass filter, and the resulting voltage signal was captured at a rate of 600 kHz by a digital acquisition (DAQ) board (USB-6251, National Instruments). A Python script was written to convert each scan to a binary text file for off-line analysis. Single-chemistry particles with fluorescent rhodamine incorporated throughout were scanned to optimize the performance of the scanning system, leading to a combination of amplifier gain (22), cutoff frequency (100 kHz), slit width (4 μm), and PMT control voltage (0.300 V) that produced the highest signal-to-noise ratio (SNR) and frequency response possible.

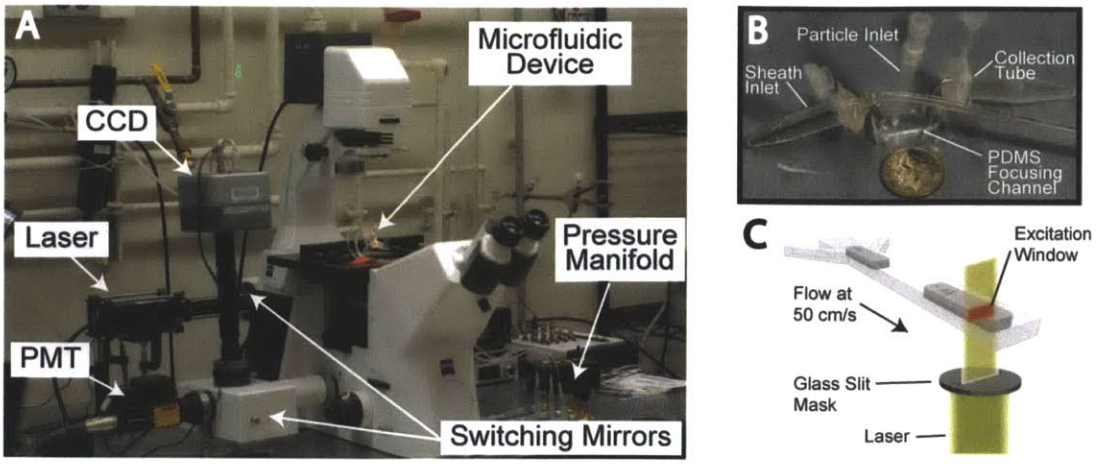

Figure 2.1: *Equipment setup for particle scanning. (A) Image of the inverted fluorescence microscope configured for scanning. The switching mirrors are used to toggle between the different excitation (Lumen UV and laser) and detection (CCD and PMT) instruments. (B) Image of the PDMS flow-focusing device, with fluid inlets and outlet attached. (C) Schematic of the slit-scan process.*

2.3 General Experimental Protocols

2.3.1 Soft Lithography and Assembly of Microfluidic Channels

Master molds for the production of PDMS devices were either created at the BioMEMS Resource Center (BMRC) in Charlestown, MA or purchased from the Stanford Microfluidic Foundry. For those molds fabricated at the BMRC, a clean silicon wafer was first spin-coated at an appropriate speed with negative photoresist (SU-8 25, MicroChem). High-resolution photomasks (10,000 dpi, CAD Art Services or Fineline Imaging) were then used to selectively expose the coated wafers to UV light, thus creating the desired channel patterns. Following treatment with SU-8 developer (MicroChem), the wafers were flood exposed to UV light and baked. A profilometer (Dektak) was used to determine the heights of features located on the left, right, and central portions of the wafer. The wafers were then treated with a fluorosilane ((tridecafluoro-1,1,2,2-tetrahydrooctyl)1-trichlorosilane, United Chemical Technologies, Inc.) by placing five drops of the silane in a vial next to the wafer under vacuum for 60 min in a chemical fume hood. PDMS prepolymers (10 parts base, 1 part curing agent) were poured over the molds to a depth of 5 mm, degassed in a vacuum chamber for 60 min, and allowed to cure in an oven at 65°C for 12 h. Individual channel designs were cut from the mold with a scalpel, and inlet and outlet holes were punched with blunt 15-gauge luer stub adapters (Clay Adams). The devices were then rinsed with water and ethanol, dried with argon gas, placed channel-side down on slides coated with partially-cured PDMS (20–25 min at 65°C), and baked in an oven at 65°C for 12 h. Microchannels used for particle synthesis had heights between 37 and 40 μm, while those used for flow-through particle analysis were between 38 and 40 μm in height.

2.3.2 *Preparation of Prepolymers*

The porosity and detection properties of hydrogel particles depend on the composition of the prepolymers from which they are synthesized. As a result, it was critical to ensure that the prepolymer preparation steps were precise and reproducible. The necessary reagents (PEG-DA_{700}, PEG_{200}, Darocur 1173, 3× TE, 1× TE, food coloring) were first aliquoted in separate glass vials. In the prepolymer preparation, after the addition of each reagent to a 1.7-mL snap-top tube, the solution was vigorously agitated on a vortex at the highest setting to ensure complete mixing. In the initial step, PEG-DA_{700} was carefully added, followed by PEG_{200} and then Darocur 1173. For the pipetting of these three viscous reagents, it was critical to draw up and dispense the liquid at a slow rate such that the main liquid front and the secondary residue front traveled at the same velocity within the pipette. Failure to do so resulted in residual liquid remaining trapped in the pipette and thus inaccurate dispensing of reagent. 3× TE was added after the PEG-DA_{700}, PEG_{200}, and photoinitiator were thoroughly mixed. Depending on prepolymer type, the monomer solutions were then either added to a previously prepared aliquot of DNA probe ("probe" monomer) or supplemented with additional reagents ("DA20", "DA30", "code" monomer, and "inert" monomer) (Table 2.1).

For flow focusing experiments, DA20 and DA30 were mixed 9:1 with 1× TE to mimic the prepolymer formulation used in previous nucleic acid detection experiments. For detection experiments, code prepolymer was formed by combining code monomer with 1× TE and rhodamine-acrylate (Rh-Ac, 1 mg/mL) to give final concentrations of 9.4% and 0.6%, respectively. Inert prepolymer was formed by combining inert monomer with 1× TE and blue food coloring to give final concentrations of 8.0% and 2.0%, respectively. Food coloring was used to introduce contrast between neighboring streams for easier adjustment of stream width during SFL. Probe regions on single-probe particles were polymerized from a monomer that was added to acrydite-modified DNA probe sequences suspended in 1× TE to give the desired concentration of probe in 18% PEG-DA_{700}, 36% PEG_{200}, and 4.5% Darocur 1173; the remaining balance consisted of 3× TE. For multi-probe particles, certain probe prepolymers were modified to allow for stream visualization during synthesis by replacing a portion of the 3× TE with food coloring (final concentration of 2%). Once all reagents had been added and thoroughly mixed, each prepolymer was centrifuged (VWR Galaxy Mini-Star, 2,000 *g*) for 14 min prior to injection into the synthesis device to sediment any debris or agglomerations that could clog the microchannels. Code and inert prepolymers could be used for up to three weeks after preparation; probe prepolymer was prepared fresh on the same day as the synthesis.

2.3.3 *Particle Synthesis*

Hydrogel microparticles with up to six different chemical regions were simultaneously synthesized, functionalized, and encoded at rates up to 18,000 per h with 50–100 ms UV exposures using the SFL method (Figure 2.2) [52, 160]. Exposure time was periodically

adjusted to compensate for the aging of the UV bulbs used [175]. Code, inert, and probe prepolymer solutions were loaded into microfluidic synthesis channels with 1–6 inlets using modified pipette tips as delivery chambers. These tips were rinsed with water and ethanol and then dried with argon gas prior to use; this practice was seen to dramatically reduce the frequency of clogs in the synthesis channels. The modified tips were connected to an adjustable pressure manifold with Tygon tubing, and forcing pressures of 3–4.5 psi were used to drive flow [161]. As discussed earlier, when synthesizing particles with multiple chemistries, food coloring was added to certain prepolymers to create a contrast difference that could be exploited for stream visualization in the synthesis process using a CCD camera (Hitachi KP-M1A or Andor Clara).

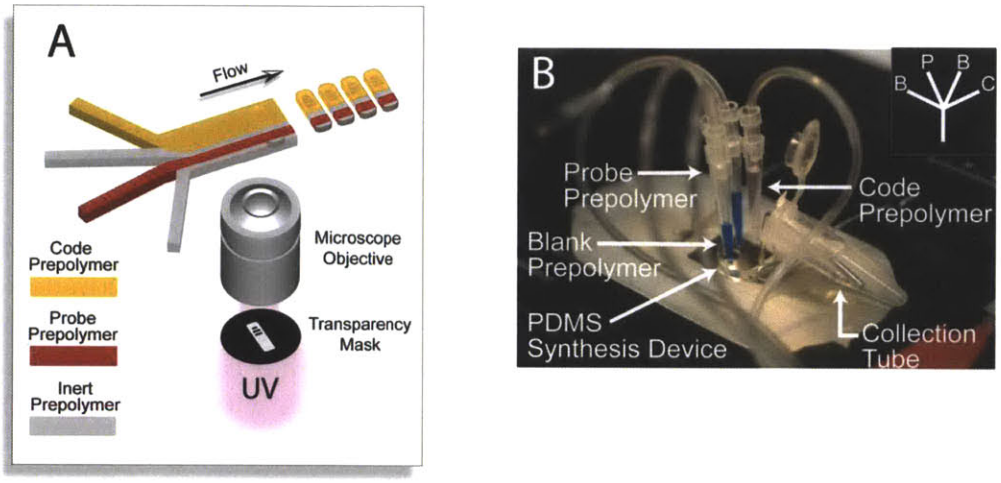

Figure 2.2: *Microparticle synthesis using SFL. (A) Schematic of the creation of a single-probe particle in a four-inlet channel. (B) Image of a four-inlet device mounted on an inverted fluorescence microscope for synthesis. C = Code, B = Blank (Inert), P = Probe.*

Following polymerization, particles were flushed down the synthesis channel and collected in a 1.7-mL Eppendorf tube containing 950 µL of TET. Tween was used in the collection buffer to prevent particle aggregation. Particles were next suspended in 200 µL of PEG_{200} for 5 min and then rinsed with 700 µL of TET. This washing sequence was used to rinse the particles of unreacted PEG-DA_{700}, probe, and rhodamine-acrylate. The wash sequence was then repeated two more times and required manual aspiration of supernatant facilitated by centrifugal separation of the dense particles. After two further washes with 500 µL TET, particles were stored in TET at a final concentration of ~12.5 particles/µL in a refrigerator at 4°C. Unless otherwise noted, particle dimensions cited in this work refer to the size expected from the transparency mask used. Depending on buffer conditions, the size of the particle could be greater or smaller than the original synthesis dimensions due to swelling.

2.3.4 MicroRNA Assay with Ligation Labeling

For trials involving non-amplified ligation labeling of captured miRNA targets, particles were brought to room temperature prior to use, and each target incubation was typically carried out in a total volume of 50 μL in a 0.65-mL snap-top tube with a final salt concentration of 350 mM NaCl and at least 30 replicates of each particle type (up to 500 particles/incubation tube). For calibration and specificity studies, a hybridization buffer (TET with assay-specific NaCl molarity) was first added to the Eppendorf tube, followed by all relevant target sequences appropriately diluted in 1× TE. Tween was excluded from the dilution buffer to prevent inaccuracies in pipetting steps that can arise from surfactant-induced changes in wettability. Depending on the assay type, either 1 μL of TET or 1 μL of *E. coli* total RNA (200 ng/μL, Ambion) was introduced to simulate sample complexity.

For human tissue profiling studies, hybridization buffer was added directly to a tube containing either 2.5 or 1.0 μL of previously frozen extracted total RNA (one individual per tissue type; stored at 100 ng/μL). Primary pair samples consisted of total RNA isolated from primary tumor and its adjacent normal tissue. Total RNA for all tissues was isolated by TRIzol purification; integrity of isolation was confirmed by checking for intact 18S and 28S ribosomal RNA. Lung sample (BioChain) was obtained from 50-year-old male with poorly differentiated squamous cell carcinoma. Breast sample (BioChain) was obtained from 53-year-old female with moderately differentiated invasive lobular carcinoma. Stomach sample (BioChain) was obtained from 70-year-old female with poorly differentiated adenocarcinoma. Pancreas sample (BioServe) was obtained from 65-year-old female with well-differentiated acina cell carcinoma. For all assays, 1 μL of miSpike target appropriately diluted in 1× TE was also introduced to give a total amount of 100 amol of the synthetic sequence to measure consistency of scanning/labeling and for quantification purposes. Prior to the addition of particles, incubation mixtures were heated to 95°C for 5 min in a thermoshaker (Biomega, 1500 rpm) and then brought back to room temperature over a 7-min period. A previously prepared master mix of particles (18 per μL) was thoroughly vortexed for 1 min, and 20 μL (~30 particles of each probe type) was introduced to each incubation tube. Incubation with target was carried out at 55°C for 90 min in a thermoshaker (1500 rpm).

Following hybridization with target, samples were rinsed three times with R50 solution. Supernatant was manually aspirated from the tube following centrifugal separation of the particles. All but 50 μL of solution was aspirated after the third rinse. Next, 245 μL of a previously prepared ligation master mix (100 μL 10× NEBuffer #2, 900 μL TET, 250 nM ATP, 40 nM universal adapter, and 800 U/mL T4 DNA ligase) was added to the tube. The mixture was placed in a thermoshaker at 21.5°C for 30 min with a mixing speed of 1500 rpm. Following ligation, an identical three-rinse cycle was performed with R50. Adapter molecules that were not ligated to captured target readily de-hybridized, while ligation products remained bound to the particles. SA-PE (1 mg/mL) was diluted 1:50 in TET and added to obtain a final dilution of 1:500. Samples were incubated in a thermoshaker (1500

rpm) at 21.5°C for 45 min. After another three-rinse cycle, particles were additionally rinsed in 500 µL of PTET, and then suspended in a final volume of 50 µL PTET for scanning. Prior to use, all PTET was sonicated for 5 min to eliminate aggregations of polymer.

2.3.5 Rolling Circle Amplification (RCA) of Reporting Signal

Typical RCA assays were conducted in 0.65-mL snap-top tubes using a total reaction volume of 50 µL and a final NaCl concentration of 350 mM. For all preliminary experiments and calibration trials, a hybridization buffer (TET with NaCl), ~20 particles of each type, and appropriately diluted synthetic RNA target sequences were added (in that order) to the reaction tube. Depending on assay type, either 0.5 µL of TET or 0.5 µL of *E. coli* total RNA (200 ng/µL) was also added. Circular template for RCA was prepared using CircLigase (Epicentre Biotechnologies) and the protocol described in Schopf *et al.* [176]. Briefly, 5 µL of 50 µM linear DNA was added to a solution containing 40 µL of nuclease-free water, 6 µL of 10× CircLigase buffer, 3 µL of 1 mM ATP, 3 µL of 50 mM $MnCl_2$, and 3 µL CircLigase enzyme. After heating the solution to 62°C for 1 h, the circularization enzyme was deactivated by raising the incubation temperature to 80°C for 10 min. Then, 1 µL of Exonuclease I (New England Biolabs) was added, and the mixture was heated to 37°C for 90 min to remove any remaining linear DNA. Finally, the exonuclease was deactivated by heating the mixture to 85°C for 15 min. Following circularization, 7-µL aliquots of template were stored at -20°C for future use. The primer sequence and template used in this study were based on the system described in Schopf *et al.*, with an alteration made to the primer site to reduce hairpin melting temperature and optimize performance [176]. For the best results, circular template was used no more than six months after synthesis; template older than this showed reduced spot counts and thus decreased the limit of detection.

Target incubation was conducted at 55°C for 2 h. After target capture, particles were washed three times with R50, again using centrifugation to pull particles to the bottom of the tube for manual aspiration and exchange of carrier solution. For all rinses in this study, 50 µL of solution was left at the bottom of the tube to ensure retention of particles. A primer-modified universal adapter sequence was then ligated to all captured targets at 21.5°C for 30 min using T4 DNA ligase (New England Biolabs) and New England Buffer #2 (NEB2, New England Biolabs). This ligation procedure was identical to that described in Section 2.3.4, with the exception that the adapter in this case contained an additional primer sequence component. Following adapter ligation, particles were washed three times in R50 and circular template was added to give a final concentration of 50 nM. Template was allowed to anneal to the primer site during a 1 h incubation at 45°C, after which particles were washed two times in R50. Prior to the addition of the RCA reagents, particles were also washed with 235 µL of a gel-customized RCA buffer consisting of 10% 10× NEB2 and 90% TET solution. Bovine serum albumin (BSA, New England Biolabs), dithiothreitol (DTT, Epicentre), dNTPs (Epicentre), and Phi29 polymerase (Epicentre) were then added to give final concentrations of 200 µg/mL, 5 mM, 150 µM (of each dNTP), and 400 U/mL,

respectively. RCA was performed at 30°C for the desired extension time (usually 4 h), followed by three washes in R50. Two biotinylated reporter sequences were added to give a final concentration of 50 nM each and incubated with the particles for 1 h at 21.5°C. Particles were washed three times in R50 and incubated with 2.5 μL of a 1:50 dilution of SA-PE (1 mg/mL) for 1 h at 21.5°C. Finally, particles were washed three times in R50 and one time in PTET to prepare them for imaging analysis. All incubations in this section were carried out in a thermoshaker with a mixing speed of 1500 rpm.

2.3.6 Serum-based MicroRNA Assay

Sera taken from one healthy donor and from one donor with prostate cancer were obtained from BioServe Biotechnologies (donors were matched by age, sex, and race). Aliquots (25 μL) were prepared immediately upon receipt and kept frozen at -20°C until assay. For all assays, 22.5 μL of a modified TET incubation buffer was added to the serum to denature background proteins as well as RISC-associated proteins known to sequester miRNAs [127]. Assuming standard physiologic NaCl concentration of 150 mM in human serum [177], the TET incubation buffer was supplemented with appropriate amounts of NaCl, SDS, and Tween-20 to give concentrations of 350 mM, 2% (w/v), and 0.05% (v/v), respectively, in the final 50 μL reaction volume. To completely dissolve the SDS at this concentration, it was useful to immerse the mixture in a hot water bath maintained at 60°C, and to improve particle clarity in post-assay imaging, it proved beneficial to pass the resulting incubation buffer through a syringe-mounted 0.45-μm filter (Acrodisc 25 mm with Supor membrane, Pall Corporation). Following addition of the buffer to the reaction tube, each sample was heated to 90°C for 10 min and then allowed to cool for 2 min. Next, SUPERase-In RNase inhibitor (Applied Biosystems) was added to each sample to give a concentration of 0.5 U/μL in the final 50 μL reaction volume. Particles and synthetic RNA target were then added, and the samples were placed in a thermoshaker (1500 rpm) at 55°C for 2 h. The remainder of the assay was identical to the procedure described in Section 2.3.5. During optimization of the serum assay, the 90°C preheating step was found to be essential for eliminating nonspecific adsorption of material during target incubation, presumably due to its effective disruption and denaturation of background proteins.

2.3.7 Particle Analysis I: Static Fluorescence Imaging

For the fluorescence imaging of stationary particles after assay, 13 μL of PTET containing the processed particles was placed on a cover glass (24 × 60 mm, VWR), sandwiched with another smaller cover glass (18 × 18 mm, VWR), and imaged using a CCD camera (Andor Clara) attached to an inverted microscope (Zeiss Axio Observer) equipped with a 20× objective (Zeiss Plan-Neofluar, 0.5 NA), UV source (Lumen 200 at 100% setting), and filter set appropriate for the fluorescence imaging of SA-PE, rhodamine-acrylate, Cy3, and Alexa 532 (XF101-2, Omega). In order to obtain the best results possible, it was important to turn off all ambient light sources during fluorescence image acquisition. For non-amplified

labeling, the focus was adjusted to the mid-plane of the particle, the microscope's halogen shutter was closed, the microscope's fluorescence shutter was opened, and the CCD camera's acquisition was immediately triggered (0.05 s exposure time). The fluorescence shutter was closed as soon as acquisition had ceased to avoid photobleaching the reporter molecules. For RCA labeling, two primary image acquisitions were made for each particle: one with the focus adjusted to the top face of the particle and one with the focus adjusted to the bottom face. For completeness, a third image was also acquired with the focus set at the mid-plane of the particle.

2.3.8 Particle Analysis II: Fluorescence Scanning

Using the microscope setup described in Section 2.2.3, PTET was injected from a reservoir input into a PDMS device to serve as a focusing sheath stream for scanning analysis. For each trial, particle-bearing fluid was aspirated into a modified pipette tip using a syringe connected to the tip via Tygon tubing. With the illumination switching mirror directed towards the laser and the capture switching mirror directed towards the PMT, the tip was then inserted into the appropriate PDMS inlet port and a pressure of 8 psi was used to drive the flow of both fluids. Immediately before the initiation of flow, the fluorescence shutter on the microscope was opened and data acquisition was triggered with a custom Python script. A typical scan of 50 µl of particle-bearing fluid lasted ~30 s and used less than 25 µl of sheath fluid, with particle throughputs ranging from 5–25 per second, depending on the number of particles used in the assay. Devices were able to be used more than 25 times without degradation. Following each scan, a rinse solution of 30 µl 1× TE was flowed through the particle inlet to flush out stranded particles and thereby reduce inter-run contamination. Additionally, the loading tip was rinsed in ethanol and water so that it could be reused. As with the static imaging protocol, the best results were obtained when ambient lights were turned off during the scanning procedure. Furthermore, to protect the PMT sensor, it was important to keep the capture mirror directed towards the CCD (rather than the PMT) at all times, except immediately before and during signal acquisition.

2.3.9 Hydrogel Encapsulation and Lysis of Cells

A set of protocols was developed for the handling and lysis of cells in the context of hydrogel microparticle assays. For assays carried out in snap-top tubes, cells were introduced either as (1) gel-encapsulated entities within the probe regions of encoded particles (Figure 2.3) or as (2) groups of 500–50,000 cells that were added directly to the reaction tube in a manner similar to that used for synthetic target spiking in Section 2.3.4. For these assays, cultured HeLa cells were trypsinized, harvested, and stored at concentrations between 1 x 10^6 per mL and 6 x 10^6 per mL in Dulbecco's Modified Eagle's Medium (DMEM) with 10% fetal bovine serum (FBS). The cells were then washed with three 500-µL volumes of PBS with 1 mg/mL BSA. For the assay of large groups of un-encapsulated cells, 0.5–2 µL of the cell

solution was added to a reaction tube containing lysis buffer and particles, with lysis and target capture occurring simultaneously during the same 90 min incubation at 55°C.

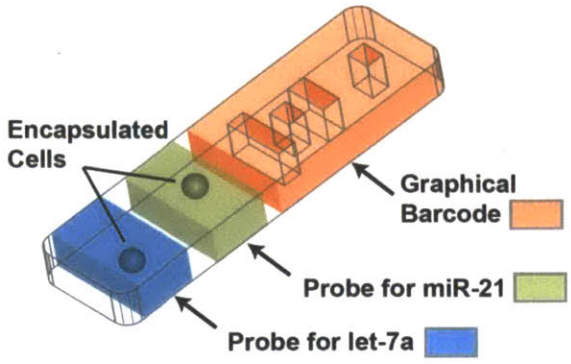

Figure 2.3: *Schematic of the cell encapsulation strategy. Cells were physically entrapped within the probe regions of encoded gel particles during SFL synthesis for subsequent lysis during assay. Transparent regions represent blank sections that contain neither probe nor fluorophore.*

For encapsulation studies, the cell solution was added to a 5-μL aliquot of the appropriate acrylate-modified DNA probe. Then, a monomer mixture consisting of PEG-DA_{700}, PEG_{200}, and Darocur 1173 was added to produce a final concentration of 50–100 μM DNA probe, 20–30% (v/v) PEG-DA_{700}, 30–40% PEG_{200}, 5% Darocur 1173, and ~2,000 cells per μL. It is important to note that following centrifugation of cells during washing steps, it was crucial to manually disperse the cell pellet that was produced by vigorous manual mixing of the solution using a pipette; simply vortexing the pellet did not disperse it fully and led to inaccurate cell dilution. In addition, the use of 1 mg/mL BSA in the wash buffer was found to be important to prevent cell adhesion to tubes and pipette tips. Trypan blue staining was used to monitor cell viability at each step in initial trials to ensure that the protocol was not compromising the cell membrane prior to encapsulation with SFL [178].

Following the mixing of the cell-laden prepolymer, the solution was loaded into a modified pipette tip. To ensure that cells were not clumped together, it was best to repeatedly draw the solution up with a syringe and eject it back into the loading tube five times before inserting the tip into the PDMS device. Synthesis devices with 50-μm and 100-μm wide inlet channels were both used, and it was observed that the 100-μm inlets were advantageous for the cell work as they did not clog nearly as frequently as the 50-μm inlets. Although the cell loading concentration could be raised above 2,000 per μL, this would also increase the chances of a clogging event. Aside from the use of a slightly different channel geometry and the alteration of the prepolymer composition, the SFL protocol for the

encapsulation of cells within the gel particles via UV-induced crosslinking was the same as that described in Section 2.3.3. After particle harvesting and the standard TET and PEG_{200} rinses described earlier, the cell-laden microgel particles were loaded into a single well of a filter plate (Whatman 96-well polystyrene plate with pore size of 25 μm and well volume of 800 μL), and a vacuum manifold was used to pull through the carrier liquid and any unincorporated cells that remained, leaving only the microparticles in the dry well. The well was then immediately rehydrated with 700 μL of TET and the filtration was repeated two more times. Following the third rinse, the well was filled with 700 μL TET, the solution was manually mixed ten times with a pipette to remove particles from well surfaces, and the entire liquid volume was transferred to a snap-top tube for further processing. This filtration was found to be effective for separating the microgel particles from unincorporated cells and was also observed to be very important for producing clean, non-fouling particles during subsequent assay. Particles containing encapsulated cells were added to snap-top tubes containing lysis buffer, and lysis and target capture were carried out simultaneously during the same 90 min incubation at 55°C.

An optimized lysis buffer was developed to ensure rapid denaturation and digestion of cellular protein so that miRNAs could be released from sequestration and captured on gel-embedded probes with the labeling protocols described in Section 2.3.4 and Section 2.3.5. The final formulation of this buffer consisted of TET with final concentrations of 350 mM NaCl, 2% (w/v) SDS, 1% (w/v) BSA, 200 μg/mL proteinase K (PK, New England Biolabs), and 0.5 U/μL Superase-In RNase inhibitor (Invitrogen). It was important to pass this buffer through a syringe-mounted 0.45-μm filter to reduce the likelihood of clumps of debris in later stages of the assay. When using SDS and PK in the lysis buffer with the RCA labeling protocol, it was crucial to use biotinylated dNTPs (bio-dNTPs) rather than biotinylated labeling oligonucleotides for the attachment of SA-PE in order to avoid non-specific fouling on the particles (see Section 6.2.2).

In the modified bio-dNTP protocol, labeling was carried out in the same manner described in Section 2.3.5 up to the point at which the RCA mixture is added. In the bio-dNTP protocol, a master mix of unmodified dNTPs (New England Biolabs) and bio-14-dNTPs (Invitrogen) was prepared with the following composition: 1 mM dGTP, 1 mM dTTP, 840 μM dATP, 840 μM dCTP, 200 μM biotin-14-dATP (Invitrogen catalog number 19524-016), and 200 μM biotin-14-dCTP (Invitrogen catalog number 19518-018). After the addition of BSA, DTT, and Phi29 enzyme, 1 μL of this master mix was added to the 50-μL volume of the reaction tube. Nucleotide concentrations and the ratio of labeled-to-unlabeled nucleotides were chosen to match the vendor's suggested conditions for polymerase incorporation. RCA was carried out at 30°C in a thermoshaker (1500 rpm) for 14 h, after which the particles were washed three times with R50. A 6M urea solution in TET was created, and 3 mL of the resulting solution was mixed with 7 mL of R50 to create a 30% urea mixture. After passing this mixture through a 0.45-μm filter, 5 μL of the mixture was added to the ~50 μL volume in the reaction tube, and the contents were incubated at 37°C for 1 h in a thermoshaker (1500 rpm). Upon removal from the thermoshaker, the particles

were washed twice with R50, and SA-PE (1 mg/mL) was diluted 1:50 in TET and added to obtain a final dilution of 1:1000. The particles were then processed for fluorescence imaging in the same manner as described in Section 2.3.5.

2.3.10 Microwell Confinement Assay

PDMS microwell arrays with well depths of 46 and 113 μm were produced from separate master wafers made at the BMRC. To facilitate magnetic manipulation, molds were only poured to a depth of about 1.5 mm (as opposed to the 5 mm depth used for other molds) by using a mixture of 1 g PDMS curing agent and 10 g PDMS base. Molds were typically used for assay within three days of their creation, and incubation buffers were always made fresh for each detection experiment. Buffer M1 (TET with 350 mM NaCl, 1% BSA, 2% SDS, and 200 μg/mL PK) and buffer M2 (TET with 350 mM NaCl, 1% BSA, 4% SDS, and 400 μg/mL PK) were created in 15-mL Falcon tubes and used for calibration and cell-based trials, respectively. To completely dissolve the SDS at these concentrations, it was useful to immerse the mixture in a hot water bath maintained at 60°C, and to improve particle clarity in post-assay imaging, it proved beneficial to pass the resulting incubation buffer through a syringe-mounted 0.45-μm filter (Acrodisc 25 mm with Supor membrane, Pall Corporation). For calibration studies, a dilution series of appropriate synthetic targets was prepared using buffer M1 as the diluent. The desired microwell design was excised from the wafer mold with a scalpel and placed feature-side upwards on a clean glass slide (24 × 60 × 1 mm, VWR) that was then inserted into a plasma oven. A vacuum pump was used to evacuate the oven for 60 s, at which point a 45-s UV treatment at the low Rf setting was performed. Although this degree of plasma treatment only slightly improved the wettability of the PDMS surface, higher Rf settings or longer treatments at the low setting were observed to create an irreversible bond between the PDMS surface and the hydrogel microparticles, thus preventing particle collection after assay.

For calibration trials with synthetic spikes, the wells were immediately transported to an inverted microscope following plasma treatment, where 7 μL of buffer M1 and 0.3 μL of Superase-In were deposited on the center of the thin PDMS slab. With the halogen lamp at the lowest possible setting to prevent evaporation of the deposited liquid, the wetting of the microwells was monitored with the 5× objective. After 5 min, 0.5 μL of magnetically-functionalized particles (stored at ~12.5 particles/μL) were gently added to the wetted portion of the PDMS, and a thin rectangular hand magnet attached to the end of a screwdriver was maneuvered underneath the stage to direct particles into wells. By controlling the angle of the magnet, particles could be dragged through solution with their broad faces or their thin edges lying flush with the PDMS surface [179]. All particles were typically inserted into wells within 2 min of particle injection.

For the introduction of synthetic miRNA targets, 7 μL of target appropriately diluted in buffer M1 was repeatedly injected into and withdrawn from the droplet lying on the

PDMS. This process was repeated at least ten times to mix the delivery and wetting fluids for even dispersal of target. After the tenth cycle, the fluid in the pipette was emptied onto the PDMS, and the slide was removed from the microscope and placed into the bottom holder of a microarray hybridization chamber (Agilent). A second glass slide (24 × 60 × 1 mm) was placed on top of the PDMS, the chamber's top holder was inserted, and the chamber was then secured tightly with the thumb screw. For a tight seal without deforming the wells, it was best to turn the thumb screw only until resistance was encountered. The chamber was then placed in a small oven kept at 55°C for 90 min for target capture.

Following incubation, the thumb screw and top holder were removed, and the glass-PDMS-glass assembly was transferred to the microscope stage. Once the top glass slide was removed, 15 μL of R50 was immediately deposited onto the PDMS surface, and 15 μL of R50 was also placed onto the underside of the glass slide. This was done to maintain hydration of the particles so that they would not stick to the substrates. For particles remaining in the wells, 15 μL of R50 was pipetted into the wells to eject particles, which could then be collected by aspirating the liquid from the top of the PDMS. For particles retained on the glass slide, it was often necessary to gently scrape them from the surface with a pipette tip in order to aspirate them. All collected particles were then deposited in a 0.65-mL snap-top tube containing R50, rinsed, and processed either with non-amplified ligation labeling or RCA as in Section 2.3.4 and Section 2.3.5, respectively.

For cell assay within the microwells, cultured HeLa cells were trypsinized, harvested, and stored at concentrations between 1 x 10^6 per mL and 6 x 10^6 per mL in Dulbecco's Modified Eagle's Medium (DMEM) with 10% fetal bovine serum (FBS). Depending on the desired cell density, 5–60 μL of cell solution was added to 2–4 mL of TET with 150 or 350 mM NaCl and 1% BSA. Then, 7 μL of this mixture and 0.3 μL of Superase-In were deposited onto a clean, plasma-treated PDMS slab. After waiting 5 min for the wells to wet and for the cells to settle, 0.5 μL of particles (stored at ~12.5 particles/μL) was gently added. Next, 7 μL of buffer M2 was manually mixed into the deposition droplet in a manner identical to that described above for the synthetic target. Thorough mixing was crucial to ensure even distribution of the lysis agents contained within buffer M2. Subsequent well sealing, incubation, and particle extraction/processing for the cell-based assays proceeded exactly in the manner described earlier for calibration trials. It should be noted that the two protocols (one for calibration with synthetic spikes and one for cell-based assays) and the two buffers (M1 and M2) were designed to produce the same final concentration of reagents within the sealed wells (350 mM NaCl, 1% BSA, 2% SDS, 200 μg/mL PK, and 0.5 U/ μL Superase-In).

Chapter 3

High-throughput Flow Alignment of Hydrogel Microparticles

Suspension (particle-based) arrays offer several advantages over conventional planar arrays in the detection and quantification of biomolecules, including the use of smaller sample volumes, more favorable probe-target binding kinetics, and rapid probe-set modification. In this chapter, we present a microfluidic system for the rapid alignment of multifunctional hydrogel microparticles designed to bear one or several biomolecule probe regions, as well as a graphical code to identify the embedded probes. Using high-speed imaging, we have developed and optimized a flow-through system that (1) allows for a high particle throughput, (2) ensures proper particle alignment for decoding and target quantification, and (3) can be reliably operated continuously without clogging. A tapered channel flanked by side focusing streams is used to orient the flexible, tablet-shaped particles into a well-ordered flow in the center of the channel. The effects of channel geometry, particle geometry, particle composition, particle loading density, and barcode design are explored to determine the best combination for eventual use in biological assays. Particles in the optimized system move at velocities of ~50 cm/s and with throughputs of ~40 particles/s. Simple physical models and CFD simulations have been used to investigate flow behavior in the device.

3.1 Introduction

The ability to accurately detect and quantify biological molecules in a complex mixture

is crucial in both basic research and clinical settings. Advancements in the fields of genomics and proteomics require robust technologies that can obtain high-density information from biological samples in a rapid and cost-effective manner [2, 4-6]. High-throughput screening for genetic analysis, combinatorial chemistry, and clinical diagnostics benefits greatly from multiplexed analysis, which is the simultaneous detection of several target molecules [7, 8]. This approach significantly reduces the required assay time, sample volume, and cost. However, it requires an encoding scheme that can be used during analysis to identify immobilized probe species.

Particle-based assay platforms exhibit several advantages over planar arrays in applications that involve the detection of low to medium target densities (1–1000), demand rapid probe-set modification, or necessitate high-throughput processing of samples [26]. Compared to planar arrays, the use of micrometer-sized particles leads to faster probe-target binding kinetics due to mixing during incubation, more efficient separation and washing steps, and higher degrees of reproducibility [31, 32]. The vast majority of particles used in suspension arrays are optically encoded latex microspheres with diameters between 0.3 and 10 μm that can be interrogated and decoded with laser-based flow cytometry. Optical encoding is accomplished by swelling the spheres with fluorescent organic dyes with different emission spectra. Although used extensively, this scheme requires multiple excitations and is limited to the multiplexed sensing of only ~500 analytes due to spectral overlap of encoding and analyte-detection fluorescence [27, 50]. Submicrometer rods with multiple metal stripes that serve as a graphical code for multiplexing have also been developed, but the high density of such rods leads to rapid settling in solution and thus requires the rods to be vigorously mixed during assays, a procedure which can damage fragile biological molecules like antibodies [33, 48]. Moreover, a feasible high-throughput quantification and decoding strategy for the rods has never been introduced, thereby significantly limiting their applicability in clinical or research settings.

Recently, innovations in gel-based microchips were combined with suspension array technology to create multifunctional, graphically-encoded hydrogel microparticles for biomolecule analysis [23, 52]. Implementing photolithography and microfluidic-based techniques, geometrically and chemically complex microparticles were rapidly synthesized (10^4 per hour) with high reproducibility from co-flowing streams of UV-curable monomers [160]. Synthesis, encoding, and functionalization of the particles occurred in a single step, with unpolymerized holes in the wafer structure used to construct a 20-bit fluorescent "barcode" region. Multiplexed detection of fluorescently labeled DNA oligomers was demonstrated with high specificity, high sensitivity, and short hybridization times. Nonspecific binding in multiplexed assays was minimized through the use of a biocompatible and non-fouling PEG polymer scaffold. Compared to the surface immobilization strategies employed with planar arrays and latex microspheres, the immobilization of probe molecules in a three-dimensional gel structure leads to more favorable hybridization kinetics due to the hydrated

environment, high probe-loading densities, and decreased steric hindrance [174, 180]. Furthermore, the physical separation of code and probe regions on each particle enables the use of a common fluorophore for all signalling purposes, thus avoiding the spectral issues that limit the multiplexing capacity of the optical encoding schemes discussed earlier and also reducing the costs associated with detection equipment. Although flow-through scanning was demonstrated for a limited number of encoded hydrogel particles, the processing rate was low (<1 particle/s) and therefore not suitable for high-throughput applications [52]. Robustness of the device was also not explored.

Originally developed in the 1950s to count cells, flow cytometry has become a versatile tool for the rapid interrogation of the synthetic microparticles used in suspension arrays [51, 56, 181]. Compact and inexpensive molded microfluidic cytometers made of the silicone elastomer PDMS have been developed for particle sizing, as well as single-line fluorescence detection [60, 61]. The ability to achieve well-ordered flows with uniform particle velocity and passage time is essential for accurate detection and characterization in such devices. The most common method of directing the particles through the channel involves the hydrodynamic focusing of the particle-bearing stream with secondary sheath flows [63, 67]. Recent advances have led to high-throughput and high-resolution cytometers capable of three-dimensional hydrodynamic focusing [62, 64].

In order to extend the barcoded hydrogel platform to real-world applications in high-throughput screening, we seek to develop a robust microfluidic approach to the rapid interrogation of each particle. We present a parametric study to understand the various geometric, mechanical, and operating factors that govern the system's performance. The inclusion of properly-spaced side-focusing streams, the use of a sufficiently wide detection zone, the modulation of particle cross-link density and morphology, and the choice of particle loading concentration were identified as the most crucial elements. We demonstrate here a new system that implements the design principles distilled from this study and thereby is capable of reliably manipulating the relatively large and flexible hydrogel particles into a single-file, high-velocity procession without clogging or deformation. The ability to align particles in the channel with high precision will enable PMT-based detection with a simple one-dimensional line scan that integrates fluorescence intensity along a thin excitation beam established perpendicular to the flow direction of the particle. The resulting profile could then be used to reconstruct the identity of the particle as well as the extent of the binding events on the various probe and control regions.

3.2 Theory

The tablet-shaped hydrogel particles investigated here are substantially larger (250 × 80 × 35 μm, Figure 3.1) and more flexible than the latex microspheres commonly used in other suspension arrays. This introduces additional design considerations regarding flow velocity and mechanical stress. Pressure-driven flow is used to carry the particles through rectangular PDMS channels, while sets of side streams and abrupt contractions

in width serve to orient the particles prior to their entrance into a narrow "detection zone." In a rectangular channel with a high cross-sectional aspect ratio, it is expected that a parabolic velocity distribution will develop along the small dimension. This flow profile can inhibit the performance of cytometers by generating nonuniform particle velocities. Although the short dimension can be further reduced to physically confine the particles, this lowers flow velocity and throughput. Higher driving pressures could be used to counteract these decreases, but such an approach may lead to deformation of the channel and/or the particles. While the velocity distribution in the long cross-sectional dimension will be nearly uniform in the center of the channel, large gradients will develop in a boundary layer near the wall. Particles passing through this layer will be slowed significantly. Focusing streams and periodic contractions in channel width could be used to disturb the developed flow along the walls and eject particles into the central flow region for better cytometric performance. It has previously been shown that rapid decreases of channel cross-section can enhance the focusing of deformable blood cells by introducing regions of high shear rate adjacent to the walls that produce strong hydrodynamic lift forces [182].

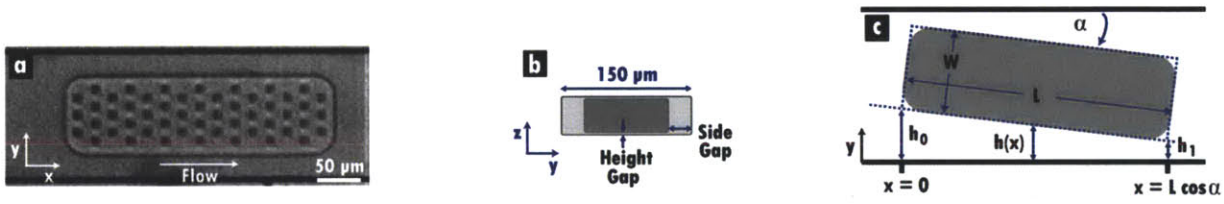

Figure 3.1: *Particle flow in rectangular channels. (A) Image from high-speed movie of model particle flowing "lengthwise" at 30 cm/s from left to right in 150-μm wide channel. Columns of coding holes run in the y-direction, while rows run in the x-direction. (B) Cross-sectional schematic of the particle in (A). The height gap is ~1–2 μm in the studies presented. The larger side gap permits significant bypass flow, thus leading to bulk fluid velocities that are higher than particle velocities. (C) Schematic of pertinent variables for application of the lubrication approximation to analyze lift forces and torques on misaligned particles in channel regions where side-gap flow is nearly unidirectional.*

The pressure-driven flow of both rigid and flexible disk-shaped bodies in parallel plate channels has been used to model the behavior of red blood cells in certain microvessels in which cell and passage heights are nearly equal [183, 184]. Although the mechanical properties of cells and hydrogels differ in some aspects, many of the effects observed in these studies are relevant to the current investigation. For flexible bodies that deform at constant volume and surface area, it was found that the pressure in the thin "height gaps" above and below the body (Figure 3.1 B) will be uniform. Small deformations in the body height were shown to produce a gap distance that varied with spanwise (y) position only; the gap distance was constant along lines parallel to the flow. Cell velocity was predicted to be much less than that of the bulk fluid for channels with small height

gaps and with spans much larger than cell width. This effect can be attributed to the ability of the fluid to easily bypass the cell by moving through the relatively large "side gaps." In contrast, for tightly fitting bodies in cylindrical tubes, the driving pressure is concentrated across the particle, leading to bulk fluid velocities that are lower than body velocities and even "leakback" of fluid [185].

A thorough understanding of the hydrodynamic forces that act on the particles in the channel is crucial for the development of an effective cytometry system. For the narrow detection portions of the channel a lubrication approximation can be utilized to determine the lift forces on a particle that arise from the bypass flow in the side gaps just described (see Section 3.6 for full derivation). This analysis can be used to rationally design a particle and a channel that will give rise to forces and torques that most effectively position and align the particle for proper scanning. In a reference frame moving with the particle, the fluid velocity and pressure drop in the side gap are given by:

$$v_x(x,y) = \frac{y}{2\mu}\frac{dP}{dx}(y - h(x)) + U_w\left(\frac{y}{h(x)} - 1\right) \qquad \text{Equation 3.1}$$

$$\frac{dP}{dx} = -\frac{12\mu q}{h(x)^3} - \frac{6\mu U_w}{h(x)^2} \qquad \text{Equation 3.2}$$

where μ is the dynamic viscosity, P is the dynamic pressure, U_w is the wall velocity, and q is the volumetric flow rate per unit width (see Figure 3.1 C for other definitions). The geometric and dynamic criteria required for application of the lubrication analysis become $\tan\alpha << 1$ and $(q/v)\tan\alpha << 1$ [159]. Neglecting deformation and any three-dimensional effects from flow in the height gap, these conditions are met by the nearly unidirectional bypass flow established in the side gaps when an oblong particle is passing through the relatively narrow regions of the channel at small α. In analyzing the stress exerted by the fluid on a rigid particle surface, the normal viscous stresses are zero, and the components of the stress vector are thus given by:

$$s_x = -\frac{dh}{dx}P - \mu\frac{\partial v_x}{\partial y} \qquad \text{Equation 3.3}$$

$$s_y = P. \qquad \text{Equation 3.4}$$

The torque (per unit width) about $\mathbf{r}_0$ can be calculated as

$$\mathbf{G} = \int_{x_1}^{x_2} (\mathbf{r} - \mathbf{r}_0) \times \mathbf{s}(\mathbf{n})\, dx. \qquad \text{Equation 3.5}$$

Meanwhile, the rotational and translational tendencies of particles in the wider regions of the channel (*i.e.*, upstream) are best understood by the principle of gradient minimization, which dictates that the oblong particles will tend to rotate until the velocity gradient across their rear surface can no longer be reduced. For rectangular particles with high aspect ratios, this condition will be met once the short and long dimensions have been oriented perpendicular and parallel, respectively, to the flow direction. The large particles used in the study are expected to impact the time scale of this orientation process by altering local velocity profiles and generating significant wake flows in areas of high particle concentration.

3.3 Process Design

The success of high-throughput microparticle scanning depends on *both* the fluidic channel design and the particle morphology. We took a three step approach to independently study these two facets of the project and optimize the process. First, using a canonical microparticle design we explored a variety of operating conditions and channel designs with the aim of minimizing clogging and disruptive particle-particle interactions in the detection zone. Next, particle size and composition were varied to explore the impact on alignment tendency and mechanical stability. Finally, the operational limits of a revised particle design suitable for bioassays were studied to maximize throughput and success rate while also maintaining a high degree of reproducibility; additional modeling and analysis of these particles were conducted to further understand the complexities of their behavior in high-speed flows. A "successful" scan was defined to be one in which the horizontal distance between the center of any two holes in a given column of the code region was less than 5 μm. In addition, particles with any measurable lateral (y-direction) drift were deemed "unsuccessful" passages. This conservative definition of success is based on the PMT sampling rates (0.1–1 MHz) and excitation beam width (1–5 μm) required for fluorescence scanning procedures. Quoted throughput values include both successful and unsuccessful particles, and unless otherwise noted, each flow trial involved the measurement of 100 particles.

3.3.1 Channel Design

The effects of detection-zone width (w_d), side-stream number (N), side-stream spacing (L_f), and forcing pressures were studied for a fixed particle design (Figure 3.2). All particles used in channel optimization were photopolymerized from DA20 prepolymer (Table 2.1), had dimensions of 270 × 90 × 33 μm, and featured 10 × 10 μm code holes spread evenly throughout the particle (Figure 3.1 A). The composition was selected based on its performance in earlier assay optimization studies [52], while the hole design was chosen for its symmetry and for its use in alignment measurements. Loading concentration was fixed at 10 particles/μL.

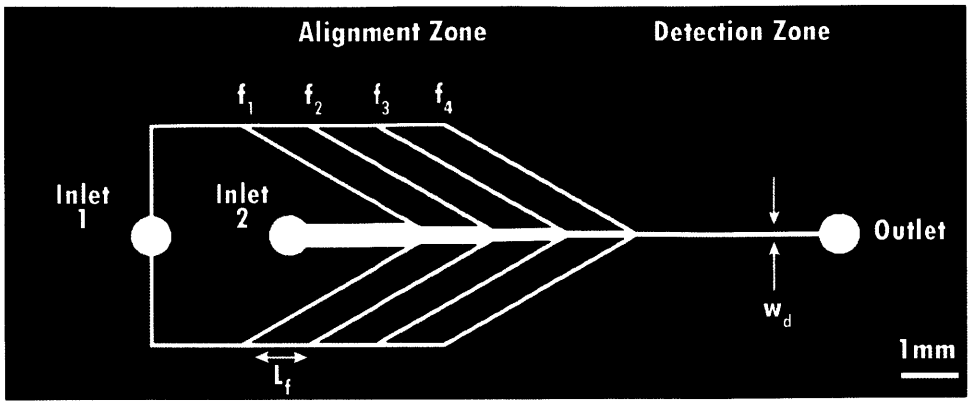

Figure 3.2: *Particle flow device. Schematic of a "4-focus" device, with four sets of side streams (N = 4), each separated by L_f = 1000 μm. Sections of constant width (450, 350, 250, 150, and 125 μm) are broken up by abrupt contractions. Sheath flow is introduced through inlet 1, while the particle-bearing fluid is introduced through inlet 2. The detection zone is the region in which the particle velocity, alignment, and position are evaluated to determine if a passage is successful. The measurement point was 750 μm from the outlet for all flow trials.*

Initial trials were performed with a simple channel design with one set of side streams ("1-focus device," $N = 1$). The central channel decreased in width from 500 to 100 μm at the meeting point of the side streams, producing a large velocity gradient in the flow direction. The detection zone was 2.3 mm in length, with w_d = 100 μm. The forcing pressures of the particle and sheath streams were matched, and they varied between 4 and 9 psi. Average particle velocities for this pressure range were between 10 and 30 cm/s. Analysis of the detection region revealed a tendency for particles to appear in clusters with poor alignment and slight deformations of the leading and trailing particle edges. Moreover, flow in the channel would temporarily decrease at times, producing wild variations in particle velocities over short periods of time.

These observations implied that the particles were jamming at the contraction point of the channel. Subsequent investigation of this region revealed periodic instances in which groups of 2–5 particles traveled closely together and lodged tightly in the contraction zone, thus impeding flow and leading to an accumulation and compression of particles. After 100–1000 ms, the elastic hydrogels would eventually squeeze past one another and eliminate the blockage, producing the clumps observed further downstream. It should be noted that the clogging never led to permanent (plastic) deformation. Particles collected in an exit reservoir did not exhibit any substantial structural abnormalities. Seeking a more gradual contraction with improved particle conditioning, additional trials with 2- and 3-focus devices with w_d = 100 μm and L_f = 400 μm were performed. The frequency and duration of the blockage events were reduced,

but only by small amounts. Observations of the flow patterns in the 500-μm width region of 1-focus devices revealed a tendency for some particles to travel slowly along channel walls. Such behavior is consistent with the flow profile of a channel with a high aspect ratio, as discussed earlier. Although the same observations were made in the 500-μm wide regions of the 2- and 3-focus devices, the "wall-huggers" in these channels were reliably coerced off the wall prior to the detection zone by the local velocity increase created by the impinging side streams.

It was postulated that increasing L_f from 400 to 1000 μm would better enable particles to adopt a lengthwise flow orientation prior to the shorter contraction points at which clogs were ocurring. This was based on the belief that rotation into the lengthwise orientation arose from a tendency for the particle to minimize the velocity gradient of the flow impinging upon it. The disordered flow patterns in the wakes of particles severely limited this effect, making congested areas less likely to produce well-aligned particles. Trials with larger L_f seemed to confirm this hypothesis. Based on observations of both upstream and detection zones, the longer residence time of the particles in the wide portions led to a nearly complete elimination of blockage events and drastic velocity variations in a modified 3-focus device with L_f = 1000 μm. However, deformations of particles traveling through the detection zone persisted, especially at higher forcing pressures. Particles approaching the final width contraction (200 to 100 μm) in the 3-focus device were seen to distort violently if they approached the contraction from a position far from the centerline of the channel. Furthermore, the small side gap between the particle and channel walls (5 μm on each side) led to a large pressure drop across the particle length and introduced substantial lift forces that compressed the particle in the direction perpendicular to flow and elongated it in the direction parallel to flow (~10% increase in length). Although such deformation could potentially increase the resolution of the proposed line scans, it was determined that future channels would have detection zones roughly twice as wide as the particle to preserve particle morphology by increasing bypass flow and lowering the pressure drop. In short, this study revealed the need for multiple sets of side streams separated by a sufficient distance, as well as a detection zone width that permitted substantial bypass flow for shape preservation.

3.3.2 Particle Design

The control over hydrogel morphology and composition permitted by SFL is a valuable tool for design. The alignment of the tablet-shaped particles observed in initial experiments was far more reliable than that of additional morphologies that were also investigated (oblong particles with pointed ends, as well as tear-drop and bullet shapes). As a result, the 3-focus design with L_f = 1000 μm was adopted for the parametric study of the tablet-shaped particles. All studies detailed in this section were performed with w_d = 150 μm and a pressure of 9 psi for both inlets, leading to particle velocities of 25–35 cm/s.

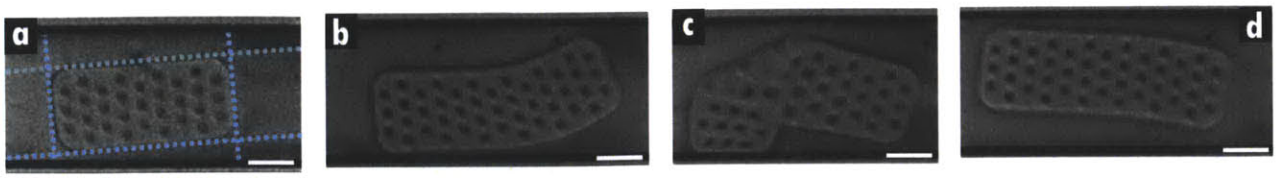

Figure 3.3: *Primary failure modes of DA20 particles in detection zone with w_d = 150 μm. (A) 190 × 90 μm particle (AR = 2.11) with poor alignment. (B–D) 270 × 90 μm particles (AR = 3.00) with drastic deformations that would preclude reading of the barcode. Scale bar in all images is 50 μm.*

	Aspect Ratio	Success Rate	Mean Dist From Centerline (μm)	Main Failure Mode
DA20	2.11	91%	4.5	Lateral movement
	2.56	95%	2.6	Front deformation
	3.00	82%	3.2	Front/back deformation
	3.44	99%	1.4	None
DA30	2.11	82%	9.2	Lateral movement
	2.56	94%	6.9	Lateral movement
	3.00	88%	6.5	Poor alignment
	3.44	100%	3.6	None

Table 3.1: *Effect of AR on particles in device with N = 3 and w_d = 150 μm.*

The effect of particle aspect ratio (AR) was explored by flowing 90-μm wide particles (DA20 composition) with four different lengths: 190, 230, 270, and 310 μm. Flow trials involved measuring the lateral position and success rate of 100 particles of each type (Table 3.1). The position was calculated as the distance from the center of the particle to the centerline of the channel. It was observed that several of the shortest particles, AR = 2.11, exhibited significant lateral movement and had slanted front and rear edges upon reaching the detection zone (Figure 3.3 A). Particles with AR = 2.56 flowed more closely along the centerline of the channel and with virtually no lateral movement, but several had leading edges that were slightly blurred or compressed at driving pressures of 9 psi. Particles with AR = 3.00 exhibited drastic deformations (Figure 3.3 B–D), leading to the lowest success rate of the four particle types. In many instances, the front edge of the particle was bent towards one of the walls, thereby disrupting the alignment of the holes in the code region. This phenomenon is qualitatively similar to the deformations of tightly fitting red blood cells in two-dimensional channels. In the case of cells, the bending arises to reduce the driving pressure needed to sustain a certain cell velocity [186]. Several particles (10%) with this AR also exhibited curved side walls. The particles with AR = 3.44 suffered from none of the problems that plagued the other designs. The sole failure in this trial was one particle that was twisted into a U-shape.

The results of these trials indicated two potential sources of failure. At low AR, there was a reduced tendency to orient into and maintain a flow alignment that was

conducive to scanning. As discussed earlier, the generation of lateral forces in the small side gap between the channel wall and the particle edge will tend to rotate the particle into an orientation such that the major axis of the particle is aligned with the centerline of the channel. This effect becomes more pronounced as the particle length-to-channel width ratio (b) becomes larger. Longer particles experience a larger net torque, and smaller side gaps generate greater lift. Meanwhile, failures of a different nature arose at more moderate AR. Particles with mid-range AR achieved the desired orientation and position within the detection zone, but they were more susceptible to deformations of their leading edges. A visual inspection of the particles entering the final contraction in the 3-focus device revealed that many of the particles of mid-range AR were poorly oriented and thus forced to bend significantly to enter the more narrow detection width. In contrast, particles with the lowest AR resisted such deformation and were able to enter with imperfect alignment due to their smaller size. Particles with the highest AR were already aligned sufficiently so that they did not experience distortion upon their entrance into the detection zone.

It is well known that the mechanical strength of a hydrogel depends to a great extent on the number and nature of the cross-links present [173]. By using a prepolymer with a higher proportion of crosslinking monomer (PEG-DA), it should be possible to generate hydrogel particles with higher cross-linking densities that are more resistant to deformation. The AR study was thus repeated with particles polymerized from DA30 prepolymer (Table 2.1) to investigate effects on flow characteristics. Atomic force microscopy (AFM, Agilent Technology) was used to probe the mechanical properties of the particles. An optical microscope (IX 81, Olympus) was employed to position AFM cantilevered probes above particle samples. Calibration of AFM cantilevers of nominal spring constant $k = 0.01$ nN/nm and probe radius $R = 25$ nm (Veeco) was conducted. Briefly, inverse optical lever sensitivity (nm/V) (InvOLS) was measured from deflection-displacement curves recorded on rigid glass substrates. For each measurement of elastic modulus, at least 25 replicate indentations were acquired to maximum depths of 20 nm. Acquired probe deflection-displacement responses were converted to force-depth responses using measured spring constants and InvOLS (Scanning Probe Imaging Processor, Image Metrology). Elastic moduli, E, were calculated by applying a modified Hertzian model of spherical contact to the loading segment of the force-depth response with the scientific computing software Igor Pro (Wavemetrics).

From AFM measurements on particle regions *without* coding holes, the elastic modulus of the DA20 hydrogel was found to be 10.1 ± 0.4 kPa, while that of the DA30 hydrogel was found to be 19.6 ± 1.2 kPa. The impact of the added rigidity of the DA30 particles was noticeable, with significantly less deformation at all values of AR (Table 3.1). DA30 particles did not exhibit the bent leading edges, curved side walls, or compressions that plagued the softer DA20 particles. Observations of the final contraction revealed particles with no perceptible shape changes, in sharp contrast to the DA20 case.

While the higher cross-linking density solved one flow problem, it seemed to exacerbate the other. The stiffening of particles with ARs of 2.11 and 2.56 led to an increase in poorly aligned particles that were also more susceptible to moving laterally in the detection zone (Figure 3.4). The use of DA30 raised the success rates of the two higher ARs, but actually led to a decrease in the success rates of the two lower ARs. In the case of DA30 particles with ARs of 2.11 and 2.56, the additional rigidity arising from higher cross-link density, when combined with the compact morphology, leads to a regime of rigid-body motion within the channel. This effectively eliminates the temporary hydrogel deformations induced by the surrounding focusing flow that play a significant role in coercing the particle into the preferred position and alignment. Any attempt to tune the flow behavior with this design parameter must balance the desire for structural integrity with the need for efficient focusing and orientation by hydrodynamic forces. Thus, the best particle design will have a high aspect ratio and a stiff gel network.

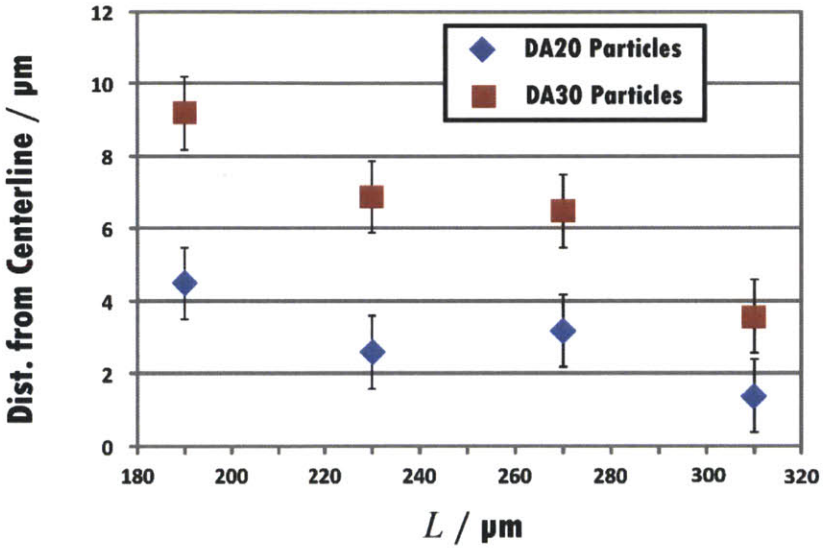

Figure 3.4: *Lateral position of particle (W = 90 µm) in detection zone with w_d = 150 µm. This plot demonstrates the difference in position for particles of different lengths and compositions. At all lengths, the softer DA20 particles exhibit superior positioning and a reduced tendency to move laterally. Longer particles are observed to settle into stable flow trajectories closer to the centerline than shorter particles. Each point represents 100 particles, and all measurements were made from channel centerline to the central-most point of the particle.*

3.4 Barcoded Particle Optimization

The channel and particle motifs with the best performance characteristics were selected to create a flow-through system that could be operated reliably at high-throughput with hydrogel designs that were capable of extracting and displaying information from

bioassays. Three different channel designs (A, B, C) were used (Table 3.2), each with L_f = 1000 μm. The shape and composition of the hydrogel particle were altered to ensure proper alignment, durability in high-velocity flows, and compatibility with bioassays. Using new masks and SFL, 9 μm × 9 μm holes were limited to one half of the particle, thus creating a "probe" region and a "code" region (Figure 3.5 A). Columns and rows of holes were separated by 9 μm. This design allows the capture and quantification of target(s) on one end and the display of probe identity on the other[52]. To create "bifunctional" particles, the code region was polymerized from DA30 to ensure mechanical stability, while the probe region was polymerized from DA20 to produce a pore size consistent with that featured on particles employed in high-sensitivity assays in previous work [52, 174]. Furthermore, the use of DA20 imparted a flexibility that would aid in orientation within the channel, as seen in the earlier particle study. The new particles were 235 × 65 × 35 μm and featured a redesigned hole setup capable of 3,072 distinct codes. The AR of this design (3.62) was higher than any used in previous flow trials.

Name	w_d (μm)	Side stream sets, N	Upstream widths (μm)
A	100	4	450, 350, 250, 150, 100
B	125	4	450, 350, 250, 150, 125
C	150	3	450, 350, 250, 150

Table 3.2: *Channel parameters for optimization study.*

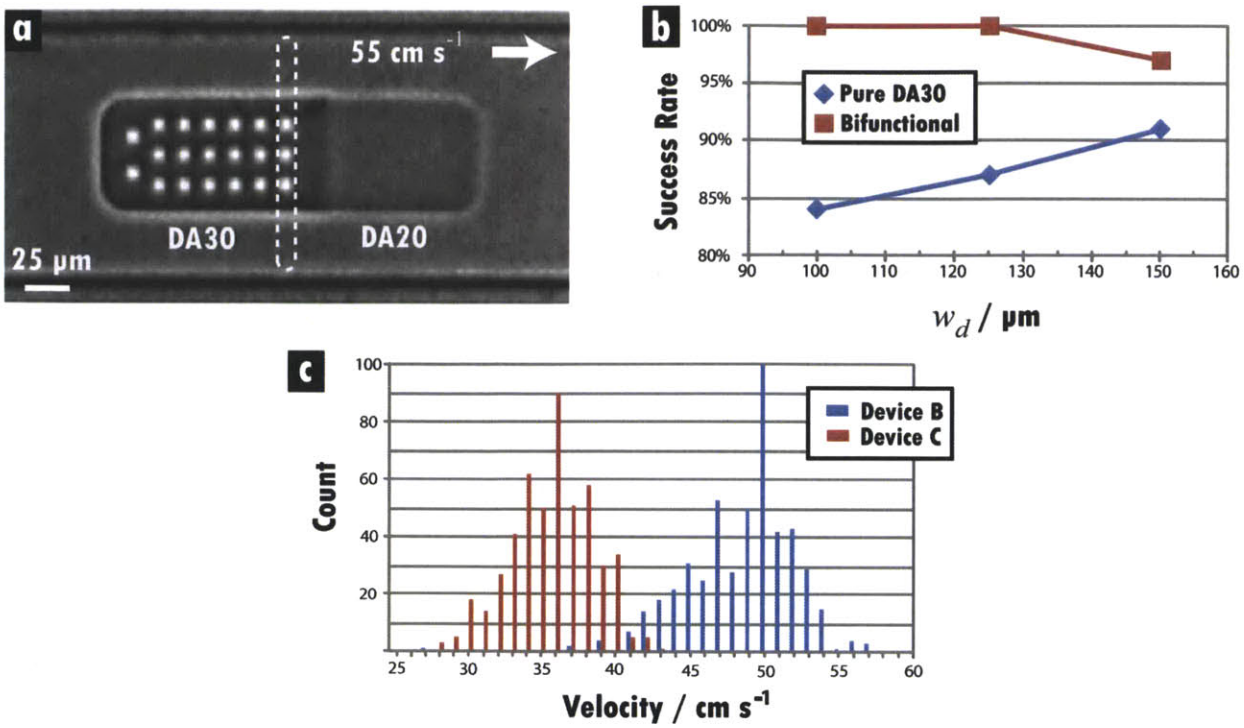

Figure 3.5: *Bifunctional barcoded particles. (A) Image from high-speed movie of bifunctional barcoded particle flowing "probe-first" at 55 cm/s from left to right in a channel with w_d = 125 µm. The dotted box around the first column of holes is drawn to indicate the thin excitation beam that will be employed in 1-D line scans. Column and row spacings are 7 and 9 µm, respectively. (B) Plot showing superior performance of bifunctional design. Each point represents 100 particles. (C) Histogram of detection-zone velocities of 1,000 bifunctional particles in devices B and C. The small spread of velocities for each device indicates a high degree of order and repeatibility. Results are compared from trials run in five B and five C devices with five different particle batches. The tails on the left side of each spike can be attributed to the small percentage (15–20%) of particles that flowed "code-first." For the bifunctional design, these particles were typically 10% slower than their probe-first counterparts.*

3.4.1 Bifunctional Design

To evaluate this new design, bifunctional particles were flowed through the three channel types at loading concentrations of 10 particles/µL, and their performance was compared to that of particles with probe and code regions both synthesized from DA30. Higher success rates were recorded for the bifunctional particles in all three channels (Figure 3.5 B). Bifunctional particles also flowed more closely along the centerline than their pure-DA30 counterparts in all channel types, with the best positioning achieved in design C. With the asymmetric morphology, a preference for "probe-first" flow was observed, with 91% of bifunctional and 79% of pure-DA30 particles doing so. In addition, higher velocities (35–60 cm/s) were recorded for these slender particles. Compared to the previously used 90-µm wide design, the 65-µm wide design provided larger side gaps that effectively reduced the

pressure drop across the particle, thereby diminishing the tendency to deform in the detection region. For the 600 total hydrogels analyzed, probe-first particles traveled ~10% faster than code-first particles, with a larger difference being measured for the pure-DA30 design.

3.4.2 Hole Spacing

The effect of hole spacing was investigated, again using the same three channel designs. Seeking to increase throughput, the loading concentration was increased from 10 to 15 particles/μL for these trials. Bifunctional particles with column spacings of 9, 7, and 5 μm were studied (all row spacings remained 9 μm). Shorter column spacings reduce the particle area needed for coding and thus increase the area available for probe immobilization. However, the desire to minimize the code area must be balanced by the need to maintain structural integrity. Nine trials with bifunctional particles of the three spacings in the three channels revealed a noticeable reduction in success rate for holes with 5-μm spacing. For the 900 hydrogels studied, the average success rates of the 9-, 7-, and 5-μm spacings were 97%, 99%, and 88%, respectively. Most failures of the smallest spacing were due to large compressions of holes in particles traveling code-first. Mean throughput at the higher loading concentration was 29 particles/s, while mean velocity was 51 cm/s.

3.4.3 Repeatibility

The high success rates achieved in devices B and C (100% and 99%, respectively) with 7-μm spacing were explored further by conducting additional trials. Five new batches of bifunctional particles with the spacing were synthesized, and five devices of each type were constructed. To investigate the reproducibility of the earlier results, each batch was sent through one of the five sets of devices (*i.e.*, batch 1 through B-1 and C-1, batch 2 through B-2 and C-2, *etc.*) at a loading concentration of 15 particles/μL. The results of these trials (Table 3.3) indicated a high degree of repeatibility, including inter-trial CVs less than 4% for the mean velocity, as well as mean success rates over 99%. This uniformity of particle speed (Figure 3.5 C) is crucial for high-fidelity signal analysis and signifies the establishment of well-ordered flows with minimal particle-particle interactions. As in earlier trials, particles preferentially adopted a probe-first orientation by the time they had entered the detection zone, with 76% flowing in this manner in B compared to 80% in C.

Loading Concentration (particles/μL)	Channel Type	Number of Trials	Mean Success Rate	Mean Throughput (s^{-1})	Mean Velocity (cm/s)	Inter-trial Velocity CV	Percentage Probe-first
15	B	5	99.8%	30.2	46.3	3.29%	84.4%
	C	5	99.2%	24.9	35.0	3.91%	84.6%
17.5	B	5	98.4%	40.2	48.1	2.02%	75.6%
	C	5	98.8%	35.4	35.4	1.44%	79.8%
20	B	1	92%	47.4	50.8	NA	86%
	C	1	91%	40.3	38.5	NA	71%

Table 3.3: *Optimized particle results for channels B and C at various loading concentrations. All results represent bifunctional particle design with AR = 3.62 and 7-μm column spacing. Each trial involved the measurement of 100 particles, and thus, the total number of particles represented in this table is 2,200.*

3.4.4 Loading Concentration

In order to maximize throughput, an attempt was made to determine the highest loading concentration that could still produce well-ordered, single-file flows. A reproducibility study similar to the one just described was conducted at a loading concentration of 17.5 particles/μL. Once again, a high degree of repeatibility was achieved (Table 3.3), with a minor success-rate decrease that was outweighed by a noticeable increase in mean throughput. As in the previous study, device B performed slightly better, with a higher mean throughput. Trials were then performed at 20 particles/μL. At this concentration, a more significant drop-off in the success rate occurred (Table 3.3), with crowding in the channel significantly disrupting the upstream focusing and even leading to the partial overlap of particles in the detection region. It was concluded that the increase in throughput at 20 particles/μL was not worth the decrease in success rate, and the maximum concentration was set at 17.5 particles/μL.

3.4.5 Tapered Channel Designs

Additional flow trials were conducted in two channel designs that did **not** use sheath streams (N = 0). These designs featured only a central channel (of the same length as the central channel in A, B, and C) that gradually tapered to a final width of either 100 μm (D) or 150 μm (E). The final width persisted for 2.6 mm in D and 3.4 mm in E. Bifunctional particles with 7-μm column spacing were used for these trials. At throughputs of only ~20 particles/s, success rates were lower (83% for D, 97% for E) than those in channels with side streams and abrupt contractions. A throughput of ~40 particles/s in E led to a 92% rate of success. Analysis of the upstream behavior in these simple tapered channels revealed a disordered flow of tumbling particles, as well as particles that slowly traveled along the walls of the channel (a behavior that was seen earlier in single-focus devices). While many of these particles were able to eventually adopt a proper orientation further downstream, the chaotic upstream tendencies led to a flow pattern and velocity distribution in the detection zone that exhibited more variability than those of designs with sheath flow. Indeed, for comparable throughputs, the standard deviation of particle velocity in D was

40% greater than in A and the deviation in E was 47% greater than in C. In many instances, consecutive particles in the detection zone in D and E were touching one another, with some even wedging a small portion of their probe region under the code region traveling ahead of it. These observations indicate poor conditioning of the particles in the upstream region and underscore the importance of side streams for the reliable establishment of well-ordered, single-file particle flows.

3.5 Barcoded Particle Flow Analysis

The hydrodynamic forces acting on the barcoded particles in the detection region of device B were explored by applying Equations 3.1–3.5 to the nearly unidirectional side-gap flow to determine the torque involved in lengthwise alignment. As expected, the torque about a central point on the particle's trailing edge increased as the deviation from lengthwise orientation grew (Figure 3.6 A). This torque always acted to restore the lengthwise orientation, and its magnitude was greater for particles with higher values of b (particle length-to-channel width ratio). This trend reinforces earlier observations regarding alignment tendencies and particle dimensions. For the case b = 1.88, results of the lubrication approximation agree well with the torques calculated for various values of θ using 2-D COMSOL simulations (Figure 3.6 B).

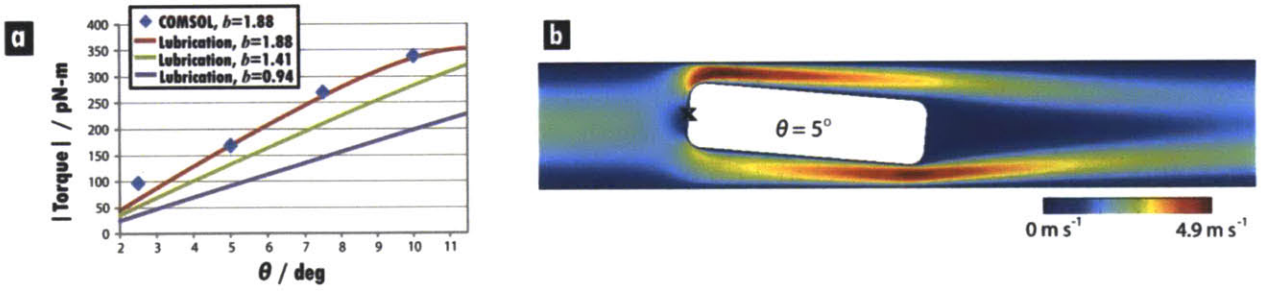

Figure 3.6: *Hydrodynamic forces on misaligned particles. (A) Plot of torque magnitude calculated for misaligned particle centered in detection zone with w_d = 125 μm. Torque is calculated about the central point on the trailing edge of the particle (marked by black x in (B)), based on experimental observations of particle rotation. As expected, higher deflection angles and higher values of b lead to larger torques that restore the particle to a lengthwise orientation. Lubrication analysis shows excellent agreement with torques calculated using 2-D COMSOL simulations of flow profiles (B) for the commonly investigated situation of b = 1.88 (i.e., particle length of 235 μm and channel width of 125 μm). Calculations are based on a 1.5 psi drop across a 700-μm long detection zone containing a single particle. Re of the flow upstream of the particle is ≈ 15.*

COMSOL Multiphysics' Incompressible Navier Stokes module was used to model the two-dimensional fluid flow in the microfluidic devices for particle focusing. For all simulations, a stationary nonlinear solver was used with the Direct (UMFPACK) linear system solver. Relative tolerance for the solver was at least 1.0 x 10^{-4} for all converged flow profiles, and

high mesh densities were used to increase resolution in areas of particular interest. Based on a "full-device" simulation without particles present, it was determined that devices with w_d = 125 μm and N = 4 had a mean fluid velocity of 6.79 m/s at the point of particle measurement in the detection region. This full-device simulation specified no-slip boundary conditions at all walls of the channel except the inlet port (normal pressure condition set at 9 psi) and the outlet port (neutral condition set). With a channel Reynolds number defined as $\mathrm{Re}_c = UD_h/\upsilon$ (U is mean flow velocity, D_h is hydraulic diameter of channel, υ is kinematic viscosity of fluid), these simulations demonstrate that $\mathrm{Re}_c \approx 40$ for typical detection-zone geometries. The same module was also utilized for the study of hydrodynamic forces on particles in the detection region of the channel (Figure 3.6). Using pressure estimates from the full-device simulation, flow profiles were solved for a 1.5 psi drop across a 700-μm long detection zone with w_d = 125 μm that contained a single particle with various values of θ. No-slip boundary conditions were set at the two side walls, a normal pressure condition was set at the inlet, and a neutral condition was set at the outlet. In addition, a normal flow velocity condition was set at the boundary of the particle to match the typical velocity of the particles in the detection region (50 cm/s). To determine the forces acting on the particle surface, the post-processing feature of COMSOL was used to export data on drag and lift forces at each point of the line segments used to construct the particle. This data was then combined with Equation 3.5 to numerically calculate the torque with a MATLAB script.

To further understand the flow in B, the orientation of particles was recorded by measuring the *acute* angle between the major axis of the particle and the centerline of the channel (θ) as particles moved through the upstream contraction points (Figure 3.7 A). An indication of alignment tendency can be obtained by measuring the standard deviation in this angle at the end of each constant-width region for a collection of 85 particles (Figure 3.7 B). The results indicate a nearly linear decrease in deviation as the channel width decreases for both of the orientations. The larger deviations in θ for code-first particles suggest this orientation is not driven to alignment in the flow as strongly as probe-first particles. Indeed, of the 85 particles studied, four switched from code-first to probe-first during flow, while none made the transition from probe-first to code-first. A closer examination of one particle of each orientation reinforces this hypothesis. For each frame of video, the *full* angle (*i.e.*, 0°–360°) between the long axis and the centerline (φ) was measured to preserve orientation information, with code-first corresponding to φ = 0° and φ increasing in the counter-clockwise direction (Figure 3.7 C). Despite starting only 20° from a lengthwise orientation, the code-first particle nearly moves into a widthwise orientation before rotating back into a code-first alignment that oscillates quite dramatically as the channel width approaches 150 μm. Meanwhile, the probe-first particle behaves in a much more controlled and predictable manner, with a rapid transition from widthwise to lengthwise orientation before a relatively mild oscillation about φ = 180°.

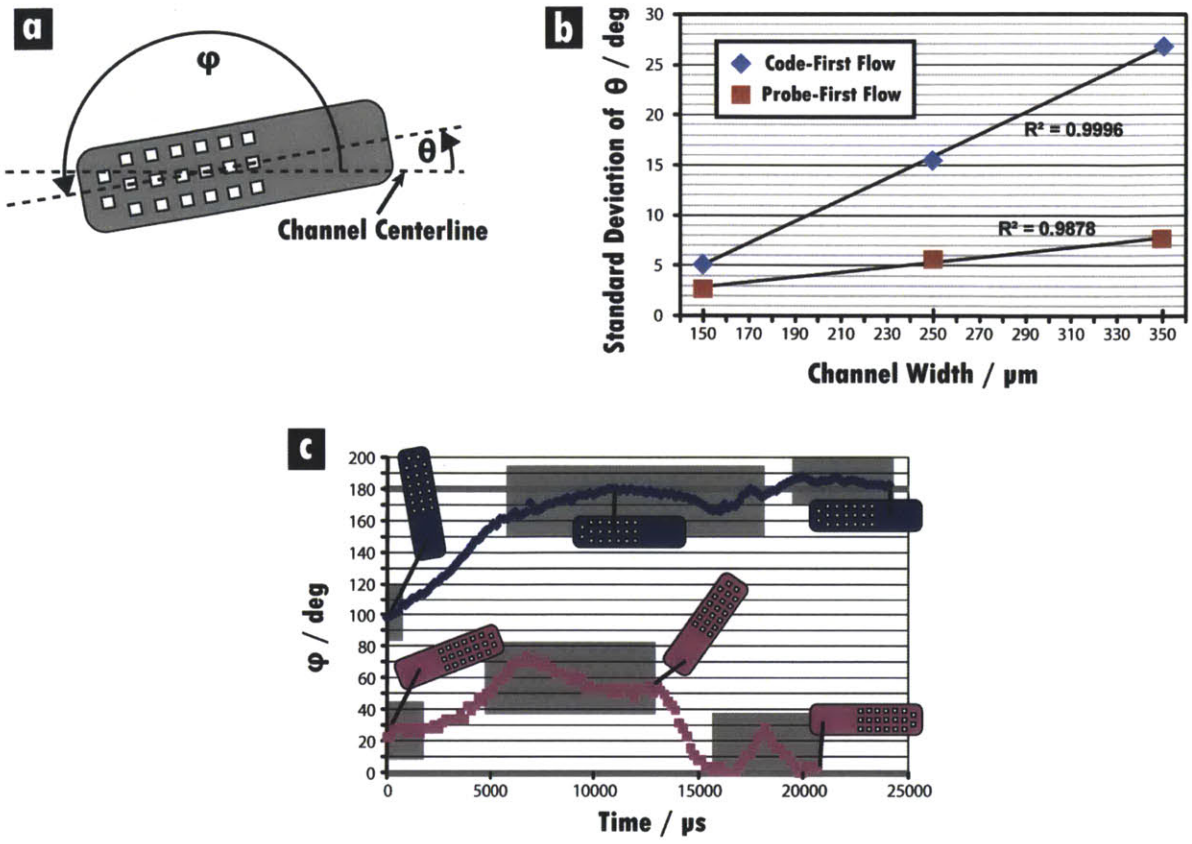

Figure 3.7: *Upstream rotation analysis in device B. (A) Schematic depicting the two angles of interest. (B) Plot of deviation of θ with channel width in the upstream region for particles that flow code- or probe-first. The larger deviation exhibited by the code-first particles suggests that such an orientation is less stable than the probe-first orientation. Measurements were taken at the end of the corresponding constant-width region prior to contraction. (C) Plot of φ over the course of the travels of two particles through the upstream region. The probe-first orientation is seen to be achieved in a smoother and more predictable fashion than the code-first orientation, again suggesting that the probe-first orientation is more stable. While the probe-first particle experiences limited disruptions in the regions of constant width (shaded boxes), the code-first particle experiences two sharp alterations in alignment. From left to right, the constant-width regions measure 350, 250, and 150 μm, respectively.*

These analyses provide insight into the preferential orientation that was observed in every trial with the half-probe/half-code particles, including those in which both regions were polymerized from DA30. Of the 3,200 bifunctional particles analyzed in A, B, and C devices, 83% flowed probe-first, compared to 79% of the 300 pure-DA30 particles. This indicates that the flexibility difference in the bifunctional design plays, at most, a minor role in the preference. The measurements of rotational tendency in the upstream region imply that the resistance to fluid flow in the thin height gaps (each ~1–2 μm) above and below the code region is different from the resistance in the height gaps above and below the probe. This disparity can be observed directly by comparing the lateral wobbles of a code-first particle

to the smooth, settled flow of a probe-first particle in the upstream regions of a channel (Figure 3.7 C). While it is tempting to attribute this resistance difference to the relative stiffness of the code region, the data from the pure-DA30 trials refute this claim. The holes that constitute the graphical code are the only other source of asymmetry in the particle and thus appear to give rise to the resistance difference. It seems that the flow pattern and the resulting pressure gradient along the length of the particle in the height gap depend on whether the holes are on the leading or the trailing edge of the particle. This hypothesis is supported by the observed velocity disparity between code- and probe-first particles noted earlier for bifunctional particles as well as pure-DA30 particles.

3.6 Derivation of Lubrication Approximation

To better understand the hydrodynamic forces acting on the particles, a lubrication approximation was developed to describe the bypass fluid flow in the side gaps in the narrow detection portions of the channel. In this section, a full derivation of the equations from Section 3.2 is provided for completeness. Based on the negligible deformation of particles in the optimized design, the particles are assumed to be rigid bodies for this analysis. Building off previous observations of deformable red blood cells in rectangular channels, the bypass flowrate in the larger side gaps is assumed to be much greater than the flowrate through the small height gaps, leading to the neglect of any three-dimensional flow effects in the side gaps (*i.e.*, flow only in the *xy*-plane) [183, 184]. The side gap is essentially a long, narrow channel, and as a result, the flow within it can be regarded as nearly unidirectional (*x*-direction) and dominated by viscous stresses. For the lubrication approximation to be valid in this situation, both geometric and dynamic requirements must be met [159]. Using the physical setup depicted in the schematic in Figure 3.1 C and assuming a constant volumetric flowrate in the detection region of the channel, the geometric requirement becomes:

$$\frac{|h_0 - h_1|}{L\cos\alpha} = \frac{L\sin\alpha}{L\cos\alpha} = \tan\alpha << 1 \qquad \text{Equation 3.6}$$

and the dynamic requirement becomes:

$$\left(\frac{u(x)h(x)}{\upsilon}\right)\left(\frac{|h_0 - h_1|}{L\cos\alpha}\right) = \frac{q}{\upsilon}\tan\alpha << 1 \qquad \text{Equation 3.7}$$

where $u(x)$ is the mean velocity at a given x position in the channel, υ is the kinematic viscosity of the fluid, and q is equivalent to $u(x)h(x)$. Upon entrance into the detection region of the optimized channel, the observed angle of deflection, α, for a typical particle is between 0° and 5°, thereby giving a maximum value of 0.087 for tan α and satisfying the

geometric requirement. Meanwhile, based on a typical volumetric flowrate per width, q, of 2 x 10^{-5} m^2/s and a kinematic viscosity, υ, of 1 x 10^{-5} m^2/s for the PTET carrier fluid, the q/υ prefactor in Equation 3.7 has a value of 2 and thus the **maximum** value of the central expression in Equation 3.7 is 0.174. These values suggest that the use of the lubrication approximation is indeed valid within this side gap region.

A reference frame moving with a particle with a center of mass located at the center of the channel was adopted to simplify calculations (Figure 3.1 C). Considering only the lower half of the channel and assuming the particle has a constant velocity, U, in the $+x$-direction, the no-slip boundary conditions are

$$v_x(x,0) = -U_w \qquad \text{Equation 3.8}$$

$$v_x(x,h(x)) = 0 \qquad \text{Equation 3.9}$$

where

$$h(x) = h_0 + \left(\frac{h_1 - h_0}{L\cos\alpha}\right)x. \qquad \text{Equation 3.10}$$

The lubrication approximation reduces the Navier-Stokes equation to

$$\frac{\partial^2 v_x}{\partial y^2} = \frac{1}{\mu}\frac{dP}{dx} \qquad \text{Equation 3.11}$$

where P is solely a function of x. As discussed elsewhere, the distinction between dynamic pressure, P, and the regular pressure, p, is quantitatively insignificant within thin layers of fluid that have large pressure variations [159]. Integrating twice with the boundary conditions gives Equation 3.1.

When this expression is used to evaluate the mean velocity in the channel, it is found that

$$u(x) = -\frac{dP}{dx}\frac{h(x)^2}{12\mu} - \frac{U_w}{2}. \qquad \text{Equation 3.12}$$

Upon rearrangement, this provides Equation 3.2. When this expression for dP/dx is used in the expression for the velocity in the x-direction, the following result is obtained:

$$v_x(x,y) = -\frac{y}{h(x)^2}\left(\frac{6qy}{h(x)} + 3U_w y - 6q - 3U_w h(x)\right) + U_w\left(\frac{y}{h(x)} - 1\right). \qquad \text{Equation 3.13}$$

In order to determine the force (per unit width) which the fluid exerts on the surface of the particle, it is necessary to calculate the stress vector, **s**:

$$\mathbf{s} = \mathbf{n}\cdot\boldsymbol{\sigma} \qquad \text{Equation 3.14}$$

$$\mathbf{n}(x) = \frac{1}{g}\left(\frac{dh}{dx}\mathbf{e}_x - \mathbf{e}_y\right) \qquad \text{Equation 3.15}$$

$$g(x) = \left[\left(\frac{dh}{dx}\right)^2 + 1\right]^{1/2} \qquad \text{Equation 3.16}$$

where **n** is a vector normal to the particle surface, $\boldsymbol{\sigma}$ is the stress tensor, $g(x)$ is a normalization factor, and $\mathbf{e}_x$ and $\mathbf{e}_y$ are the unit normal vectors in the x- and y-directions, respectively. The nonzero components of the stress vector are then given by

$$s_x = \frac{1}{g}\left(\frac{dh}{dx}\sigma_{xx} - \sigma_{yx}\right) = \frac{1}{g}\left[\tau_{xx}\frac{dh}{dx} - P\frac{dh}{dx} - \tau_{yx}\right] \qquad \text{Equation 3.17}$$

$$s_y = \frac{1}{g}\left(\frac{dh}{dx}\sigma_{xy} - \sigma_{yy}\right) = \frac{1}{g}\left[\frac{dh}{dx}\tau_{xy} + P - \tau_{yy}\right] \qquad \text{Equation 3.18}$$

where $\boldsymbol{\tau}$ is the viscous stress tensor. Because the particle is assumed to be a rigid body, both of the normal viscous stresses are zero. Moreover, in the nearly unidirectional flow in the gap, the normalization factor, g, can be approximated as unity, and the $\partial v_x/\partial y$ term will be much larger than the $\partial v_y/\partial x$ term in the calculation of the remaining viscous stress component ($\tau_{xy} = \tau_{yx}$). With this approach, Equation 3.3 is recovered, and further it is found that

$$s_y = \mu\frac{dh}{dx}\frac{\partial v_x}{\partial y} + P. \qquad \text{Equation 3.19}$$

In calculating the y component of the stress vector, it is permissible to neglect the shear stress term. The ratio of the pressure to the shear stress is $\sim L\cos\alpha/|h_1 - h_0| = \cot\alpha$, and since α is not usually more than 5° in the detection region, it is estimated that the pressure

contribution will always be at least ten times greater than the shear stress contribution. This reasoning allows us to reduce to Equation 3.4.

For calculation of the drag and lift forces (per unit width) involved in orientation and alignment, these stresses can then be integrated along the surface of the particle using the following equations:

$$F_x = -\int_{x_1}^{x_2}\left(\frac{dh}{dx}P + \mu\frac{\partial v_x}{\partial y}\Big|_{y=h(x)}\right)dx \qquad \text{Equation 3.20}$$

$$F_y = \int_{x_1}^{x_2} P\,dx. \qquad \text{Equation 3.21}$$

For the curves plotted in Figure 3.6 A, the stress expressions derived above were used to calculate the torque that the gap flow exerted on particles in the detection region. The pressure field was calculated by integrating Equation 3.2 and using boundary values that matched the bulk flow ahead of and behind the particle [159]. Torque (per unit width), **G**, was calculated about the central point on the trailing edge of the particle, $\mathbf{r_0}$ (Figure 3.6 B), using numerical integration in MATLAB and Equation 3.5. The torque was calculated about this point because high-speed videos of poorly aligned particles in the upstream portion of the detection region were observed to most often rotate about this point in their movement into a properly-aligned orientation. For all calculations with this lubrication approximation, the effect of the upper gap was modeled in an analogous fashion to that just described for the lower gap and the contributions summed for the determination of the total force and torque. The primary difference between the two situations is that the lower gap involved a contraction while the upper gap involved a symmetric expansion.

3.7 Summary of Results

We have shown that a plurality of sufficiently spaced side-focusing streams, a detection zone of ample width, and a moderate particle loading concentration are crucial for the high-throughput flow alignment of graphically encoded hydrogel microparticles. In addition, the reliable alignment of soft particles in high-speed flows (without deformation or clogging) is greatly enhanced by simultaneously optimizing the mechanical properties and morphology of the particles to ensure efficient focusing by hydrodynamic forces while still maintaining overall structural integrity in areas of high shear. The high throughputs achieved in the optimized design of our microfluidic system (40 particles/s) compare favorably with those of currently available technologies for analyzing hard-sphere suspension arrays. The use of multiple probe strips on each particle in our setup has the potential to greatly augment this processing capacity in future work.

The next step in the development of this platform is the implementation of a PMT for the detection of the fluorescence emitted by the passing particles. The single-color detection scheme made possible by the graphical encoding of probe identity should make the platform easier and less expensive to operate than existing suspension array cytometers. Furthermore, the large code library of the method described here permits the pooling of samples prior to scanning, a step which can greatly reduce processing times for assays.

Chapter 4

Rapid MicroRNA Profiling on Encoded Hydrogel Microparticles

The work presented in this chapter establishes the encoded gel particle system as an efficient miRNA profiling platform through the introduction of a ligation-based fluorescent labeling scheme and a microfluidic scanning instrument that can decode particles and quantify the amount of target bound to probe regions at rates up to 25 particles/s. This platform's unprecedented combination of sensitivity, flexibility, and throughput offers exciting possibilities for discovery and clinical applications, particularly in the rapid quantification of low-abundance miRNA and other biomolecules for cancer diagnostics.

4.1 Introduction

MicroRNAs are short non-coding RNAs that mediate protein translation and are known to be dysregulated in diseases including diabetes, Alzheimer's, and cancer [117, 125, 187]. With greater stability and predictive value than mRNA, this relatively small class of biomolecules has become increasingly important in determining disease diagnosis and prognosis. However, the sequence homology, wide range of abundance, and common secondary structures of miRNAs have complicated efforts to develop accurate, unbiased quantification techniques [134, 188]. Applications in the discovery and clinical fields require high-throughput processing, large coding libraries for multiplexed analysis, and the

flexibility to develop custom assays. Microarray approaches provide high sensitivity and multiplexing capacity, but their low-throughput, complexity, and fixed design make them less than ideal for use in a clinical setting [12, 138]. PCR-based strategies suffer from similar throughput issues, yet offer highly sensitive and specific detection for genome-wide miRNA expression profiling [139]. Alternative bead-based systems provide a high sample throughput, but with reduced sensitivity, dynamic range, and multiplexing capacities [35, 41, 59]. miRNA profiling by deep sequencing is emerging as a powerful tool for small RNA analysis; however, the high cost of implementation and need for large amounts of input RNA currently limit its utility [149]. The ideal system for miRNA quantification would offer the detection performance of array and PCR-based methods, the throughput of bead-based systems, and improved reproducibility with a user-friendly workflow.

The Doyle lab has previously reported the synthesis of chemically and geometrically complex hydrogel microparticles using flow lithography [52, 153, 166]. By polymerizing across laminar co-flowing streams of monomer, multifunctional particles with distinct chemical regions can be rapidly (>10^4/h) produced with high degrees of reproducibility. Separate "code" and "probe" regions are used to identify particles and capture targets, respectively [52]. The bulk-immobilization of probe molecules in the bio-inert, PEG-based gel scaffolds provides solution-like capture kinetics and high degrees of both specificity and sensitivity, leading to significant advantages over surface-based immobilization strategies employed in microarrays and existing particle systems [180]. Patterns of unpolymerized holes in the code portion of the particle serve as the basis for a graphical multiplexing barcode to identify the probe(s) in a particular particle.

Despite rapid developments in the synthesis of information-rich encoded micro- and nanoparticles, there has been little progress in the creation of high-throughput systems for analyzing these complex entities [44, 46]. The majority of emerging bead-based systems lack a method for rapid decoding and target quantification, while commercially available flow-through scanning systems constrain multiplexing capacity and provide only simple intensity measurements for inefficient, gate-based analysis [41, 44, 189, 190]. Unlike bead systems that optically encode spheres and use arrays of lasers and PMTs, our particles have multiple distinct regions, making single-color, morphology-based scanning possible, with only one excitation source and one detector required. This setup significantly reduces the cost and complexity of analysis. Furthermore, the coding library can easily be expanded to accommodate high levels of multiplexing or parallel processing of samples. The flexibility of our synthesis method also allows for embedding living entities such as cells in the probe region of particles, or for incorporating multiple probe regions on a single particle for intrabead multiplexing [52, 163].

4.2 Microfluidic Scanning System

Here, we describe the performance of a gel particle scanning system and an accompanying post-hybridization labeling scheme for use in high-throughput multiplexed miRNA

quantification (Figure 4.1 A). We constructed a slit-scan system that uses a thin laser illumination window to sequentially excite passing portions of precisely oriented particles, thus producing a temporal fluorescent signature from which code identity and bound target amount can be determined (Figure 4.1 B,C) [191, 192]. A polydimethylsiloxane (PDMS) focusing chamber bonded to a glass slide was mounted on a fluorescence microscope for analysis procedures. To align the soft gel particles, the sample and sheath streams were injected into the device with 8-psi forcing pressure, creating a single-file flow of particles traveling at velocities of ~0.5 m/s. Slit illumination was created with a 532-nm laser spatially filtered through a chrome-coated glass mask inserted into the field stop position of the microscope. As particles passed through the illumination window, fluorescent signatures were captured with a PMT and the resulting signals were processed using a homemade amplifier with a low-pass filter.

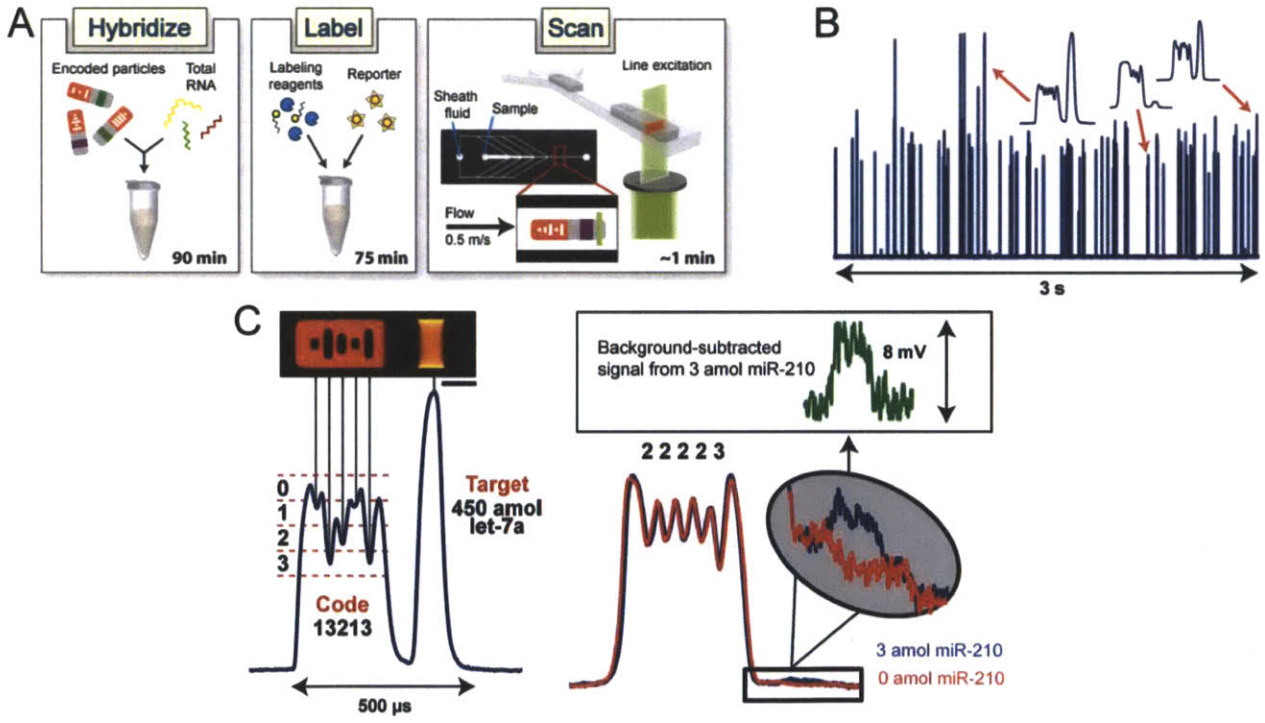

Figure 4.1: *Encoded gel particle assay system. (A) Workflow of platform includes (i) hybridization of particles with target, (ii) incubation of particles with universal labeling adapter, ligation enzyme, and fluorescent reporter, and (iii) scanning of particles to determine code identity and amount of target bound. A typical particle consists of a fluorescent barcoded region and a probe-laden region flanked by two inert sections. Central-most hole has a fixed value to indicate particle orientation. (B) Actual PMT fluorescence signatures of 75 flow-aligned particles. (C) Magnified signatures of individual particles. As probe-target reaction rate is observed to be faster than target diffusion through gel matrix, the increased fluorescent intensity on the sides of the particle in image can be attributed to binding of target near the side faces of probe region [180]. Scale bar is 50 µm.*

The fluorescent signal obtained along each particle is integrated across the particle width by the detector. The sizes of the holes in the code region determine the depths of the fluorescence troughs in the signature and thus indicate the particle identity. We optimized the particle architecture and hole design to find that four distinguishable coding levels (0–3) could be obtained for 70-µm wide particles, leading to 192 possible codes for a five-bar particle (Figure 4.1 C). Multiplexing capacity could easily be augmented to $>10^5$ by adding more bars, using multiple fluorescent levels for the code region, or incorporating multiple probes on each particle (Figure 4.2 and Figure 4.3). Furthermore, by scanning particles with various barcode designs, it was observed that a minimum spacing of 8 µm was required between holes to prevent mechanical deformations of the soft hydrogels during flow alignment. We developed and trained a decoding algorithm to accurately decode particles and quantify targets. Particle orientation and velocity are determined to analyze the coding holes and establish a first estimate of code identity. A revised assignment is calculated by checking the consistency among holes identified as the same level, and a decoding confidence score is then computed and used to accept or reject particles.

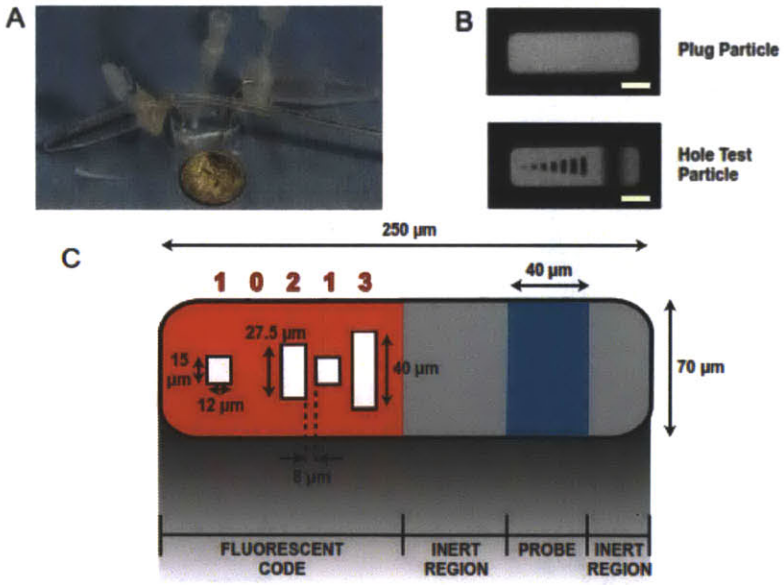

Figure 4.2: *High-throughput flow alignment device and code design. (A) Image of PDMS focusing chamber attached to glass slide, with inlets and outlet attached. Reservoir inlet on the left delivers sheath fluid, while central pipette tip delivers the particle-bearing fluid. Reservoir outlet on the right serves as a collection point for particles that have been scanned. The chamber is mounted on a standard inverted fluorescence microscope for scanning runs. (B) Images of particles used to optimize scanner performance. Simple plug particles were scanned to maximize signal-to-noise ratio (SNR) and frequency response of detection circuit. Particles with holes of various areas were used to determine the minimum differences in size required to distinguish between coding levels. Scale bars are 50 µm. (C) In the final particle design, coding holes were separated by 8 µm, and the lengths of the holes were 15, 27.5, and 40 µm for levels 1, 2, and 3, respectively. All holes had a width of 12 µm.*

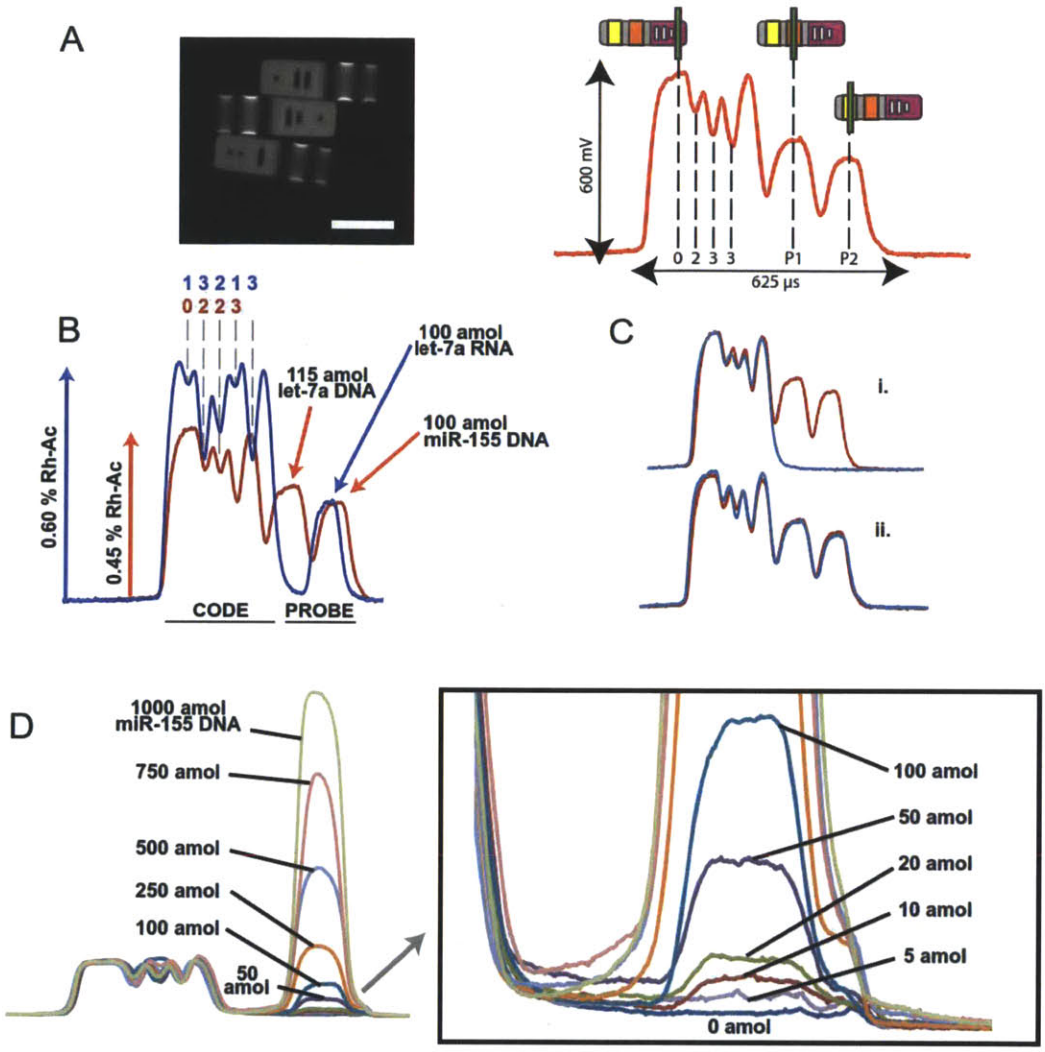

Figure 4.3: *Multi-probe particles. (A) Fluorescence image and accompanying scan of two-probe barcoded hydrogel particles of the same dimensions (250 × 70 × 35 µm) as used in the 12-plex study. The probe strip nearest the code region contains DNA capture sequence for let-7a, while the second strip contains capture sequence for miR-155. Particles have been incubated for 90 min with 115 and 100 amol of the DNA analogs of let-7a and miR-155, respectively. Labeling has been performed with the ligation scheme. Although the probe strips are ~50% smaller than those used in the 12-plex study, single-probe particles with this reduced strip size were successfully implemented in the sensing and scanning procedures. To demonstrate different encoding possibilities, these two-probe particles were synthesized with four coding bars and with 75% as much rhodamine acrylate (Rh-Ac) in the code region (0.45% (v/v) final concentration) as the 12-plex batches. Scale bar is 100 µm. Green bar in schematic indicates position of excitation slit relative to particle. (B) A single-probe particle from the 12-plex study incubated with 100 amol let-7a RNA is shown (blue curve) for comparison purposes. Red curve corresponds to scan in A. (C) Overlaid scans comparing (i) particle incubated as in A and particle incubated with 0 amol of both targets, and (ii) two particles incubated as in A and scanned during different assay sessions. (D) Scans of two-probe particles incubated with 0–1000 amol of miR-155 DNA analog target. As in the 12-plex study, five different codes are featured for the same probe set.*

4.3 Ligation-based Method for miRNA Labeling

To generate signal in the probe region of particles, we employed a unique ligation-based scheme to fluorescently label bound miRNA targets. Existing approaches rely on the bulk-labeling of RNA using chemical or enzymatic means [138, 193, 194]. These methods suffer from high cost, sequence bias due to secondary structure [138], complicated protocols [138], and in the case of microarrays, the need for small-RNA purification and clean-up [193, 194]. To overcome these issues, we implemented a two-step method to efficiently label targets after hybridization in about one hour. We used T4 DNA ligase to link a universal oligonucleotide adapter to the 3' end of targets captured on gel-embedded DNA probes (Figure 4.4). For maximum fluorescent efficiency, we used a biotinylated adapter with phycoerythrin-conjugated streptavidin reporter (SA-PE), though it is also possible to use fluorophore-conjugated adapters directly.

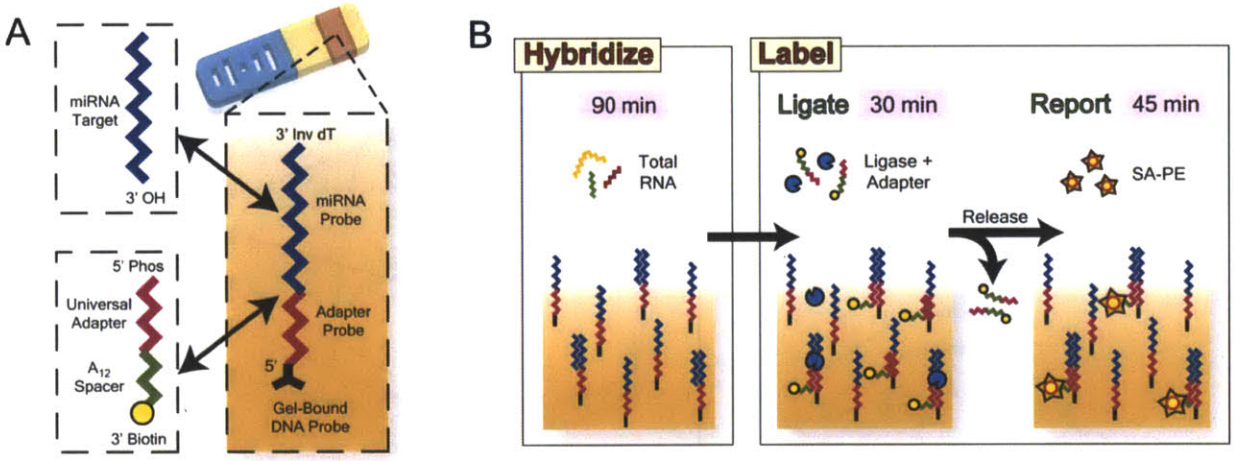

Figure 4.4: *Post-hybridization miRNA labeling via ligation to a universal adapter. (A) DNA probes, linked at their 5' end throughout the probe region of encoded hydrogel particles, contain a miRNA-specific sequence adjacent to a universal adapter sequence such that the 3' end of a captured target would abut the 5' end of a captured adapter oligonucleotide. The probe is capped with an inverted dT to mitigate incidental ligation and the adapter has a poly(A) spacer to extend its biotinylated 3' end away from the hydrogel backbone for efficient reporting. (B) After particles are hybridized with total RNA, T4 DNA ligase is used to link the universal adapters to the 3' end of captured targets, unligated adapters are released using a low-salt rinse, and SA-PE is used as a fluorescent reporter.*

It was necessary to optimize several aspects of the labeling scheme, including probe/adapter design, reagent concentrations, rinse buffer salt content, ligation time, and ligation temperature. We show here the effects of ligation time and adapter tail length on labeling efficiency. The nucleic acid probes, targets, and adapters (all from IDT) are given in Table 4.1:

Oligo Name	Sequence/Modifications	
let-7a probe, DNA	/5Acryd/GATATATTTTAAACTATACAACCTACTACCTCA/3InvdT/	
let-7a target, RNA	5'-UGAGGUAGUAGGUUGUAUAGUU-3'	
UA10-Cy3, DNA	/5Phos/TAAAATATAT/3Cy3/	
UA10-bio, DNA	/5Phos/TAAAATATAT/3Bio/	poly(A) = 0
	/5Phos/TAAAATATATAAA/3Bio/	poly(A) = 3
	/5Phos/TAAAATATATAAAAAA/3Bio/	poly(A) = 6
	/5Phos/TAAAATATATAAAAAAAAAAAA/3Bio/	poly(A) = 12

Table 4.1: *Nucleic acid probes and targets used in labeling optimization studies.* ***Blue*** *represents universal adapter-specific sequences,* ***maroon*** *represents target-specific sequences, and* ***green*** *represents poly(A) tails.*

Probes were designed to include a miRNA-specific region and an adapter-specific region, such that when bound, the 3' end of the miRNA target would abut the 5' end of the adapter. We chose to label the 3' end of miRNA targets because it has been demonstrated that when using a DNA template, the action of T4 DNA ligase in joining DNA to RNA molecules proceeds several orders of magnitude more rapidly at the 3' end of RNA versus the 5' end [195]. The adapter sequence and length were chosen such that (1) the melting temperature was between 10–20°C in ligation buffer, (2) the sequence was not self-complementary in order to avoid adapter hairpin or homodimer formation, and (3) complete DNA probes (with adapter and miRNA sequences) did not show appreciable hairpins for the miRNAs investigated.

We performed studies to determine the minimum ligation time needed for our labeling assay, using let-7a as a model system. Particles bearing a let-7a DNA probe region were incubated with 5 fmol synthetic let-7a RNA at 55°C for 110 min. Particles were rinsed three times with PBST and incubated with 250 μL of a ligation mix containing 200 U T4 DNA ligase, 40 nM Cy3-modified adapter (UA10-Cy3), and 0.05% Tween-20 in T4 DNA ligation buffer (NEB) for 10, 30, or 90 min at 16°C. After ligation, particles were rinsed three times in 1× TE containing 0.025 M NaCl, deposited on a glass slide, and imaged using a CMOS camera (Imaging Source). We measured the fluorescence intensity in the probe region of each particle, subtracting the background fluorescence to get a target signal, which indicated ligation efficiency. The results are shown in Figure 4.5. We calculated the relative efficiency by normalizing each signal by that obtained for the 90 min sample. As can be seen in Figure 4.5, ligation is >95% complete even after a short 10-min reaction. For the experiments described in this work, we chose to use a ligation time of 30 min to ensure nearly complete ligation.

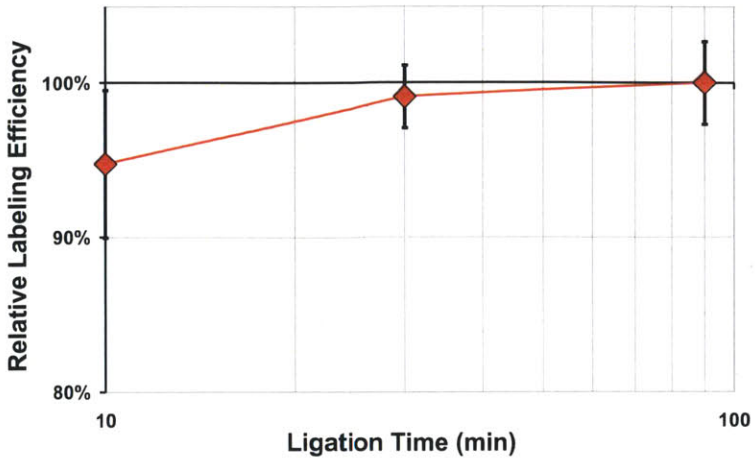

Figure 4.5: *Relative ligation efficiency over time. Error bars represent the standard deviation taken over measurements from five particles.*

The SA-PE reporter is a large protein structure that has a radius of gyration on the order of ~10–15 nm. As such, when using biotinylated adapters with the SA-PE reporter, we found that it was beneficial to extend the biotin group away from the polymer backbone of the gel matrix. To do this, we used a poly(A) tail at the 3' end of the adapter and investigated the effect of tail length on target signal. In this experiment, we used the same let-7a particles as in the previous section, incubating with 50 amol let-7a miRNA for 60 min at 50°C. The particles were rinsed three times in PBST, and divided into four separate tubes. Particles in each tube were incubated for 30 min at room temperature with ligation mix containing 200 U T4 DNA ligase, and 40 nM UA10-bio (with either a 0, 3, 6, or 12 bp poly(A) tail), in 1× T4 DNA ligation buffer (NEB) with 0.05% Tween-20. After ligation, particles were rinsed three times in 1× TE containing 0.05 M NaCl and 0.05% Tween-20. Particles were deposited on a glass slide and imaged. The target signals were compared to determine the effect of poly(A) tail length. As can be seen in Figure 4.6, the length of the poly(A) tail has a large effect on target signal obtained. From zero to 12 bp, the signal increases ~5× but seems to level off at that point. For the experiments described in this work, we chose to use universal adapters with poly(A) tail lengths of 12 bp.

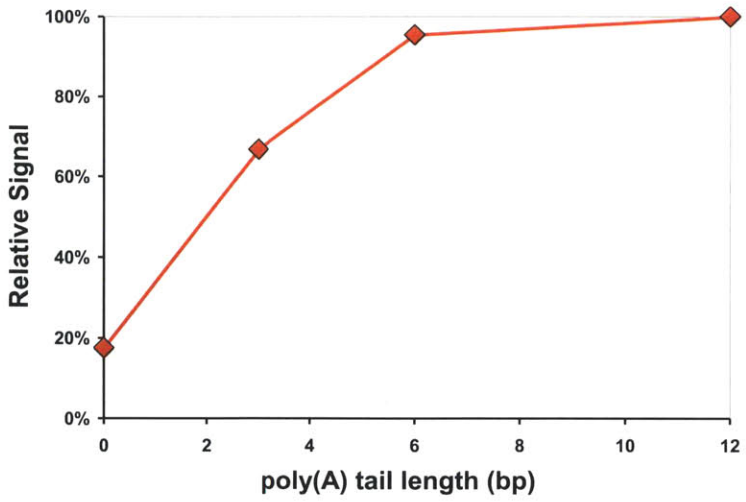

Figure 4.6: *Effect of universal adapter poly(A) tail length on fluorescence signal when using biotinylated adapters with a streptavidin-phycoerythrin reporter. Signals are relative to that measured for a tail length of 12 bp.*

Importantly, this labeling method was highly efficient, had no minimal input RNA requirement, and showed no sequence bias for the targets used in this study. For each new miRNA target species, we simply incorporated a target-specific sequence into the universal probe template; complex modification and customization were not necessary.

4.4 System Characterization

We investigated the dynamic range, sensitivity, and specificity of the platform in the context of a 12-plex assay featuring ten clinically relevant miRNA targets. Because of its relative invariance across tissue types and disease states, RNU6B was used as an internal control for normalization purposes. We also used 100 amol of miSpike (a synthetic 21-mer) as an external control to validate the consistency of the labeling and scanning processes. We synthesized twelve batches of single-probe particles for this study. To compensate for discrepancies in target hybridization rates, we implemented a coarse rate-matching by tuning the probe concentration for each target using previously determined scaling laws [180]. In an effort to coarsely rate-match the binding of the targets used in the study, we incorporated the probe sequences at different concentrations in the particles (Table 4.2). As the characteristic time for target depletion scales with the inverse square root of probe concentration, a doubling of the binding rate for a given target will require a 4× increase in the amount of probe incorporated in a probe region of fixed size. In this study all rates were adjusted to match that of let-7a binding. It should be noted that higher sensitivities and shorter assays could have been achieved by loading probe at maximum concentration, but the goal of this study was to develop a 12-plex assay with broad dynamic range and ~1 amol

sensitivity for *all* targets. To fully demonstrate the versatility of the scanner, five separate codes were correlated to particles of each probe type, thereby simulating a 60-plex assay (Table 4.2).

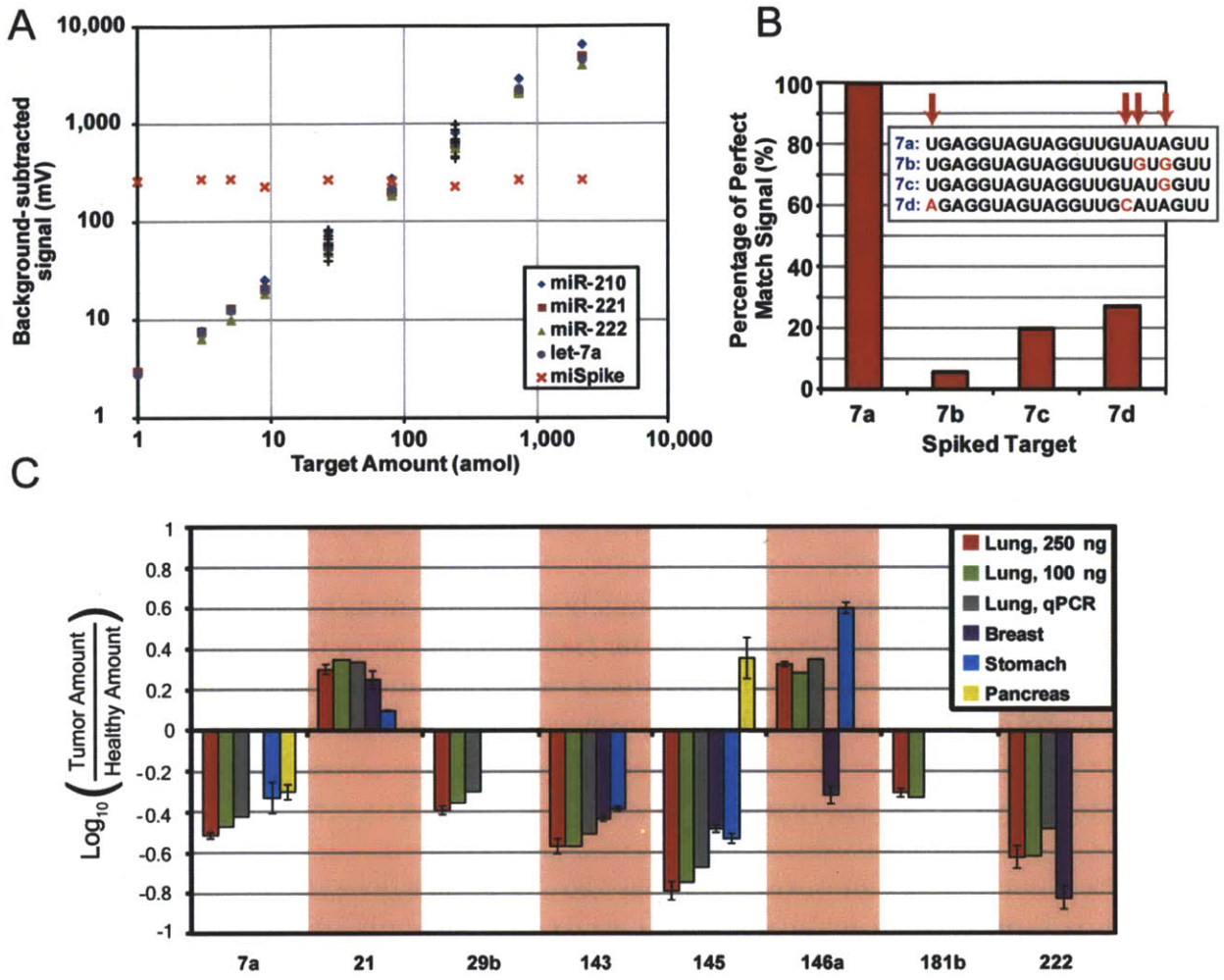

Figure 4.7: *System performance in 12-plex assay. (A) Calibration curves for particle batches, with background-subtracted signal plotted against spiked target amount. miR-210, -221, -222 and let-7a were spiked into the same incubation mixes at the indicated amounts. The remaining seven naturally-occurring targets ('+' symbols) were spiked into the 27- and 243-amol trials to validate performance. For all trials, 200 ng of E. coli total RNA was also spiked in for complexity. Mean CV of target level is 6.35% when considering target levels greater than 5 amol. Each point represents, on average, 19 particles from a single run. (B) Specificity of let-7a probe in the presence of sequences closely related to intended target. (C) Cancer profiling results for dysregulated targets in four human tissue types. Error bars represent standard deviation in triplicate measurements on aliquots of the same single-patient sample. Amount of total RNA used in gel-particle assays is 250 ng, unless otherwise noted. See supporting information for details of dysregulation analysis.*

Target	Probe Sequence	Hairpin Melting Temps (°C)	Binding Rate Relative to let-7a (Probe at 50 µM)	Adjusted Probe Conc. (µM)	Identifying Codes for Mock 60-plex
let-7a	5Acryd/GAT ATA TTT TAA ACT ATA CAA CCT ACT ACC TCA/3InvdT	38.0	1.00	50	31131, 32231, 31231, 32131,
miR-21	5Acryd/GAT ATA TTT TAT CAA CAT CAG TCT GAT AAG CTA/3InvdT	60.4, 52.9, 49.3, 46.6	0.45	247	31112, 32212, 31212, 32112,
miR-29b	5Acryd/GAT ATA TTT TAA ACA CTG ATT TCA AAT GGT GCT A/3InvdT	45.9, 44.7, 41.7	0.63	126	31132, 32232, 31232, 32132,
miR-181b	5Acryd/GAT ATA TTT TAA CCC ACC GAC AGC AAT GAA TGT T/3InvdT	58.4, 43.2, 38.6	0.89	63	32230, 31130, 31230, 32130,
miR-143	5Acryd/GAT ATA TTT TAG AGC TAC AGT GCT TCA TCT CA/3InvdT	55.2, 51.1	1.04	50	31110, 32210, 31210, 32110,
miR-145	5Acryd/GAT ATA TTT TAA GGG ATT CCT GGG AAA ACT GGA C/3InvdT	47.4, 43.0, 36.6	1.01	50	31121, 32221, 31221, 32121,
miR-146a	5Acryd/GAT ATA TTT TAA ACC CAT GGA ATT CAG TTC TCA/3InvdT	64.6, 49.4, 48.3, 43.4	0.67	111	30001, 31101, 32201, 31201,
miR-210	5Acryd/GAT ATA TTT TAT CAG CCG CTG TCA CAC GCA CAG/3InvdT	68.4, 65.6, 59.7, 55.4	0.90	62	31122, 32222, 31222, 32122,
miR-221	5Acryd/GAT ATA TTT TAG AAA CCC AGC AGA CAA TGT AGC T/3InvdT	49.8, 43.6, 42.2, 41.0	0.82	62	31111, 32211, 31211, 32111,
miR-222	5Acryd/GAT ATA TTT TAA CCC AGT AGC CAG ATG TAG CT/3InvdT	68.2, 68.1, 58.1, 47.5	0.62	130	31120, 32220, 31220, 32120,
miSpike	5Acryd/GAT ATA TTT TAA GAC CGC TCC GCC ATC CTG AG/3InvdT	66.5, 46.0	1.21	35	30002, 31102, 32202, 31202,
RNU6B	5Acryd/GAT ATA TTT TAA AAA ATA TGG AAC GCT TCA CGA ATT TGC GTG TCA TCC TTG CG/3InvdT	64.4, 58.4, 56.9, 56.1	0.95	55	30000, 31100, 32200, 31200, 32100

Table 4.2: *Particle codes and probe information for batches synthesized for 12-plex study. Final composition (v/v) of PEG-DA$_{700}$, PEG$_{200}$, and Darocur 1173 photoinitiator in prepolymer stream for probe were fixed at 18, 36, and 4.5%, respectively. Hairpin melting temperatures are listed in descending order, as calculated for the DNA-RNA duplex by IDT's OligoCalc application for the incubation conditions used in the study. For each miRNA, the relative binding rate was calculated using the average of target signals from 30- and 60-min incubations with 500 amol of target and ligation labeling. Short incubations were chosen to ensure the system had not reached equilibrium. Quoted probe concentrations refer to prepolymer stream composition. Approximately 11% of the probe in the prepolymer stream was covalently incorporated into the particles [180].*

To assess sensitivity and dynamic range, we simultaneously spiked four of the twelve targets into 50-µL incubation mixes at amounts ranging from 1 to 2187 amol. The four targets used in calibration (let-7a, miR-210, miR-221, and miR-222) were chosen for their diversity of 3' nucleotides, hairpin melting temperatures, and relative binding rates. We observed a linear detector response over four logs, with sub-attomole sensitivity achieved for three of the four targets (Figure 4.7 and Figure 4.8) and strong agreement between neat samples and those spiked with 200 ng of *E. coli* total RNA to add complexity. By

comparison, existing bead-based approaches have a 200-amol limit of detection and only one log of range [41]. To assess specificity, we performed assays with let-7a particles and four members of the let-7 family spiked separately at 200 amol into samples containing 200 ng *E. coli* total RNA. Scans revealed a maximum cross-reactivity of 27%, which is lower than other systems [138] (microarray ~50%) and can be dramatically improved with lower hybridization salt concentrations (Figure 4.9). These assays were very reproducible, with intra- and inter-run CV's of 2–7% (Table 4.3). Due to limitations in detection and particle preparation, it is common for users of current bead-based systems to employ 4,500 copies of each type of bead in an assay for high-confidence estimates of target level [2]. By contrast, we found it sufficient to analyze only 10–15 hydrogel particles for each probe type (Figure 4.10).

	1 amol	3 amol	5 amol	9 amol	27 amol	81 amol	243 amol	729 amol	2187 amol
miR-210	59.45	29.22	10.88	10.93	1.81	5.91	1.39	5.85	1.93
miR-221	36.71	9.95	21.80	18.41	4.11	7.20	2.79	6.81	2.01
miR-222	-	5.96	16.10	15.62	4.85	5.25	3.26	5.93	3.27
let-7a	87.99	19.18	26.77	18.83	5.20	5.83	3.13	5.53	2.93

Table 4.3: *Intra-run CVs in target level for E. coli calibration curve. All entries are percentages with each statistic calculated using 19 particles on average. miR-222 exhibited a limit of detection over 1 amol. Inter-run CV in background-subtracted miSpike signal (100 amol) for the nine represented scan sets was 6.84%. Inter-run refers to different detections with the same batch of particles.*

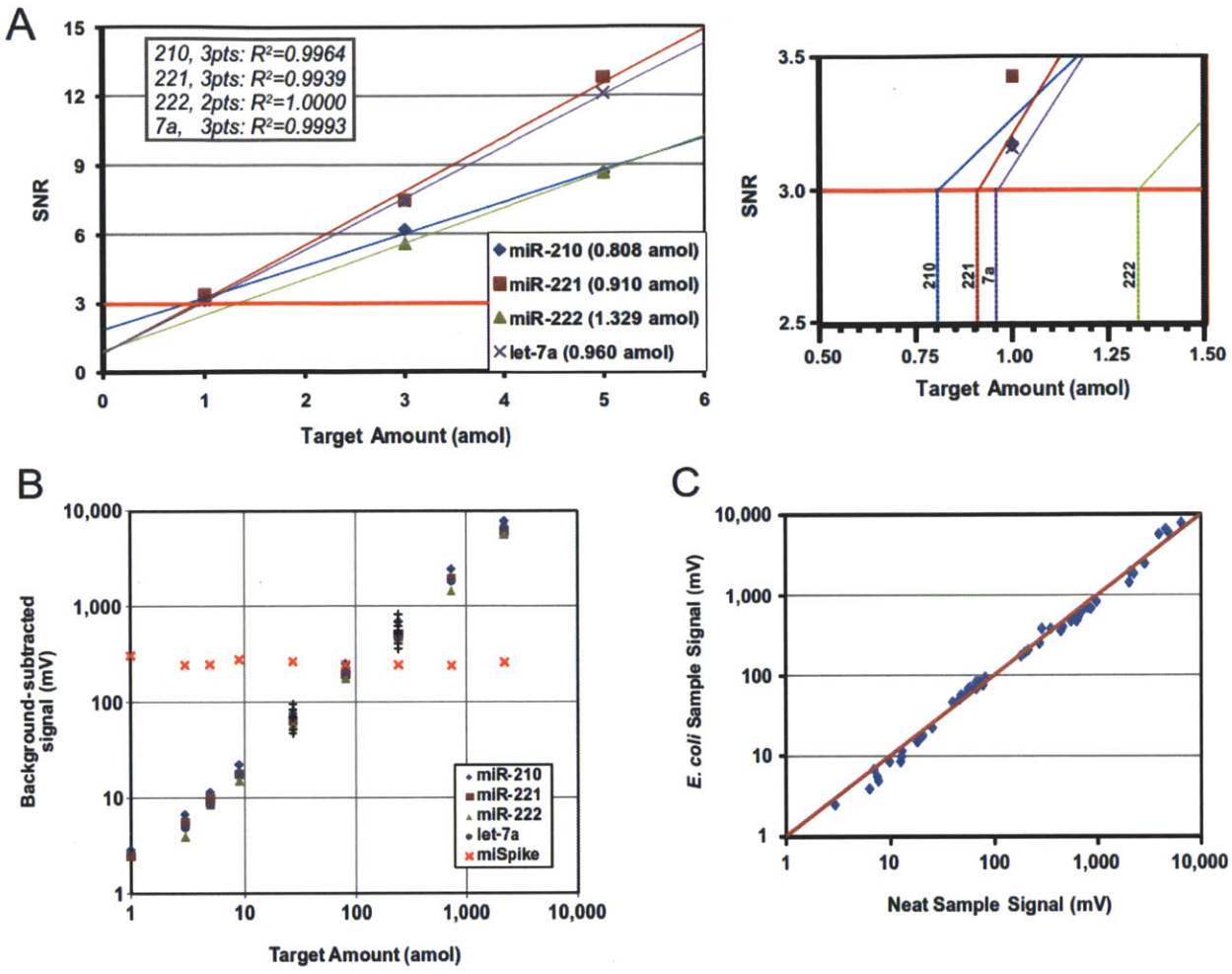

Figure 4.8: *Limit of detection calculations and calibration curves for neat samples. (A) Extrapolation of SNR for determination of LOD. The LODs of the four calibration targets (see legend) were calculated by finding the target amount at which the SNR was three. Regression lines with a mean Pearson coefficient of 0.9965 (excluding miR-222) were used to extrapolate LODs. (B) Neat calibration curves for particle batches incubated without spiked E. coli total RNA. Except for the absence of E. coli RNA, conditions are identical to those used to construct Figure 4.7 A. The remaining seven naturally-occurring targets (+ symbols) were spiked into the 27- and 243-amol trials to validate performance. (C) Comparison of background-subtracted signals from neat and E. coli calibration measurements. Clustering of points around the identity line (red) indicates highly specific detection with no noticeable decrease in binding rates in more complex samples. For all plots, all target levels (except miSpike) have been adjusted for comparison purposes by using the background-subtracted signal from the 100-amol miSpike profiles.*

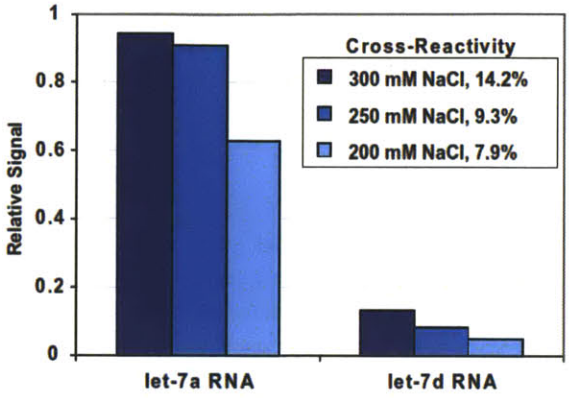

Figure 4.9: *Effect of hybridization buffer salt concentration on cross-reactivity between let-7d miRNA and let-7a probe. Particles bearing a let-7a probe region were incubated with 500 amol of synthetic let-7a or let-7d RNA for 90 minutes at 55°C with varying amounts of NaCl. Particles were labeled using the standard ligation/reporter protocol. Probe region fluorescence was measured and scaled using the let-7a fluorescence signal for particles incubated at 350mM NaCl (as used in the 12-plex study in the main text).*

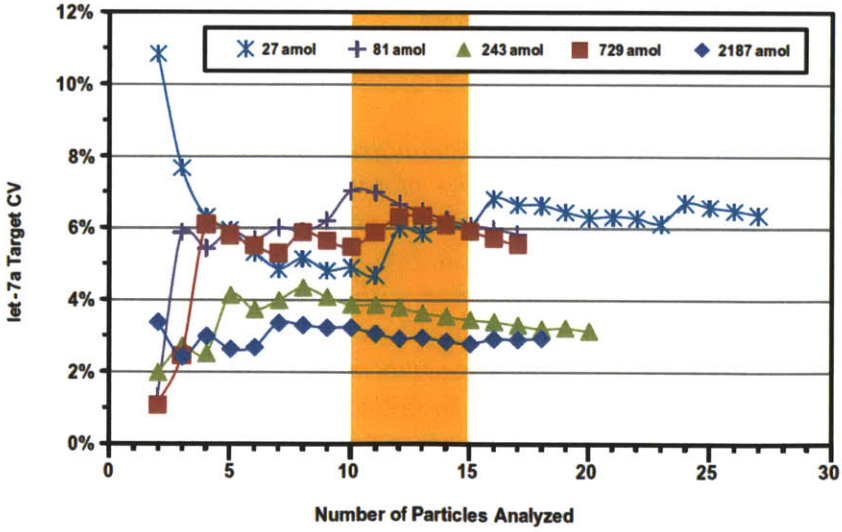

Figure 4.10: *Coefficient of variation (CV) of target level as a function of number of particles analyzed. The CV of the target level for let-7a in the E. coli calibration scans was seen to stabilize to a nearly constant value in the 10–15 particle window for the five spike-in amounts presented above. More information about intra-run target-level CVs can be found in Table 4.3.*

4.5 Dysregulation Analysis of Human Total RNA

As a further validation of the platform, we performed expression profiling across tumor and adjacent normal tissue for several cancer types. As anticipated, we observed the dysregulation of miRNA targets in all of the diseases investigated (Figure 4.7 C, Table 4.4, and Table 4.5). Although we used 250 ng of total RNA for these samples, similar profiling results were obtained for lung samples using only 100 ng, suggesting that less input RNA would be sufficient. Aliquots of the lung samples were profiled with qPCR by the Dana Farber Cancer Institute's Molecular Diagnostics Laboratory to independently confirm our results. The two platforms exhibited strong agreement for the seven targets available for comparison (Figure 4.7 C). With a simple workflow and a total assay time of only 3 h, the profiling is far more efficient than microarray approaches (~24 h) [138] and recent amplification schemes (~9 h) [196], and it exhibits sensitivity and reproducibility superior to that of existing bead-based methods [41, 59].

	let-7a	miR-21	miR-29b	miR-181b	miR-143	miR-145	miR-146a	miR-210	miR-221	miR-222	RNU6B
Lung Tumor	594.81	1498.85	68.36	7.02	85.61	162.88	77.02	-	7.21	8.13	57.16
Lung Healthy	368.08	141.70	31.80	2.69	59.79	189.07	6.95	-	-	6.45	10.84
Breast Tumor	1094.19	808.08	65.88	3.71	32.48	73.53	9.26	-	-	2.29	116.88
Breast Healthy	912.95	302.39	32.87	2.65	59.01	149.06	12.90	-	-	10.20	78.55
Stomach Tumor	270.64	561.87	68.78	2.28	169.45	388.39	29.66	-	2.93	14.15	175.69
Stomach Healthy	258.28	204.24	73.44	-	186.39	597.31	3.33	-	-	7.83	78.45
Pancreas Tumor	44.96	14.96	9.95	-	5.43	22.63	-	-	-	-	9.49
Pancreas Healthy	98.10	18.21	14.85	-	6.79	10.88	-	-	-	-	10.33

Table 4.4: *Mean target amounts and inter-run CVs in target amount for 250-ng tissue assays. Top number in each entry is mean amount for replicate trials (amol); bottom number in parentheses is the inter-run CV (%). Amounts were determined by comparison to the background-subtracted 100-amol miSpike signal from each run. Replicate assays were conducted on different days to rigorously test reproducibility. Each statistic was calculated using 16 particles on average. Entry spots lacking data indicate that target was not present above the 2-amol cutoff.*

	let-7a	miR-21	miR-29b	miR-143	miR-145	miR-146a	miR-181b	miR-222
Lung	-0.5119	0.3020	-0.3911	-0.5670	-0.7870	0.3232	-0.3066	-0.6210
Breast	-0.0942	0.2532	0.1378	-0.4318	-0.4801	-0.3168	-0.0266	-0.8253
Stomach	-0.3310	0.0966	-0.3844	-0.3877	-0.5336	0.6007	0.3294	-0.0935
Pancreas	-0.3023	-0.0198	-0.1402	-0.1251	0.3534	-	-	0.1785

Table 4.5: *Log-transformed expression ratios for 250-ng assays. Top number in each entry is the mean of the log-transformed ratios of tumor amount-to-healthy amount of the indicated target in the specified tissue over three trials; bottom number in parentheses is the standard deviation. Entry spots in red indicate dysregulation. Entry spots lacking data indicate that the ratio was not calculated. miR-210 and miR-221 were omitted because they did not appear above the 2-amol cutoff in both tumor and healthy samples in any of the four tissues investigated.*

In past work, gel particles were imaged with a CCD camera and then analyzed at rates <1 particle/min. For the mock 60-plex assay demonstrated here (*i.e.*, five codes per probe type), the scanner provided a decoding accuracy of ~98%, with only ~10% score-based rejection at throughputs up to 25 particles/s. This represents a 1,500-fold increase in analysis rate. With manual loading from Eppendorf tubes, eight 50-μL samples could be scanned and analyzed in 30 min, leading to a projected throughput of ~125 samples per 8-h workday. In future applications of this technology, it is expected that automation of the particle-loading and rinsing processes using well-plates and a liquid handling system will greatly augment efficiency to levels that match or exceed state-of-the-art particle analysis systems used for genotyping (>500 samples/day) [35].

4.6 Data Analysis

In this work, raw data files (20 million points/scan) produced by the scanning process were analyzed with a custom MATLAB algorithm designed to isolate individual particle signatures, identify the code displayed by each particle, and quantify the amount of target bound. The algorithm processed scans of 50-μL samples in under 5 s, making the approach suitable for high-throughput applications. In the initial filter step, the algorithm excised portions of the scan that exceeded a threshold voltage and then interrogated each removed segment for characteristics that identified it as a particle signature. Using specific properties of the fluorescent code region as reference points, a high-confidence estimate of the velocity of each particle was determined and utilized to pinpoint trough locations for the five coding holes. The orientation of the particle (*i.e.*, probe- or code-first) was established using the fixed-value "3" hole that bordered the inert region. After an initial code identity was calculated from the trough depths, a secondary review was conducted by measuring the standard deviation in trough depths of holes designated to be of the same level and corrective action was taken if necessary. In the final decoding step, a confidence score was calculated for the particle by computing the linearity of the correlation between trough

depth and assigned level. A particle decoding event was rejected if its Pearson coefficient fell below 0.97.

In order to calculate the amount of target bound, the measured particle velocity was used to infer the location of the center of the probe region. Briefly, a search window was used to investigate the scan in this region, seeking to identify a local maximum that could be correlated to a target-binding event. If a maximum was found, the position of the search window along the scan profile was adjusted until the two endpoints were sufficiently close in signal amplitude, thereby selecting a nearly symmetrical portion of the maximum over which to average for quantification purposes. In the cases in which a maximum was not found, the original estimate of probe center was used to calculate a mean signal without a search window. To calculate the background for a given probe sequence and incubation condition, particles from the same synthesis batch were incubated in the presence of *only* 100 amol of miSpike target according to the procedure described above. This method provided a measure of the probe-dependent background that arose from the PEG scaffold and the universal adapter used in the labeling process. Also, upon calculation of all code identities and target levels, a particle would be rejected from consideration if its target level was more than one inter-quartile range above the third quartile or below the first quartile of the data set consisting of target levels associated with the probe in question. This measure was taken as further protection against incorrect code assignments and inter-run contamination.

For calibration and profiling studies, mean background-subtracted signals were computed for each target at each incubation condition. For inter-run comparisons of calibration data, signals were normalized by background-subtracted miSpike amplitude, with the null (0 amol) samples providing the reference 100-amol miSpike value for both neat and *E. coli* investigations. miSpike target values displayed on the calibration curves (Figure 4.7 A and Figure 4.8 B) were not adjusted to this reference in order to demonstrate the repeatibility of the labeling and scanning process. For profiling studies, the background-subtracted miSpike signal from the first scan of each healthy tissue type was used as the reference for analysis of that tissue. Signals from a given profiling scan were further normalized by the RNU6B amount in that scan to facilitate direct quantitative comparisons that were independent of total RNA amount [197]. Repeat runs of tissue assays were conducted at least one day after the original. Assays of 250-ng tissue samples were repeated in triplicate, while assays of 100-ng samples were performed once to provide a basis of comparison. For each calculated expression ratio, the healthy and tumor samples were assayed and scanned in the same set of experiments for consistency. We required at least 2 amol of target to be detectable in a tissue of a given disease state in order to calculate an expression ratio. As we only used a single patient sample for each tissue type, we implemented a threshold approach to determine dysregulation. For each target in each tissue, the three log-transformed expression ratios from the three separate trials were used to calculate an SNR, by dividing the mean of the set by the standard deviation. Targets with SNRs above 3 were considered to be dysregulated. It should be noted that all 20 instances of dysregulation were

able to be correlated to observations from the literature regarding the expression profiles of either mature miRNA (16 of 20) [117, 125, 187, 198-200] or miRNA precursors (4 of 20) (Figure 4.11) [201, 202].

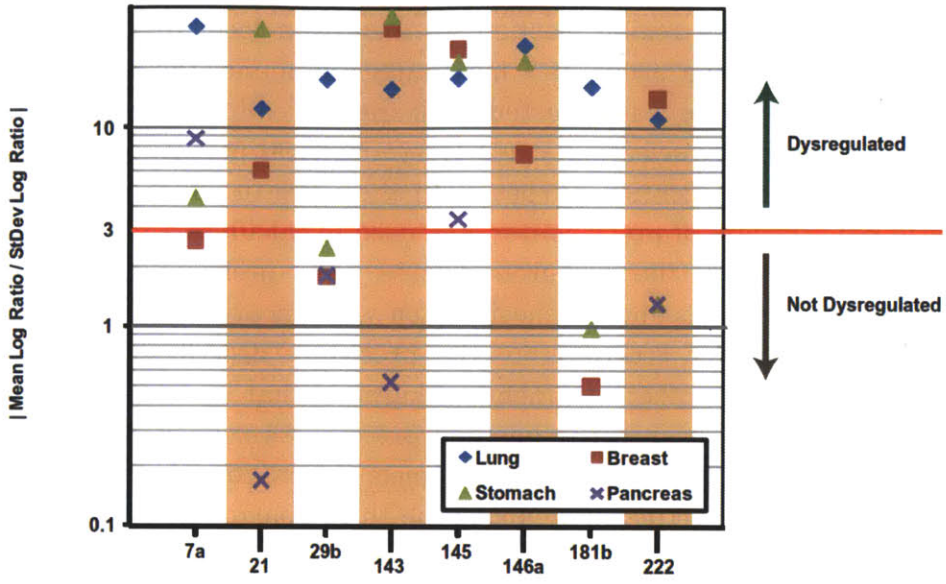

Figure 4.11: *Dysregulation classification. A SNR was used to distinguish dysregulated targets in tissue profiling. The mean and standard deviation of the log-transformed expression ratio were calculated for each target in each tissue for the triplicate assays. A SNR of three was chosen as the threshold for dysregulation. All 20 instances of dysregulation matched observations in the literature. miR-210 and miR-221 were omitted because they did not appear above the 2-amol cutoff in both tumor and healthy samples in any of the four tissues investigated.*

Chapter 5

Ultrasensitive MicroRNA Detection via Rolling Circle Amplification

There is great demand for flexible biomolecule analysis platforms that can precisely quantify very low levels of multiple targets directly in complex biological samples. In this chapter we demonstrate multiplexed quantification of miRNAs on encoded hydrogel microparticles with sub-femtomolar sensitivity and single-molecule reporting resolution. Rolling circle amplification (RCA) of a universal adapter sequence that is ligated to all miRNA targets captured on gel-embedded probes provides the ability to label each target with multiple fluorescent reporters and eliminates the possibility of amplification bias. The high degree of sensitivity achieved by the RCA scheme and the resistance to fouling afforded by the use of gel particles are leveraged to directly detect miRNA in small quantities of unprocessed human serum samples without the need for RNA extraction or target-amplification steps. This versatility has powerful implications for the development of rapid, non-invasive diagnostic assays.

5.1 Introduction

The growth of molecular diagnostics requires innovative tools that are sensitive, specific, and precise enough to quantify low levels of multiple biological targets simultaneously in complex media in a single assay. To minimize assay development time and cost, these systems should be flexible enough to allow for rapid probe-set modification, standard post-assay analysis methods, and the interrogation of diverse classes of clinically relevant

biomolecules. MicroRNAs are small noncoding RNAs that have been shown to have powerful predictive value in determining diagnosis and prognosis for several diseases including cancer, diabetes, and Alzheimer's [117, 125, 187, 203]. It has proven difficult, however, to accurately and efficiently quantify this increasingly important target set in biological samples due to high levels of sequence homology, complex secondary structures, and wide ranges of natural abundance [134]. Microarray, deep sequencing, and PCR-based approaches for miRNA quantification provide high sensitivity but ultimately are ill-suited for the high-throughput analysis of small, focused clinical target panels, an application space that is quickly expanding due to interest in personalized medicine [12, 138, 139, 149]. With shorter, customizable workflows and rapid post-assay analysis options, particle-based arrays offer a more economical solution for such applications, but the relatively poor sensitivity of commercially available particles requires significantly larger sample amounts [44, 59, 204, 205]. The ideal platform for the analysis of focused miRNA biomarker panels would provide high sensitivity and specificity, scalable multiplexing with a simple workflow, and the ability to directly interrogate easily-obtainable biological samples without the need for RNA extraction.

It has recently been shown that miRNAs are remarkably stable in the RNase-rich environment of blood because of their association with the Argonaute2 ribonucleoprotein complex and membrane-bound vesicles [127, 128]. As a result, these small noncoding RNAs have become an attractive target set for the development of non-invasive blood-based bioassays and for the study of novel mechanisms of intercellular communication [127, 206-208]. Unfortunately, the quantification of circulating miRNAs is particularly challenging due to low levels of natural abundance, as well as the biological complexity of blood and its derivatives (plasma and serum). While microarray and PCR-based methods have been developed to profile serum-based miRNAs, all existing approaches require RNA isolation and/or target amplification, which complicates assay workflow as well as quantification [206-208]. The development of efficient diagnostic assays in this biological medium requires a highly sensitive multiplexing platform capable of direct target detection in minute amounts of sample without the need for complex, time-consuming processing and purification steps.

In order to enhance the sensitivity of a biological assay, one can either amplify the number of targets present in a sample or amplify the reporting signal produced by each of the targets. Target-based amplification via PCR has been widely used as a means to profile low-abundance miRNA [139]. However, great care must be taken in the optimization of primer sequences to prevent amplification bias in multiplexed assays and to ensure accurate quantification of target amounts. Signal-based amplification improves sensitivity without augmenting the number of target molecules, and as a result, offers a more direct route to biomolecule quantification, even allowing for single-molecule reporting resolution. Several signal amplification strategies have been adapted for the quantification of miRNA, including RCA and isothermal ramification amplification (RAM) [204, 209-212]. In these approaches, the polymerase-mediated replication of a circular template is used to create

long DNA concatemers either in solution or immobilized on a substrate that can be labeled with multiple fluorophores or radioactive isotopes, thereby amplifying the signal generated from a single target molecule to a level that can be observed using standard detection instruments. Although significant enhancements in detection performance have been achieved with signal-based amplification, the LODs demonstrated with such approaches remain considerably higher than those obtained with quantitative PCR, preventing their use in emerging applications such as the direct quantification of multiple miRNAs from single cells or easily-obtainable body fluids [204].

We sought to investigate the use of RCA for multiplexed miRNA quantification on graphically-encoded hydrogel microparticles [52, 180, 205]. In a typical assay, a custom mix of particles bearing DNA probes complementary to the desired target miRNA sequences are exposed to a sample solution, specific targets are captured on the immobilized probes, and the captured miRNA molecules are then fluorescently labeled for quantification. The selective labeling of only those miRNAs that have been specifically captured on immobilized probes has several advantages over the bulk enzymatic and chemical methods used in the majority of direct detection schemes, including higher efficiency, lower cost, and reduced likelihood of labeling bias due to secondary structure [138, 193, 194]. In previous work with these particles, we demonstrated a post-target-hybridization labeling procedure that ligated a universal adapter sequence with a single fluorophore to each target captured on or within the microgel particles for attomole-level miRNA quantification and rapid dysregulation analysis in low-input human total RNA for cancer profiling [205]. Because the same adapter can be used for *all targets* in a multiplex assay, this scheme provides a convenient means for developing signal-based amplification without the risk of sequence bias.

In this chapter, an RCA-based signal amplification strategy is used to achieve sub-femtomolar multiplexed quantification of miRNA on encoded microgels with single-molecule reporting resolution. A primer site is incorporated into the 3' end of the universal adapter, and then each ligated adapter (Figure 5.1) is extended through the introduction of a circularized DNA template and Phi29 DNA polymerase, a highly processive enzyme capable of more than 50,000 base insertions per binding event [213]. The enzyme's excellent strand displacement allows for the use of small circular templates, the repeated 'rolling' of which results in the production of extensions bearing hundreds of replicate sequences that can each be fluorescently labeled through the hybridization of appropriately decorated reporter oligonucleotides (Figure 5.1). This method greatly expands the utility of our multifunctional gel particle platform by enhancing sensitivity to a level that allows for the direct detection of miRNA in small amounts of serum without the need for RNA extraction or potentially biasing target-amplification steps [52, 180, 205, 214]. With RCA and fluorescent spot-based quantification, we achieve miRNA detection sensitivity superior to that of existing particle arrays, RCA approaches, and conventional microarrays [204].

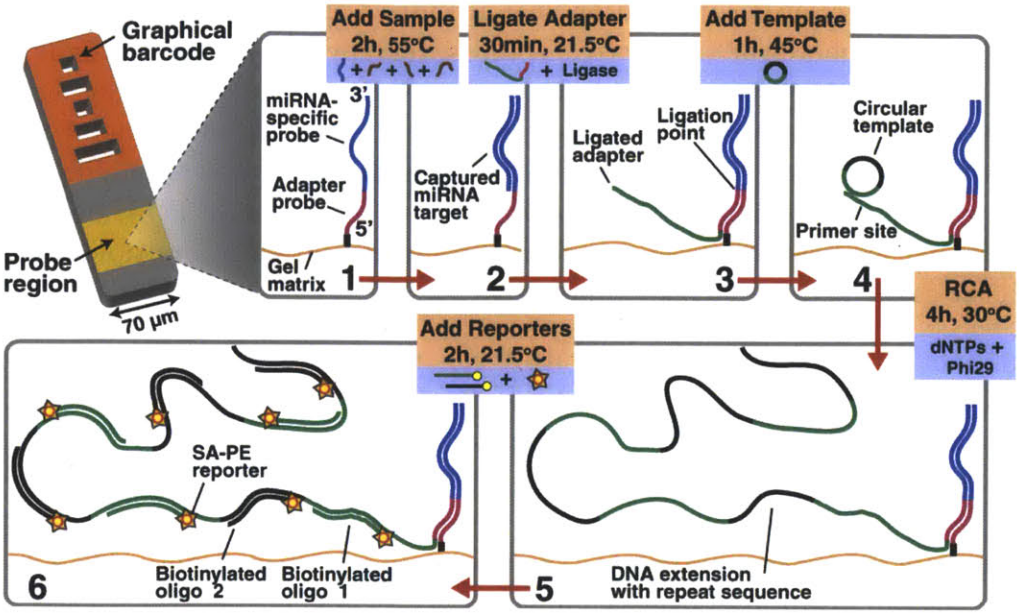

Figure 5.1: *Gel particle RCA workflow. A graphical barcode consisting of unpolymerized holes in the wafer structure of the particle indicates the miRNA-specific probe embedded within a different region of the gel. Particles are incubated with sample, after which a universal adapter sequence with a primer site is ligated to the 3' end of all captured targets and a circular template is allowed to anneal. Phi29 polymerase and dNTPs are incubated in a custom reaction buffer at 30°C to generate a DNA extension with repeat sequences, each of which can be labeled with two distinct biotinylated oligonucleotides attached to SA-PE.*

5.2 RCA Optimization

Although RCA has been widely used to enhance signal transduction on solid surfaces [176, 215-217], there is limited information on the technique's performance on gel-based substrates [22, 218]. Our hydrogel particle platform is highly advantageous for bioassays, as it has proven to be both bioinert and non-fouling in complex biological media [214]. However, careful optimization must be undertaken when introducing new labeling reagents that can alter the environment of the stimuli-responsive microgels. To evaluate the compatibility of RCA and our microgels, we created particles with a probe region embedded with a previously described DNA sequence capable of capturing miR-210 target and our universal adapter sequence (Table 5.1) [205]. Upon testing the detection of 10 amol of synthetic miR-210 RNA with a primer-modified adapter and two commercial RCA buffers from New England Biolabs (Ipswich, MA) and Epicentre Biotechnologies (Madison, WI), we observed significant non-specific binding of fluorescent labels on all portions of the particles. In an attempt to isolate the reagent(s) responsible, we prepared several "knockout" buffers using NEB2, which had proven to be compatible with the gel particles during earlier ligation studies. Each knockout buffer either eliminated one of the

constituents of the commercial RCA buffers altogether or reduced it to the lower level found in NEB2. When the Tris-HCl concentration was reduced from 40–50 mM to 10 mM in the RCA buffer, the majority of the fouling was eliminated without negatively impacting the amplification process, indicating that lower buffer pH was responsible for the non-specific adsorption onto the gel matrix. The remaining noise was removed by supplementing the customized buffer with BSA at a concentration of 200 μg/mL. In separate experiments, incubation conditions and the concentrations of circular template, DTT, dNTPs, Phi29 polymerase, and reporter sequences were adjusted to ensure the highest possible signal-to-noise ratio.

	Sequence (5' to 3')
miR-141 Probe	/5Acryd/ GAT ATA TTT TAC CAT CTT TAC CAG ACA GTG TTA /3InvdT/
miR-210 Probe	/5Acryd/ GAT ATA TTT TAT CAG CCG CTG TCA CAC GCA CAG /3InvdT/
miR-221 probe	/5Acryd/ GAT ATA TTT TAG AAA CCC AGC AGA CAA TGT AGC T /3InvdT/
cel-miR-39 Probe	/5Acryd/ GAT ATA TTT TAC AAG CTG ATT TAC ACC CGG TGA /3InvdT/
Universal Adapter	/5Phos/ TAA AAT ATA TAA AAA AAA AAA ATC AGA ACA GTC TCG GAA GGA
Circular Template	/5Phos/ TAA GTC ATT CGC ACA GGA GCA ACA GAC GAG TCC TTC CGA GAC TGT TCT GA
Reporter Oligo 1	GCA CAG GAG CAA CAG ACG AGA AAA AA /3Bio/
Reporter Oligo 2	CGA GAC TGT TCT GAT AAG TAA AAA A /3Bio/

Table 5.1: *DNA sequences used for RNA target capture and labeling. "5Acryd" refers to 5' acrydite modification (for covalent incorporation into the PEG-DA gel matrix), "3InvdT" refers to 3' inverted dT modification (to prevent incidental ligation of adapter to the end of the probe), "5Phos" refers to 5' phosphorylation (for ligation), and "3Bio" refers to 3' biotinylation (for attachment of streptavidin-phycoerythrin (SA-PE) reporter). Underlined portions of probes are target-specific capture sites. Blue letters indicate sequence portions involved in universal adapter binding. Red letters indicate sequence portions involved in circle binding.*

5.3 Assay Optimization

The RCA protocol depicted in Figure 1 was optimized through a parametric study of reagent types and concentrations. Commercially-available RCA buffers from Epicentre Biotechnologies and New England Biolabs proved to be incompatible with our gel-particle system, and thus we explored the use of other solutions. NEB2 buffer had been successfully used in previous ligation-labeling studies. In addition, it contained the same concentration of $MgCl_2$ as the commercially-available RCA buffers (but less Tris-HCl, DTT, and $(NH_4)_2SO_4$) and was thus chosen for further study (Table 5.2). The use of NEB2 as an RCA reaction buffer led to reduced signal from 10 amol miR-210 spike-ins when compared to the commercially available buffers, but it also produced clean particles that were not plagued by non-specific adsorption of fluorescent label and particulate debris. As a result, NEB2 was supplemented with Tris-HCl and DTT to match levels used in the commercially

available buffers in an attempt to recover Phi29 enzyme activity and eliminate non-specific adsorption.

NEB2 Buffer (1×, NEB)	Phi29 Reaction Buffer (1×, Epicentre)	Phi29 Reaction Buffer (1×, NEB)	T4 DNA Ligase Buffer (1×, NEB)
50 mM NaCl	50 mM KCl	50 mM Tris-HCl	50 mM KCl
10 mM Tris-HCl	40 mM Tris-HCl	10 mM $MgCl_2$	50 mM Tris-HCl
10 mM $MgCl_2$	10 mM $MgCl_2$	4 mM DTT	10 mM $MgCl_2$
1 mM DTT	4 mM DTT	10 mM $(NH_4)_2SO_4$	10 mM DTT
pH 7.9 at 25°C	5 mM $(NH_4)_2SO_4$	pH 7.5 at 25°C	1mM ATP
	pH 7.5 at 25°C		pH 7.4 at 25°C

Table 5.2: *Buffer compositions for RCA optimization.*

It was observed that supplementing the NEB2 buffer with only enough DTT to raise the concentration to 4 mM rescued the activity of the enzyme, restoring it to a level that was comparable to that seen in the commercially available buffers while noticeably reducing non-specific adsorption. The Tris-HCl supplement, meanwhile, did nothing to increase the RCA performance, and it produced "sticky" particles that non-specifically adsorbed fluorescent labels and particulate debris (similar to the commercial buffers). Further experiments with NEB4 buffer and T4 DNA ligase buffer from New England Biolabs seemed to confirm the hypothesis that higher Tris-HCl content and lower pH were responsible for non-specific adsorption, while elevated DTT concentration was essential for efficient polymerase activity. Additional parametric experiments eventually led to the use of an NEB2 buffer supplemented with DTT, BSA, TE, and Tween-20. During optimization, we found that high levels of Tris-HCl (>10 mM), DTT (>5 mM), Phi29 (>400 U/mL) and dNTPs (>150 μM each) in the RCA incubation mix promoted non-specific binding of the reporter oligonucleotides, which in turn produced high levels of fluorescent background on all regions of the hydrogel microparticles. We also observed higher background and occasional particle aggregation when concentrations of circular template greater than 75 nM were used; in future work, an additional step to purify/isolate the circularized template from the solution in which it was synthesized could potentially eliminate this.

For the low target amounts considered in this study (<50 amol), the vast majority of the target-binding events occurred on probes immobilized near the surface of the hydrogel particle. This can be attributed to the probe-target reaction rate being relatively fast compared to target diffusion through the gel matrix, as well as the fact that the collection of probes near the surface will avoid saturation [52, 180, 205]. Because of this binding pattern, we imaged the top and bottom faces of each tablet-shaped particle in order to quantify the fluorescent signal arising from target-binding. For higher target amounts, fluorescence was integrated over the top and bottom faces of each probe region and then averaged. For lower amounts where individual DNA-reporter coils could be distinguished, fluorescent spots on the top and bottom faces of each probe region were summed.

We investigated the effect of RCA extension time on signal intensity by incubating 5 amol of synthetic miR-210 with ~20 particles bearing an appropriate probe (Figure 5.2). The number of discernable spots increased over the first 4 h of extension, but there was no noticeable difference in spot count between RCA times of 4 and 8 h. However, the fluorescence intensity of each spot increased throughout the examined time range, with evidence of a plateau emerging by hour 16. The higher signal intensity seen at the sides of the particle beginning at 4 h (Figure 5.2) is due to the labeling of targets bound to the side faces of the particle's probe region. RCAs were also performed in the absence of miR-210 target for the extension times seen in Figure 5.2 to generate appropriate control measurements for each time point. Signal arising from these particles was subtracted from the 5 amol spike signals to generate background-subtracted measurements. Although background fluorescence levels increased slightly over time, the low spot count on the 16-h control particles and the absence of non-specific binding of debris suggests that overnight extension for intense amplification is feasible for the gel-particle system. To shorten assay time, ensure that all target-binding events were detectable, and minimize signal variability, we chose to extend for 4 h for all subsequent RCA trials in this study.

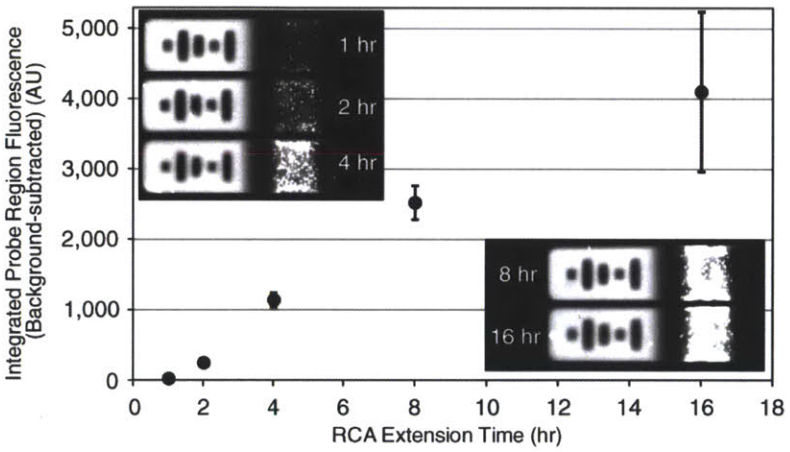

Figure 5.2: *Background-subtracted target signal as a function of RCA extension time for 5 amol spike of synthetic miR-210. Five distinct groups of particles were exposed to target and five distinct groups of particles were incubated without target to obtain appropriate background measurements. For each time point, one batch with target and one batch without target were processed with the specified RCA extension time and then labeled using the methods detailed in Section 2.3.5. Fluorescence was integrated over the probe region, with each data point representing the mean of at least five top and five bottom faces. Error bars represent standard deviation of signal.*

5.4 Detection Performance

The optimized protocol was used to investigate the detection of miR-210 over a concentration range of three orders of magnitude. Previous miRNA multiplexing experiments with gel particles and ligation-based labeling determined 350 mM NaCl to be optimal for achieving highly specific target binding with short incubation times. To simulate biological complexity and assess the specificity of the RCA scheme, 100 ng *E. coli* total RNA was added to each 50 μL incubation volume. As illustrated in Figure 5.3 A, the number of spots decreased as the target amount was reduced, and the code and other non-probe-bearing portions of the gel particles exhibited very low levels of background. The low spot count on the control (0 amol) particles demonstrated that only the intended target was being captured and labeled even in the presence of a great excess of non-target RNA sequences. It should be noted that 100 ng total RNA is sufficient for robust multiplexed profiling with the non-amplified gel-particle protocol [205], and thus profiling in total RNA with the RCA scheme would use far less input RNA (0.1–10 ng, depending on target set) [204]. Figure 5.3 B shows stationary scans of particles exposed to either 0 or 5 amol of miR-210, along with a magnified fluorescence image of the probe region and the coils of reporting DNA that have formed on its top face. To assess the scheme's suitability for efficient multiplexing of low-abundance miRNA targets, we next created a batch of multi-probe particles with spatially segregated capture sequences for miR-141, miR-210, and miR-221, a panel of human miRNAs known to be frequently dysregulated in cancer profiling studies [125, 203, 205]. When the three targets were added in different amounts to an incubation mix containing the multi-probe particles, the expected signal pattern was obtained upon particle analysis (Figure 5.3 C).

To more fully characterize multiplexing performance, we developed an assay with three separate particle types designed for the detection of the three aforementioned human sequences as well as a fourth particle type for the detection of a *C. elegans* miRNA (cel-miR-39) commonly used as an external control for quantifying RNA recovery in detection protocols that require nucleic acid extraction [127, 128]. For single-probe particles, stream widths were adjusted during synthesis procedures to create code and probe regions that spanned 140 and 45 μm, respectively, of the length of the particles. Inert regions accounted for the remaining 65 μm of the length. Synthetic human miRNA targets in amounts ranging from 50 zmol to 35 amol were spiked into 50 μL incubation volumes containing ~20 particles of each type and 100 ng *E. coli* total RNA. With the exception of the 35 amol spike, the three human miRNAs were introduced simultaneously; separate spikes were performed at 35 amol to verify that target capture was probe-specific. Integrating signal intensity on the faces of the probe region provided a linear calibration curve for target amounts of 100 zmol or greater (Figure 5.4 A). Meanwhile, counting the number of amplification spots was an effective means of calibrating the detection for all sub-attomole amounts investigated (Figure 5.4 B-D). Importantly, particles bearing probe for cel-miR-39 exhibited consistently low spot counts for all calibration trials (Figure 5.4 A,E), indicating a high level of specificity of target capture and signal amplification.

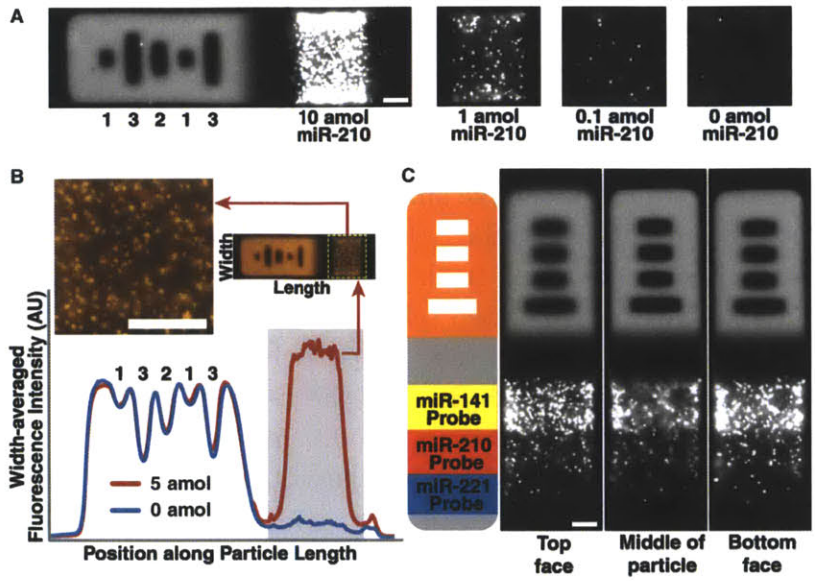

Figure 5.3: *Results with optimized RCA protocol. (A) Fluorescence images of binding events on top face of particle for detection of 10, 1, and 0.1 amol of synthetic miR-210 in buffer spiked with 100 ng E. coli total RNA. (B) Overlaid stationary scans of particles exposed to solution containing either 0 or 5 amol of miR-210, with magnified color image of probe region. Each scan represents the mean of five top and five bottom faces. (C) Multi-probe particle exposed to solution containing 5 amol miR-141, 1 amol miR-210, and 0.2 amol miR-221. Scale bars are 20 μm.*

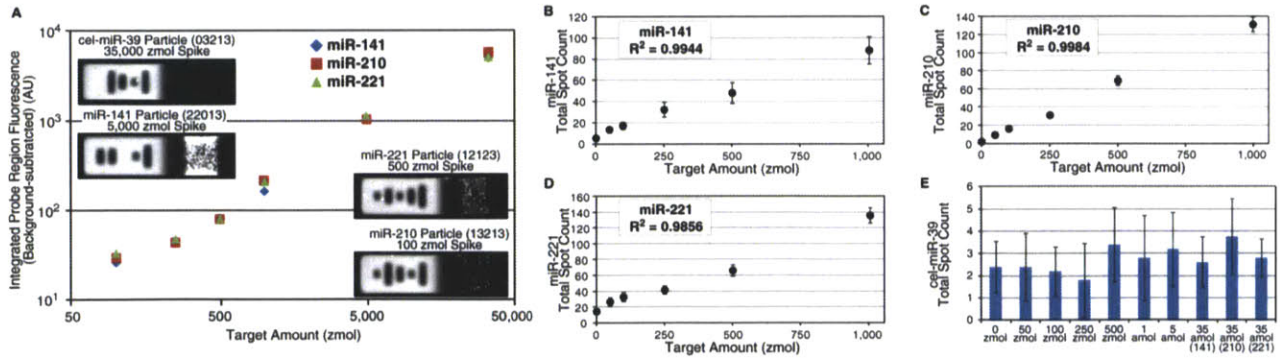

Figure 5.4: *Calibration of RCA method. (A) Calibration curve for multiplexed assay. Fluorescence was integrated over probe region for target spikes of 100–35,000 zmol. Particles bearing probe for cel-miR-39 were used as a negative control. (B–D) Fluorescent spot counts for target spikes of 0, 50, 100, 250, 500, and 1000 zmol in a multiplexed assay. The measurement resolution demonstrated here is suitable for dysregulation profiling of targets in the sub-attomole range. (E) Fluorescent spot counts on cel-miR-39 particles for the calibration trials. In all trials depicted in Figure 5.4, 100 ng E. coli total RNA was added to incubation buffer to simulate complexity and demonstrate specificity of assay. Error bars represent intra-trial standard deviation.*

We observed high reproducibility in detection performance at the low target levels investigated in this study. The gel particles were fabricated, encoded, and functionalized with probe in a single step using a high-fidelity microfluidic synthesis process that provides a greater degree of reproducibility and uniformity than the multi-step batch synthesis processes used to create and functionalize similar particle systems. The mean intra-trial CV of target signal for sub-attomole detection with spot-counting was 14% when measuring five gel particles of each type in a given trial. By comparison, the mean intra-trial CV for attomole detection with the non-amplified scheme was 62% [205], while competing particle systems require the analysis of thousands of particles for high-confidence estimates of target levels 5,000-fold higher [2]. With RCA on the gel particles, an inter-trial CV of 15% was calculated for three separate detections of 500 zmol miR-210 on three separate days. LODs for each of the human miRNAs were calculated from the calibration curves in Figure 5.4 B–D. The lowest LOD was that of miR-141, which was detectable down to 15 zmol (~9,000 copies or 300 aM in 50 μL incubation volume). This level of sensitivity is superior to those demonstrated by existing particle arrays, blots, RCA schemes (dumbbell, padlock blotting, branched), and conventional microarrays, and it should be sufficient for the direct profiling of highly-expressed miRNAs from single cells [204]. The unique hydrogel composition of our particles provides a hydrated, non-fouling scaffold that minimizes background signal from non-specific interactions and enhances nucleic acid hybridization relative to solid surfaces. As discussed elsewhere [10, 25, 180, 219], the three-dimensional immobilization of probe within a gel provides solution-like hybridization thermodynamics that lead to lower probe-target dissociation constants (and thus higher sensitivity) than can be obtained with solid particle systems and microarrays. Furthermore, the ability to immobilize probe within the gel microparticles concentrates the captured targets and resulting fluorescence signal within a relatively small volume for image analysis, leading to higher sensitivity than existing RCA approaches that use well-based spectrometer measurements and Northern blots for quantification.

We also calculated the percentage of spiked-in target miRNA molecules that were captured and labeled with this optimized assay. We determined this percentage by multiplying the background-subtracted spot count per particle by the number of particles in the reaction tube and then dividing by spiked amount. Assuming 20 particles per probe type in each incubation volume and using the spot counts for the 1,000 zmol spike trials in Figure 5.4, we arrive at capture percentages of 0.28%, 0.43%, and 0.40% for miR-141, -210, and -221, respectively. It should be noted that capture percentage can be improved by increasing the duration of the target hybridization step, decreasing the incubation volume used, and increasing the probe concentration within the particle.

5.5 Serum Assay

We sought to leverage the high sensitivity and specificity of the gel-particle RCA scheme for the detection of low-abundance miRNAs in complex biological media. Recent studies have

identified miRNAs as valuable blood-based biomarkers that could potentially be used for rapid, non-invasive determination of disease diagnosis and prognosis [128, 207, 208]. Unfortunately, the low target abundance and complexity of blood have hindered progress in developing accurate and efficient plasma- and serum-based assays, requiring target-amplification steps and time-consuming RNA extraction protocols that complicate quantification and introduce technical variability [207]. In an attempt to detect miRNA directly in 25 μL aliquots of human serum, we modified our assay protocol by adding SDS and RNase inhibitor (SUPERase-In) to an incubation buffer that would be combined with the serum. By measuring the recovery efficiency of synthetic cel-miR-39 spikes under a variety of conditions, it was determined that the optimal reaction mix should contain 2% SDS and 0.5 U/μL SUPERase-In to ensure the denaturation of both background and RISC-associated proteins, as well as the inhibition of serum-based RNases [127, 128]. We spiked 5 amol of cel-miR-39 into 50 μL mixes containing 25 μL of either normal or prostate-cancer-associated serum and observed recovery efficiencies comparable to those measured for spikes into our previous neat incubation buffers (Figure 5.5 A). Importantly, there was little evidence of non-specific binding on the surfaces of the bioinert, fouling-resistant PEG-based gel particles.

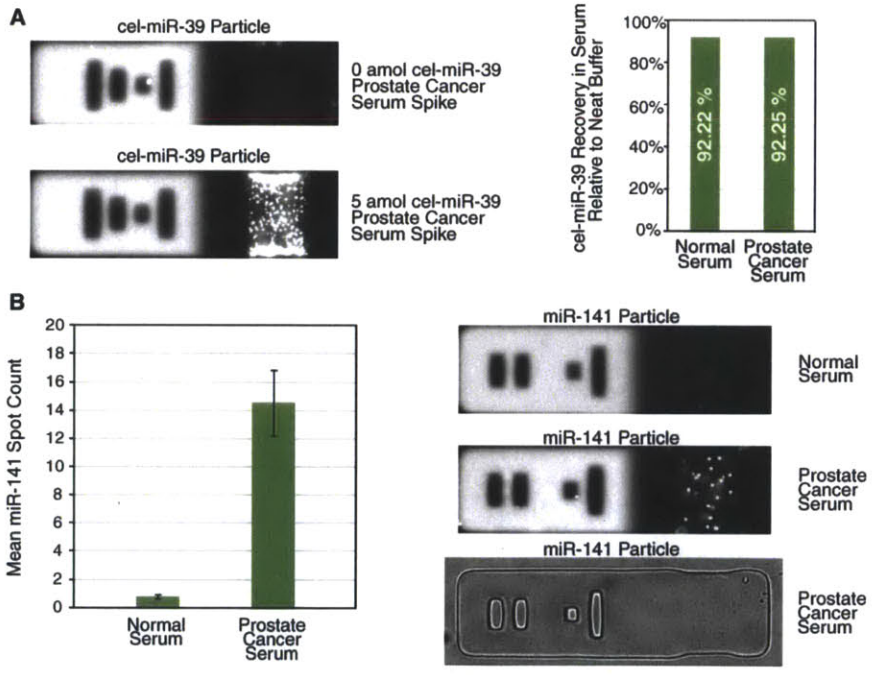

Figure 5.5: *Serum-based miRNA Assay. (A) Synthetic cel-miR-39 recovery efficiency for 5 amol spikes into normal and cancer-associated serum. (B) Upregulation of miR-141 was observed in prostate-cancer-associated serum. Data reflect the mean spot counts for three replicate trials. Error bars represent the inter-trial standard deviations.*

We also investigated the endogenous miR-141 levels in the two serum types, seeking to confirm a previous PCR-based study that found miR-141 to be upregulated in the serum of prostate cancer patients [128]. The results obtained with our gel particles for three technical replicate measurements of each serum type revealed a similar dysregulation, with mean spot counts of 0.78 ± 0.13 on particles exposed to normal serum and 14.53 ± 2.34 on those exposed to cancer-associated serum (Figure 5.5 B). The observed copy numbers of miR-141 (<400 copies/μL normal, 2,000 copies/μL cancer) also agreed with the ranges determined for the two serum types in the earlier study [128]. Unlike existing detection methods, our assay required neither RNA extraction nor target-amplification steps, leading to simple and direct quantification of targets in serum without the need for data normalization using external control measurements or primer optimization [207]. Furthermore, our method required only 25 μL of unprocessed serum for each assay. By comparison, microarray techniques that profile without target-amplification typically use 1 mL of serum to generate enough RNA extract for assay [206].

5.6 Data Analysis

Because target binding occurred predominantly on the surface of the gel particles, we acquired fluorescence images of the top and bottom main faces of each of the tablet-shaped particles (250 × 70 × 35 μm) for data analysis. For fluorescence integration, we used custom-written ImageJ macros and MATLAB scripts to process and analyze images. Following image alignment and cropping, signal intensity was summed pixel-by-pixel over the probe region for each face of a particle, and then the two resulting values were averaged to give a raw net value. For preliminary trials and calibration experiments, signal was also acquired in the same manner from a group of control particles (incubated in the same conditions but without spiked target). For each particle type, the mean signal from five of these control particles was then subtracted from each raw net value to obtain background-subtracted values for the integration analysis. Reported integration values in Figure 5.4 represent the mean of at least five particles. For spot-counting, a separate custom-written MATLAB script was used to process images. This script utilized a spatial bandpass filter and a local optimization algorithm (bpass.m and pkfnd.m, respectively; publicly available from http://physics.georgetown.edu/matlab/code.html) to automatically locate and count the number of RCA spots on each particle face. "Total spot count" refers to the sum from the two faces, and spot-counting values reported in Figure 5.4 and Figure 5.5 represent the mean of at least five particles. To estimate the limits of the spot-counting method, we calculated the probability of two probes with captured target being so close to one another that optical detection cannot resolve them. Assuming a resolution of λ/(numerical aperture) ~ 1 μm for our optical detection system, the probability that a second binding event will fall within a distance that is not resolvable from a single existing binding event is:

Area of Non-resolvability/Area of Probe Region = $[(\pi)(1\ \mu m/2)^2]/[(70\ \mu m)(45\ \mu m)] = 0.025\%$

This indicates that it is statistically unlikely for two single-molecule reporting events to overlap within the probe region of the particle. Although we chose 1 amol as the target amount at which to switch from spot-counting to integration for quantification, it should be possible to continue to spot-count for higher amounts without the risk of significant rates of overlap. In addition, better resolution could be obtained in future work by using an objective with a higher magnification and a greater numerical aperture.

In the discussion of reproducibility, "inter-run" refers to variability over different detection trials (*i.e.*, among groups of particles in different reaction volumes), while "intra-run" refers to variability within a single detection trial (*i.e.*, among the group of particles within one reaction volume). For the calculation of the LOD of each target, the intra-trial standard deviation of the 0 zmol (control) spot count was multiplied by three and added to the mean control spot count to determine a threshold count (corresponding to the signal-to-noise ratio of three frequently used in the field [205]). A linear regression was performed on the 0, 50, and 100 zmol spot-count results for each target, and the target amount at which the extrapolated curve passed through the threshold was taken to be the LOD. The LODs (in terms of molar amount, copy number, and molar concentration) are provided in Table 5.3. It is important to note that all incubation volumes in this study were 50 µL.

	Molar Amount	Copy Number	Molar Concentration
miR-141	15 zmol	9,000 copies	300 aM
miR-210	37 zmol	22,000 copies	740 aM
miR-221	31 zmol	19,000 copies	620 aM

Table 5.3: *Limits of detection for RCA-based detection on gel microparticles.*

We have demonstrated the RCA of a universal adapter sequence selectively ligated to targets captured on encoded gel microparticles for the ultrasensitive, multiplexed profiling of miRNA (Figure 5.6). We have developed an optimized protocol that allows for the highly specific detection of sub-femtomolar miRNA target concentrations in complex media, thereby expanding the dynamic range of the particle platform to over six orders of magnitude (300 aM to 40 pM) and introducing the possibility of direct single-cell profiling [204, 205]. Our ability to assay directly in minute amounts of readily-accessible biological media could potentially be leveraged for the creation of rapid, non-invasive diagnostic tests for the profiling of focused panels of miRNAs. The incorporation of fluorescent nucleotides for reporting binding events could streamline future iterations of the assay and simplify workflow [220], while the implementation of branched RCA could be explored for digital quantification [221-224]. It should also be straightforward to adapt the RCA scheme to a recent protein sandwich protocol developed for cytokine quantification on gel particles, enabling the quantification of low-abundance miRNA and proteins in the same assay and perhaps even on the same particle [175, 214].

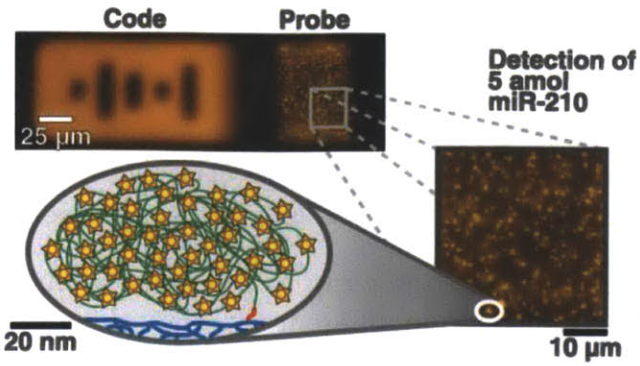

Figure 5.6: *Schematic of the three primary length scales involved in the RCA procedure.*

Chapter 6

MicroRNA Analysis in Raw Cellular Lysate

In the development of biological assays, improvements in detection sensitivity allow the use of smaller sample inputs, thereby reducing the technical and physiological burden of sample collection while also enabling more targeted analysis of specific sample subdomains (*i.e.*, tissue isolated from a particular region of a tumor). The ultimate goal for many bioanalytical researchers is a flexible and scalable analysis system that is capable of interrogating the molecular profiles of individual cells. While the miRNA detection performance we have demonstrated in previous chapters is superior to existing direct detection schemes, the LODs we have achieved are not suitable for the robust, multiplexed miRNA profiling of single cells. In this chapter, we describe the development of techniques for the miRNA analysis of individual cells and small groups of cells using hydrogel microparticles and arrays of PDMS microwells.

6.1 Introduction

The ability to directly measure miRNA from single cells is of great interest to the biological community. Evidence continues to mount that miRNAs are less susceptible to temporal fluctuations than mRNAs due to their stability and association with RISCs, making them ideal candidates for biomarkers of single-cell state and for stratifying cell populations [225, 226]. Although there are a number of technologies available for the profiling of mRNA transcripts and proteins from individual cells, there has been a noticeable lack of progress in adapting the same methods for the analysis of miRNAs [92, 99, 109, 227-229]. The copy

number of a given mature miRNA sequence depends primarily on cell type and state, with values as high as 500,000 per cell and as low as 10s per cell. Reliance on population-averaged measurements of miRNA levels prevents the interrogation of cell-to-cell expression heterogeneity, which can potentially be used to identify cell subtypes that respond to external stimuli in notable ways [230]. Techniques that require large inputs of cells also preclude the study of miRNA-mRNA correlations in rare cell types such as circulating tumor cells and embryonic cells. MicroRNA analysis on a single-cell basis allows for targeted profiling that cannot be skewed by the presence of other unknown or poorly understood cell types. The ideal system for this analysis would enable the rapid measurement of multiple miRNA levels in hundreds to thousands of cells in a single trial without the need for cumbersome sample preparation steps, RNA extraction, or target amplification. An optimal scheme would provide quantitative results from an input of crude cellular lysate with an efficient "one-pot" workflow that avoids the transfer or dilution of sample through multiple processing steps or modules.

An important consideration in transitioning from bulk to single-cell miRNA assays is the method by which the target molecules will be isolated and conditioned for capture. Unlike protein targets which are often actively secreted from cells, mature miRNAs are predominantly found complexed with carrier proteins within the cell, requiring careful yet thorough disruption of the cellular environment to facilitate binding to complementary probes. As RNA extraction at this scale is inefficient and technically challenging, the most practical analysis approach involves cell lysis (typically through heat shock or chemical treatment) and direct interrogation of the crude product. Several single-cell studies of miRNA content have been performed in this way with modified stem-loop RT-qPCR methods, but the majority are not amenable to high-throughput processing due to the need for manual handling and manipulation of individual cells with pulled capillaries prior to the lysis step [140, 141, 225]. The notable exception is the microfluidic approach introduced recently by White *et al.* in which ~300 cells can be analyzed in a highly-multiplexed fashion in a single run [226]. While this work represents a leap forward in single-cell miRNA analysis, it relies on a target amplification scheme within a relatively complex microfluidic network that may be difficult to scale-up cost-effectively in future applications. In addition, PCR reaction efficiency is highly sensitive to lysate concentration in the nanoliter chambers used and thus must be closely controlled and optimized for accurate results. It should also be noted that there has been some progress in the development of fluorescence *in situ* hybridization (FISH) for miRNA detection, but the protocol for this method requires multiple days of processing and is severely constrained in multiplexing capacity [231].

In this chapter, we present a suite of methods that moves our gel particle platform closer to a regime in which multiple miRNA targets can be measured directly (without target amplification) from hundreds to possibly thousands of individual cells with a simple workflow. Our strategy focuses on localizing probe-bearing particles and cells to nanoliter-sized PDMS wells for highly efficient capture of miRNA targets that have been liberated from cells and carrier proteins using detergent-based chemical lysis and protein digestion.

6.2 MicroRNA Detection in Lysate Produced from Collections of Cells

The vast majority of methods for miRNA quantification in tissue, cultured cells, blood, and serum first require the isolation of total RNA from the sample. In the case of PCR-based detection, this step is required to remove proteins and other entities that may interfere with the activity of the polymerase used for reverse transcription. In direct detection schemes that do not employ such enzymes, this purification is carried out to reduce the complexity of the input mixture so that subsequent incubation with probe-coupled substrates such as particles or microarrays will not lead to fouling. The ability to detect miRNAs in crude cellular lysate without a total RNA extraction procedure greatly simplifies workflow and allows for more direct quantification without the need to consider extraction efficiency.

6.2.1 Buffer Optimization and Analysis of HeLa Cells

Encoded hydrogel microparticles synthesized from PEG-based monomers and functionalized with capture probes are well-suited for direct miRNA profiling in complex mixtures due to their high sensitivity, high specificity, and resistance to non-specific adsorption of biological molecules. To investigate the compatibility of the particles with crude lysate inputs, we modified our assay protocol and carried out a series of experiments to gauge the effect of adding detergent, protease, and RNase inhibitor to our hybridization buffer. As described in Section 2.3.9 and Section 2.3.10, we added freshly trypsinized and washed HeLa cells to reaction tubes containing gel particles as well as various amounts of SDS and proteinase K (PK). These additional buffer agents were employed to disrupt the cellular membrane and to denature and digest undesirable protein content that could potentially sequester miRNA targets.

In initial trials with particles bearing probe for let-7a, ~2,000 HeLa cells were spiked into each reaction, and a small yet consistent signal was observed in the probe region of the particles after 90 min of lysis/target capture at 55°C in a reaction buffer of TET with 350 mM NaCl. Depending on buffer conditions, signal intensity was comparable to that observed for synthetic let-7a spikes of ~5–30 amol. Importantly, combining the lysis and capture steps did not lead to non-specific adsorption or fouling of the gel particles. In the concentration range of 0.5–4% SDS (w/v), it was observed that raising SDS levels (at a fixed concentration of PK, 200 μg/mL) led to an increase in target capture, although the difference between 2% and 4% was only slight (Figure 6.1 A). At SDS levels greater than 4%, signal was seen to be lower than that obtained with 2% and 4% SDS. Seeking to investigate possible benefits from heat shock, we subjected a sample to a 95°C preheat for 5 min prior to particle addition but only observed a slight increase in target capture compared to a sample with the same amount of SDS and PK (Figure 6.1 B). This contrasts sharply with assays in 25 μL unprocessed serum in which a preheat step was crucial for denaturing background proteins and for minimizing non-specific binding to the gel particles [232]. Furthermore, it was observed that levels of PK higher than 200 μg/mL led to loss of

signal, presumably from the introduction of higher amounts of the glycerol-based buffer in which the enzyme was stored (Figure 6.1 B). There seemed to be no additional benefit from introducing RNase inhibitor to the reaction mixture, with lower signals observed for 0.2 U (4 U/mL in final reaction mixture) and 20 U (400 U/mL) additions than for the case in which inhibitor was not used (Figure 6.1 C). To explore the effect of blocking agent in the washing solution used to prepare the cells for assay, we carried out a cell preparation without BSA (normally at 0.1% (w/v) in cell wash buffer). This test resulted in a lower signal than preparations with BSA (Figure 6.1 D), underscoring the importance of using BSA to block tubes and pipette tips in the cell washing process. It was postulated that failure to block led to undesirable cell adsorption and loss on tube and tip surfaces, an effect also seen in preliminary work with cell encapsulation studies (Section 6.4).

Additional trials with 600 amol of synthetic let-7a RNA target further elucidated the effects of adding SDS and PK. As Figure 6.2 demonstrates, there was only a small decrease in capture and labeling efficiency when using detergent and protease at levels suggested by the initial trials. Moreover, the increased complexity of the buffer did not affect reproducibility, with intra-trial coefficients of variation (CVs) of only 3–4% for buffers containing both SDS and PK. These results indicated that the lysis buffer components were effectively washed out of the gel particles prior to the addition of T4 DNA ligase for labeling. From these experiments, it was determined that subsequent assays would employ 2% SDS and 200 μg/mL PK to maximize target capture and labeling efficiency. With the signal generated by the 600-amol synthetic let-7a RNA spike in 2% SDS and 200 μg/mL PK, it was estimated that the fluorescence previously observed for the assay of 2,000 HeLa cells in the same buffer corresponded to ~30 amol of endogenous target, implying a let-7a copy number of ~9,000 per HeLa cell. This figure is in rough agreement with a previously published estimate that quantified miRNA expression using a modified Invader assay (4,200 per HeLa cell, Allawi *et al.* [233]).

Trials with 600-amol additions of synthetic miSpike sequence into reaction mixtures containing 2,000 HeLa cells and the optimal lysis buffer showed ~105% recovery efficiency of the spiked target when compared with the same conditions but without cell inputs. This result indicated that the presence of the raw lysate did not significantly interfere with the binding conditions required for sensitive miRNA detection, although it should be noted that the miSpike was not initially sequestered in protein complexes as endogenous miRNA targets would be.

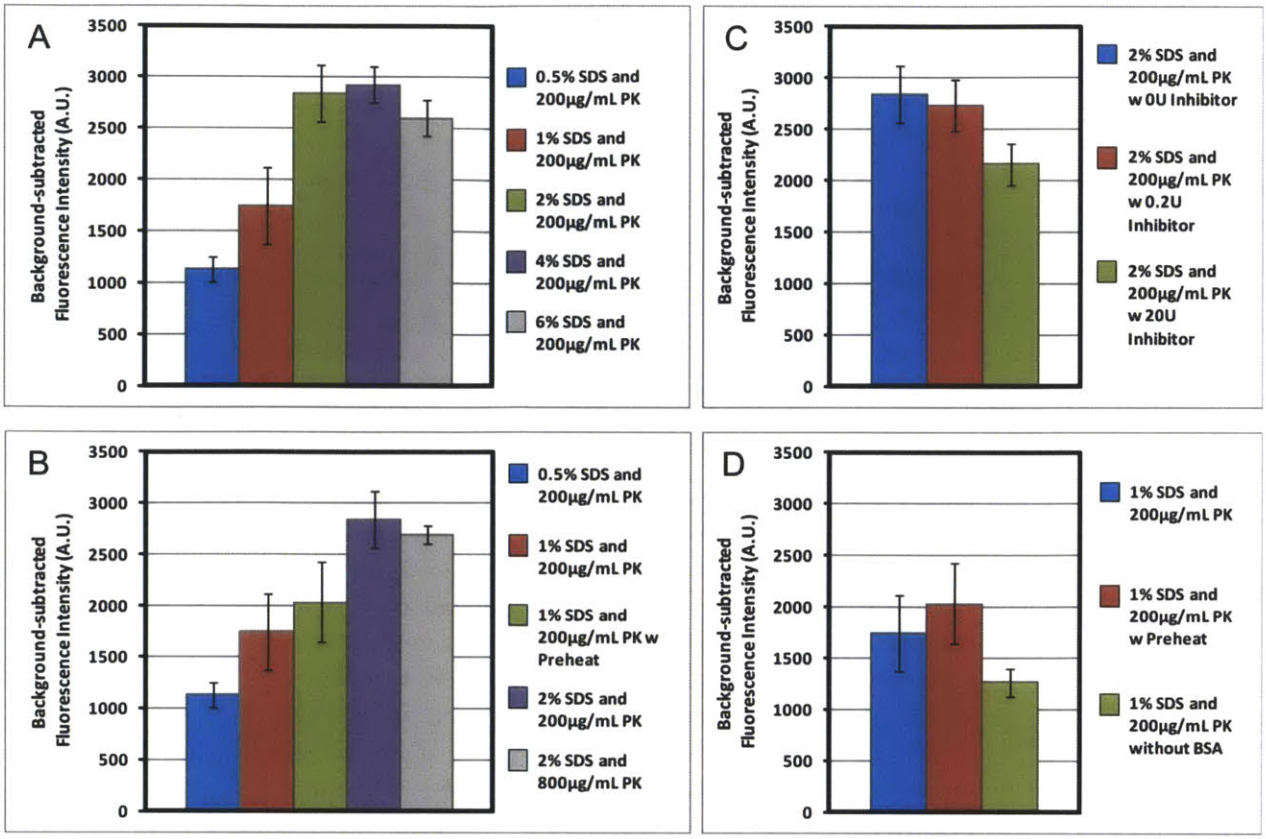

Figure 6.1: *Parametric study of buffer and operating conditions on let-7a detection in raw HeLa lysate. For each condition, ~2,000 HeLa cells were injected into the reaction mixture prior to incubation. (A) For a fixed concentration of proteinase K (PK), target capture increased with increasing SDS concentration up to 4% (w/v). (B) Preheating the reaction mix and cells to 95°C for 5 min prior to particle introduction provided only a small boost in signal, while raising the PK concentration from 200 to 800 µg/mL led to a slight decrease. (C) There was no noticeable benefit from the use of an RNase Inhibitor (RNaseOUT, Invitrogen), with signal actually decreasing at higher levels of inhibitor. (D) The exclusion of BSA from the buffer used to dilute and wash the cells led to lower signal, presumably due to the loss of cells from sticking to tubes and pipette tip surfaces during manipulation. All reactions were run at 55°C for 90 min with 350 mM NaCl, and particles were labeled using the standard non-RCA ligation/reporter protocol. Each measurement represents the mean of 4–7 particles; error bars represent standard deviation. Background measurements were taken from particles incubated in buffer with 350 mM NaCl, 2% SDS, and 200 µg/mL PK without cells.*

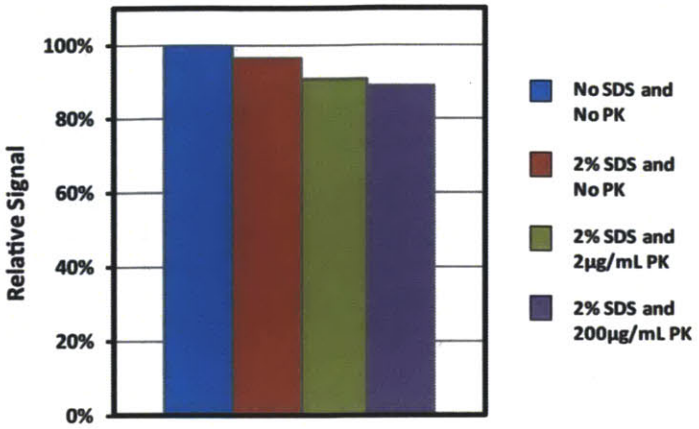

Figure 6.2: *Effect of buffer composition on the detection of synthetic let-7a RNA target. Particles bearing a let-7a probe region were incubated with 600 amol of synthetic let-7a RNA for 90 minutes at 55°C with varying amounts of SDS and PK. Particles were labeled using the standard non-RCA ligation/reporter protocol. Probe region fluorescence was background-subtracted, integrated, and scaled using the let-7a fluorescence signal for particles incubated without SDS and without PK. Each measurement represents the mean of 4–6 particles. Background measurements were taken from particles incubated in buffer with 350 mM NaCl, 2% SDS, and 200 µg/mL PK without target.*

Throughout the lysis buffer trials, the background exhibited by "negative control" particles (for which there was no expected target present) was seen not to vary noticeably with changes in SDS, PK, or inhibitor. Thus, for simplicity, the background measurements used to analyze the experimental data in Figure 6.1 and Figure 6.2 were taken from let-7a particles in the most frequently used lysis buffer: TET with 350 mM NaCl, 2% SDS, and 200 µg/mL PK without cells. Furthermore, a brief investigation of running the lysis/capture step for 150 min (as opposed to the normal 90 min) yielded only a slightly higher signal, and as a result, incubations were kept at 90 min to streamline workflow. The parametric study presented here was conducted with a fixed cell input amount of ~2,000 HeLa cells. In future work it may be necessary to adjust detergent or protease concentration to accommodate the lysing of more cells. The data included in this section provides a basis for predicting how the addition of more SDS or PK will affect the target capture and labeling processes.

6.2.2 Modified RCA for Labeling in Lysis Buffers

While there was little difficulty in adapting the non-amplified, ligation-based labeling approach to protocols with SDS/PK-based lysis buffers, it was found that the RCA process

could not as easily be ported onto the new workflow designed for direct detection in lysate. Specifically, it was observed that exposure to buffers containing SDS and PK led to subsequent fouling of all regions of the gel particles during the use of RCA. We postulated that this fouling arose from the non-specific clumping of the biotinylated oligonucleotides used for labeling the long DNA concatemers. Seeking other methods of introducing fluorophores to the concatemers, we began to use modified nucleotides in the RCA process that were conjugated to either biotin or Alexa dye. Incorporation efficiency for modified nucleotides depends on polymerase type, modification type, and the relative concentration of modified and unmodified nucleotides. However, there is little known about how to rationally design a system around these factors. As a result, reagents and conditions seen to work in previous studies were first systematically evaluated in neat buffers (no SDS or PK) to test compatibility with the gel particles. Initial work with the Phi29 enzyme and an Alexa-488-labeled dUTP (ChromaTide® Alexa Fluor® 488-5-dUTP) at concentrations of 25–50 μM failed to produce signal for 4-h RCA extension times in assays spiked with 10 amol of miRNA target. In addition, there was significant fouling of particles, even in neat buffers not containing SDS and PK.

In the next experiment, a commercially available biotinylated nucleotide mixture (1 mM dCTP, dGTP, dTTP, 0.84 mM dATP, 0.16 mM biotin-14-dATP with biotin attached at the 6-position of the purine base with 14-atom spacer, New England Biolabs) was tested with the same extension time and target amount. The addition of 5 μL of this mixture to the RCA reaction produced less fouling than the oligonucleotide labeling method, but again, there was no noticeable signal, even with RCA temperature adjustments (30–37°C) and the use of DMSO (15% (v/v), incubation at 37°C for 1 h) to denature concatemers for more efficient labeling with SA-PE. A second attempt with this nucleotide mixture and the vendor-recommended reaction buffer for Phi29 (with an additional 200 μg/mL BSA to reduce non-specific binding of debris to particles) produced a low signal (~15% of that seen for complementary oligo labeling method) for a 10-amol target spike and a 4-h RCA at 30°C. Further attempts to denature the concatemers with urea treatments for more efficient SA-PE binding to modified nucleotides [220] yielded little improvement in signal but eliminated nearly all remaining non-specific binding. These results suggested that incorporation of the biotinylated nucleotides was occurring, although at a very low rate.

Seeking to increase the number of biotinylated nucleotides in each concatemer, we began to run the RCA reaction overnight (14 h) at 30°C in our gel-customized RCA buffer. In addition, a new nucleotide mixture was created by combining unmodified nucleotides (New England Biolabs), biotin-14-dATP (Invitrogen), and biotin-14-dCTP (biotin attached at the N4-position of the pyrimidine base with 14-atom linker, Invitrogen). This approach provided two different biotinylated nucleotides for more efficient labeling. Various input amounts of the dNTP master mix described in Section 2.3.9 were tested in the RCA mixture, with 1 μL providing the lowest fluorescent background while still providing sufficient signal intensity for spot discrimination (Figure 6.3). Further tests indicated that the post-RCA addition of 5 μL of a urea/TET mixture (30% (v/v) 6 M urea in TET and 70%

R50) and incubation at 37°C for 1 h greatly reduced fouling tendencies when compared with 5 µL of 6M urea treatments used previously. It was also observed that filtering the urea/R50 mixture as well as the SDS/PK lysis buffer improved assay results by reducing the amount of debris in the reaction volume. The final optimized protocol described in Section 2.3.9 provided the ability to carry out RCA in complex lysis mixtures that featured both SDS and PK, a crucial achievement for the application of this signal amplification scheme in assays featuring crude lysate inputs. Although the intensity of the RCA spots was not as high as that seen with the complementary oligo labeling approach, there was still sufficient signal to discriminate individual binding events, allowing for single-molecule reporting resolution.

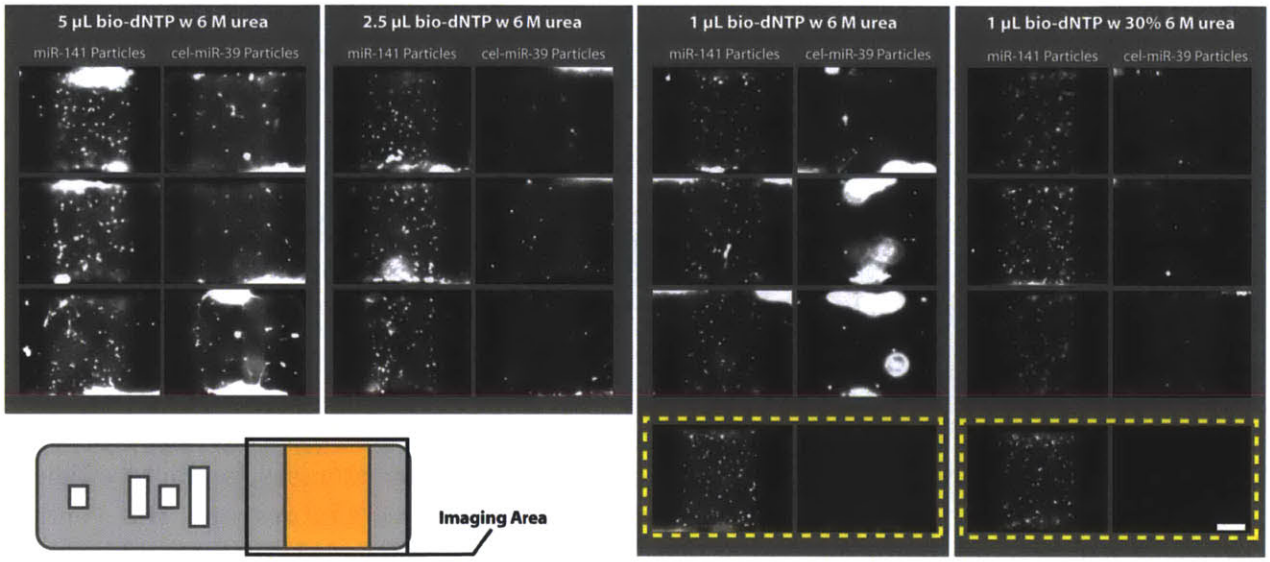

Figure 6.3: *Images of probe regions of miR-141 and cel-miR-39 particles following assay in lysis buffer containing 2% SDS, 200 µg/mL PK, 1 amol miR-141, and 0 amol cel-miR-39. The lowest background and cleanest particles were obtained when using 1 µL of biotinylated dNTP master mix and a 30% 6M urea/70% R50 treatment following RCA. Volume of bio-dNTP represents amount of master mix added to reaction tube prior to RCA. Images in yellow boxes were taken from assays with incubation buffers that did not contain SDS or PK. Scale bar in bottom-right image is 15 µm.*

6.3 Well-based Approaches for Single-cell Analysis

The development of an effective lysis buffer and a compatible high-sensitivity labeling scheme enabled us to investigate new cell-based detection schemes that previously would not have been possible. While earlier detection trials with the gel particles were carried out in 50-µL reaction volumes contained within snap-top tubes, it was postulated that capture efficiency could be greatly augmented with the lysis of cells in small volumes [102, 234]. Prior to lysis, the miRNA content within a cell is relatively concentrated, and the release of that content into a nanoliter-scale volume would lead to a much higher effective target concentration than would be achieved with release into a 50-µL reaction volume. We sought

to leverage our ability to capture and lyse in a single reaction step to generate a microwell-based "confinement assay" in which particles and cells are co-localized to nanoliter-scale volumes for detection. This approach allows us to significantly reduce the scale of the input required for analysis, potentially enabling the direct detection of miRNA from lysate generated from individual cells.

Single-layer SU-8 master wafers were created at the BMRC for the production of PDMS-based well substrates. In the confinement assay protocol, probe-laden gel particles and target input (either cells or appropriately diluted synthetic RNA spikes) were deposited onto the face of the PDMS slab featuring relief-generated features, at which point the wells could be sealed off from one another by placing a glass slide on top of the PDMS (Figure 6.4 and Section 2.3.10). Particles could be inserted into wells either by (1) a gradual settling/sifting process or, in the case of magnetically functionalized particles, by (2) using a hand magnet to rapidly rotate and translate particles into the wells [179]. For the trials described in this section, wetting and lysis buffers were supplemented with 1% (w/v) BSA to minimize the undesirable adhesion of biomolecules to well surfaces. Superase-In RNase inhibitor was also added to the deposition droplet (final concentration of 0.5 U/μL) to prevent degradation of RNA. As discussed in Section 2.3.10 and Section 7.1, it was observed that intense plasma treatment of the PDMS substrates (to increase substrate hydrophilicity and thereby aid in the spread of aqueous deposition buffers) led to strong binding between the gel particles and the PDMS surfaces, preventing the harvesting of the particles from the microwells after assay. As a result, only mild plasma treatments were employed, a protocol requirement which hindered the wetting process and prevented the use of the full complement of wells on each PDMS substrate.

Table 6.1 summarizes the dimensions and volumes investigated for the confinement assay. It was found that the particles and cells were retained with much higher efficiencies during the mixing and sealing procedures when using the deeper set of wells (113 μm in height). To minimize the reaction volume, it was desirable to use the smallest wells possible. Wells 3a and 3b proved too small to fill efficiently with the standard 250 × 70 μm gel particles even when using magnetic manipulation. Wells 1a, 1b, 2a, and 2b were large enough to fill using both particle addition methods, though the filling of the smaller 2a and 2b wells was much less efficient with the settling process than with magnetic manipulation. It was decided that subsequent studies would focus on well type 2b (300 × 100 × 113 μm, 3.4 nL), which provided the best overall balance of particle retention, filling efficiency, and volume characteristics.

In order to confirm that the wells were fully sealed by the application of the cover glass and insertion into the screw-clamp hybridization chamber, an experiment was performed in which gel particles bearing photocleavable Cy3 fluorescent groups were sealed within the wells and then exposed to UV light to release the reporters [237]. Because the hybridization chamber covers the wells, it was necessary to expose the wells and cleave the Cy3 groups after the full incubation had been performed and after the glass-PDMS-glass construct had

been removed from the chamber. As a result, the test could only provide information on the sealing status at the end of the 90 min, 55°C incubation. Figure 6.5 demonstrates that the cleaved fluorescent groups were retained within the bounds of the PDMS well and thus the wells were fully sealed by the end of the incubation.

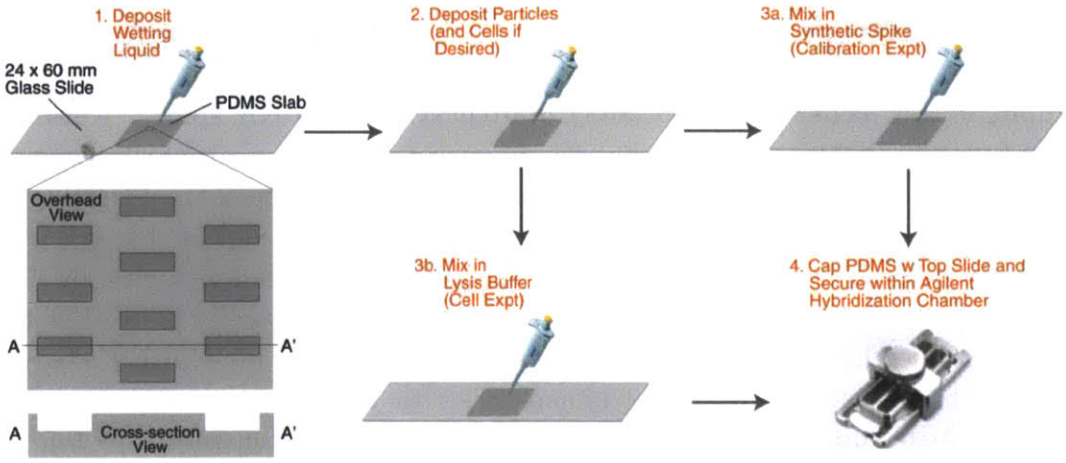

Figure 6.4: *Workflow of well loading for confinement assay. PDMS well height was dictated by the feature height on the corresponding master wafer. After depositing a wetting liquid and allowing the wells to fill, particles (and cells if desired) were deposited in a TET-based buffer without SDS or PK. For calibration experiments, synthetic targets were diluted in lysis buffer and manually mixed into the deposited droplet with a pipette to ensure even dispersion. For cell experiments, pure lysis buffer was mixed into the droplet. In both cases, wells were immediately sealed with a cover slide following manual mixing to prevent mass transport between microwells. Pipette and hybridization chamber images adapted from [235] and [236], respectively.*

The sealing confirmation allowed us to then explore the detection performance of well-immobilized gel particles. After depositing particles into wells, a lysis buffer containing appropriately diluted synthetic RNA targets was manually mixed into the deposition droplet and particles were immediately sealed and incubated at 55°C for 90 min (Figure 6.4 and Section 2.3.10). Next, particles were extracted from wells, deposited in R50 contained within snap-top tubes, and labeled with the standard protocols described in Section 2.3.4 and Section 2.3.5. To estimate target amount within each well, the concentration of synthetic target within the deposition droplet was multiplied by the well volume (3.4 nL for well type 2b). It should be noted that this calculation neglects the volume displaced by the hydrated gel particle and thus likely represents an overestimate of target amount (*i.e.*, actual target amounts within each well were most likely lower than those quoted). Magnetically-functionalized, shape-encoded particles bearing four distinct probe types were used for this study to simplify particle loading and to maximize the amount of data that could be collected in each experiment [179]. During particle synthesis, each of the probe types was loaded into its respective 20% PEG-DA prepolymer solution at a concentration of

250 μM, providing an eventual particle concentration of ~25 μM (assuming ~10% incorporation efficiency [174, 180]). In a typical experiment, ten magnetic particles could be loaded into type 2b wells in under 2 min using a hand magnet. Figure 6.6 illustrates the relative dimensions of the particle and well and also demonstrates the relative signal intensity observed for separate 500-amol spikes of each of the four target types in typical snap-top tube experiments with 50-μL incubation volumes.

	Length (μm)	Width (μm)	Height (μm)	Volume (nL)
Well 1a	500	500	46	11.5
Well 1b	500	500	113	28.3
Well 2a	300	100	46	1.4
Well 2b	300	100	113	3.4
Well 3a	275	80	46	1.0
Well 3b	275	80	113	2.5

Table 6.1: *Dimensions and volumes of microwells investigated for confinement assays.*

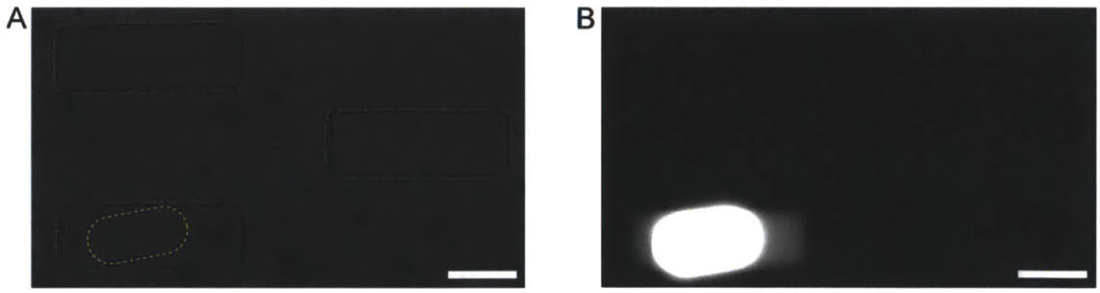

Figure 6.5: *Results of well-sealing test. (A) Brightfield image of gel particle (outlined in yellow) in 300 × 100 × 113 μm well after incubation at 55°C for 90 min but before cover glass had been removed. Particle was irradiated with UV light for 5 min. (B) Fluorescent image of gel particle 15 min after UV irradiation. The cleaved Cy3 groups have diffused away from their particle source but seem to have been retained within the bounds of the PDMS well, indicating that wells have indeed been effectively sealed. It should be noted that the cleaving wavelength was sufficiently different from the fluorescence excitation wavelength to avoid photobleaching. Scale bars are 100 μm.*

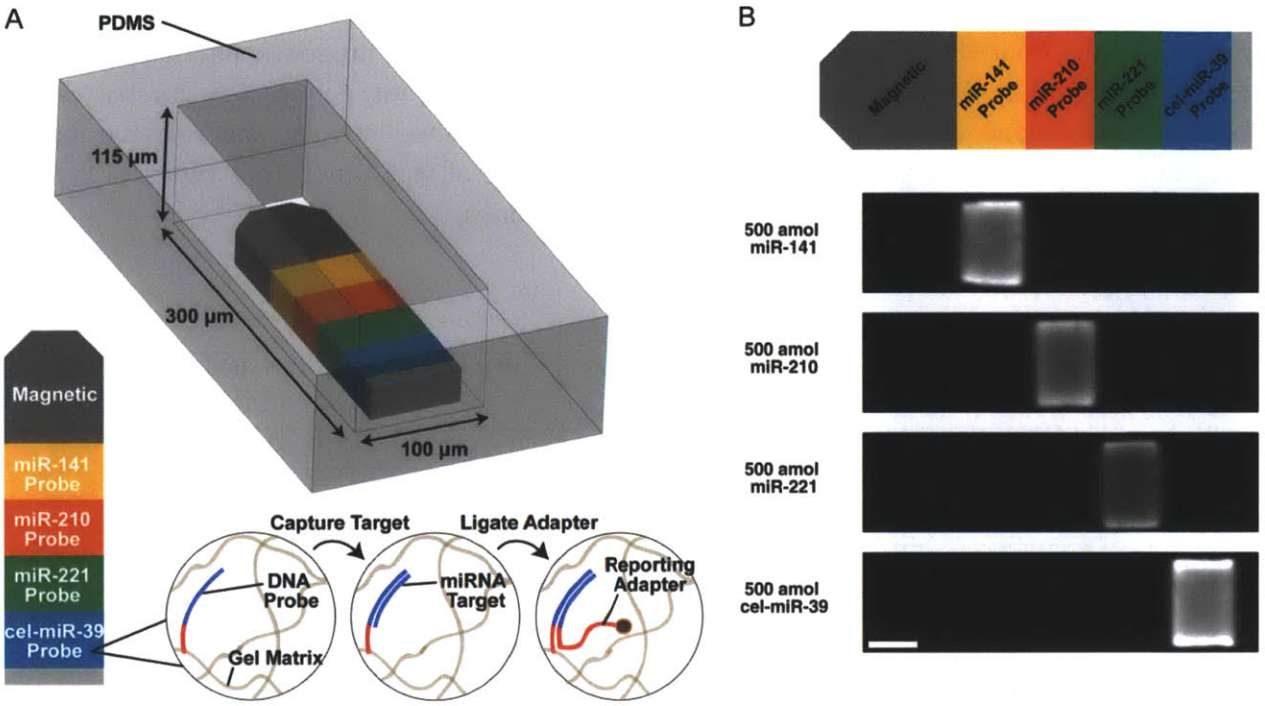

Figure 6.6: *Magnetic particle scheme for well-based assays. (A) Depiction of 4-probe magnetic particle (250 × 70 × 30 µm) in PDMS microwell. Each probe region was embedded with a DNA probe bearing a miRNA-specific region (blue) and a universal adapter region (red). (B) Fluorescence images of magnetic particles incubated with 500 amol of the indicated RNA target in a 50-µL reaction volume. Scale bar in B is 30 µm.*

The detection performance of gel particles in SDS/PK lysis buffers in the confinement assay is summarized in Figure 6.7. As shown in Figure 6.7 B, fluorescent signal with the non-amplified labeling scheme scaled with input amount for the simultaneous spike of four different sub-attomole amounts of the four RNA targets of interest. Significantly, the fluorescence from a 60-zmol spike of miR-141 was easily distinguished without the need for signal amplification. By comparison, the LOD for RCA-based labeling in 50-µL incubation volumes was previously determined to be 15 zmol. A further test with the bio-dNTP RCA scheme showed strong signal from a 50-zmol cel-miR-39 spike and faint signal from a 10-zmol miR-210 spike that seemed to be above the background registered on the neighboring "control" regions (Figure 6.7 C). To assess the well-to-well variation within a given trial, 250 zmol and 500 zmol of miR-141 and miR-221, respectively, were spiked into the wells, and the fluorescence intensities of six well-immobilized particles were examined (Figure 6.7 D). Upon integration of the background-subtracted fluorescence from each probe region, the intra-trial CVs were calculated to be 15% and 13% for the 250- and 500-zmol spikes, respectively. This result indicated that spiked target was being evenly distributed to the wells through the manual pipette-mixing process. For the RNA targets with the greatest binding rates (miR-141 and cel-miR-39), it was roughly estimated from these trials that the

confinement assay LOD was ~10 zmol (~6,000 molecules) for the non-amplified scheme and ~0.5 zmol (~300 molecules) for the RCA-based scheme.

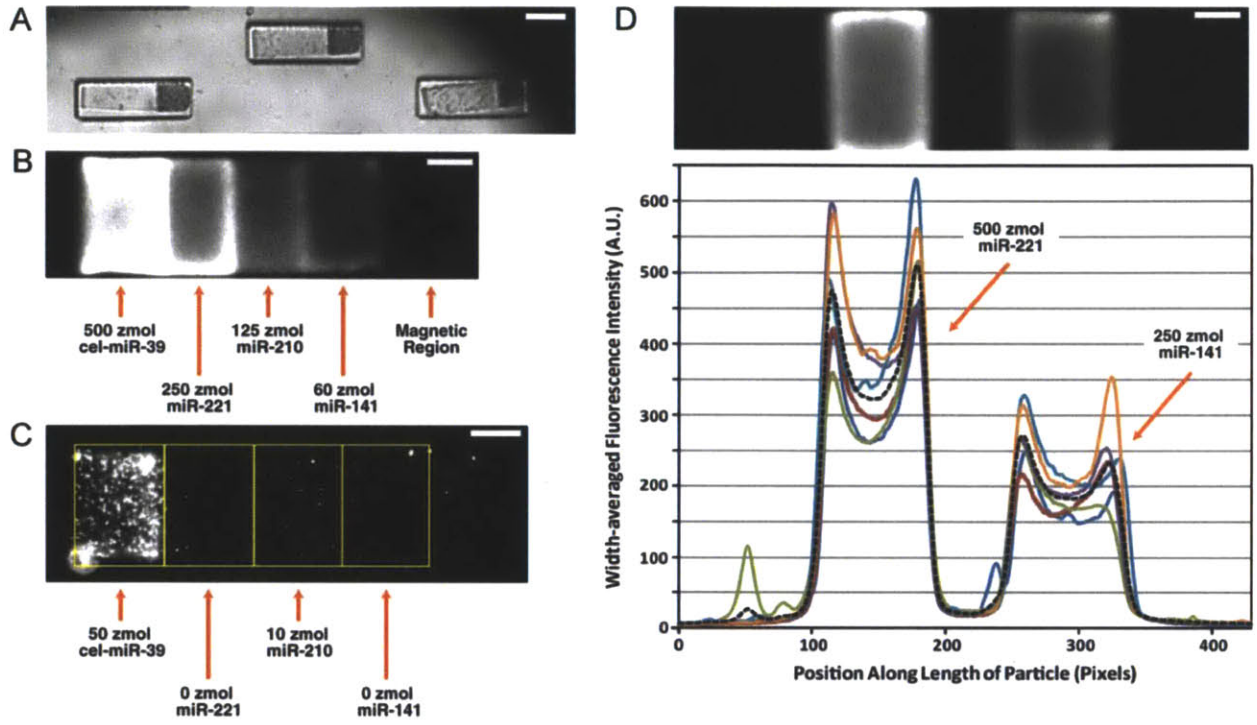

Figure 6.7: *Detection of synthetic RNA targets with magnetically functionalized gel particles (250 × 70 × 30 μm) and the confinement assay. (A) Image of 4-probe magnetic particles after well loading with hand magnet. (B) Fluorescence image of particle incubated within well with the indicated target amounts and then labeled using the non-amplified scheme. (C) Fluorescence image of particle incubated within well with the indicated target amounts and then labeled using the bio-dNTP RCA scheme. (D) Fluorescence image and width-averaged intensity profiles for six particles incubated in six separate wells with 500 zmol miR-221 and 250 zmol miR-141. Dotted black curve represents mean profile. All experiments in this figure performed with type 2b wells and target capture incubations of 90 min at 55°C in lysis buffer containing 2% SDS, 1% BSA, and 200 μg/mL PK. Scale bars in A, B, C, and D are 100, 30, 30, and 25 μm, respectively.*

It is important to note that the binding patterns observed on the magnetic particles with the non-amplified labeling scheme differed slightly from those seen with earlier particle types. This was attributed to the fact that most of the probe region interfaces border other probe regions synthesized from 20% PEG-DA prepolymer and not from the normal 35% PEG-DA prepolymer that was used as an inert spacer chemistry in the majority of previous trials. This chemistry difference allows for more rapid diffusion of targets within the more porous gel and leads to increased binding on the internal interfaces between probe regions.

Next, the suitability of this scheme for HeLa cell analysis was investigated. HeLa cells were trypsinized, harvested, and stored at concentrations between 1 x 10^6 per mL and 6 x 10^6 per

mL in Dulbecco's Modified Eagle's Medium (DMEM) with 10% fetal bovine serum (FBS) prior to assay. As described in Section 2.3.10 and Figure 6.4, cells were diluted and then deposited onto the well surface along with gel particles bearing probe for miR-21, after which the lysis buffer was manually mixed into the deposition droplet with a pipette, the system was immediately closed with a glass slide, and the well setup was incubated within the hybridization chamber. Care was taken to always deposit cells and particles in solution with 150–350 mM NaCl to ensure cell viability and to avoid swelling of gel particles. In the event that the deposition buffer contained less than 350 mM NaCl, the lysis buffer was adjusted such that its addition to the deposition droplet produced a final NaCl concentration of 350 mM for efficient target capture [205]. Although the results presented here reflect experiments in which more than two cells were loaded into each well (Figure 6.8 A and Figure 6.8 B), it was possible to dilute the cell suspension such that addition to the well substrate produced roughly 1–2 cells in 50–75% of the microwells. This optimal dilution was approximately 7,000 cells per mL of deposition buffer. To measure the background associated with the target incubation step, additional "control" particles were incubated without cells in non-agitated 50-µL reaction mixtures in snap-top tubes in the same buffer and at the same temperature as used on the PDMS chip.

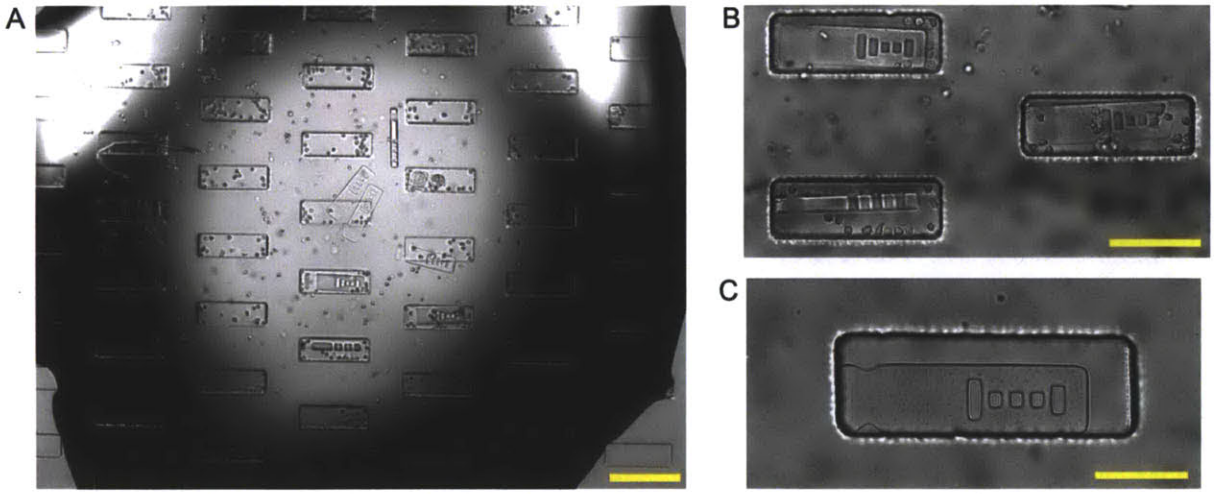

Figure 6.8: *Confinement assay with HeLa cells. (A) Image of deposition droplet containing HeLa cells and eight encoded gel particles (250 × 70 × 30 µm) bearing probe for miR-21. Cell density within wells can be tuned by adjusting the concentration of cells in deposition buffer. (B) Enlarged view of three particles co-localized with several HeLa cells within type 2b PDMS wells prior to the introduction of lysis buffer. (C) Gel particle after target incubation and removal of glass-PDMS-glass construct from hybridization chamber. Note that the particle has slightly contracted due to high incubation temperature (55°C) and that cells have been fully lysed. Scale bars (in yellow) in A, B, and C are 300, 150, and 100 µm, respectively.*

The absence of cells upon removal of the PDMS from the chamber indicated that complete lysis had indeed occurred (Figure 6.8 C), and the majority of the particles were seen to be

hydrated and intact after incubation. Upon removal from the wells and insertion into snap-top tubes, cell-exposed particles were labeled with the non-amplified ligation scheme and analyzed with static fluorescence imaging; control particles were processed in an identical manner. Figure 6.9 summarizes the results obtained for miR-21 detection from small groups of HeLa cells incubated within wells in lysis buffer at 55°C for 90 min. The ability to localize and then lyse cells within a sealed, particle-occupied well produced noticeable miR-21 signal with inputs as small as 2–5 cells. Given an estimated copy number of 12,000 copies/cell for miR-21 in HeLa [238], this translates to approximately 40–100 zmol within the well upon lysis. Experiments with synthetic RNA targets showed this range to be within the limit of detection when using the non-amplified labeling scheme.

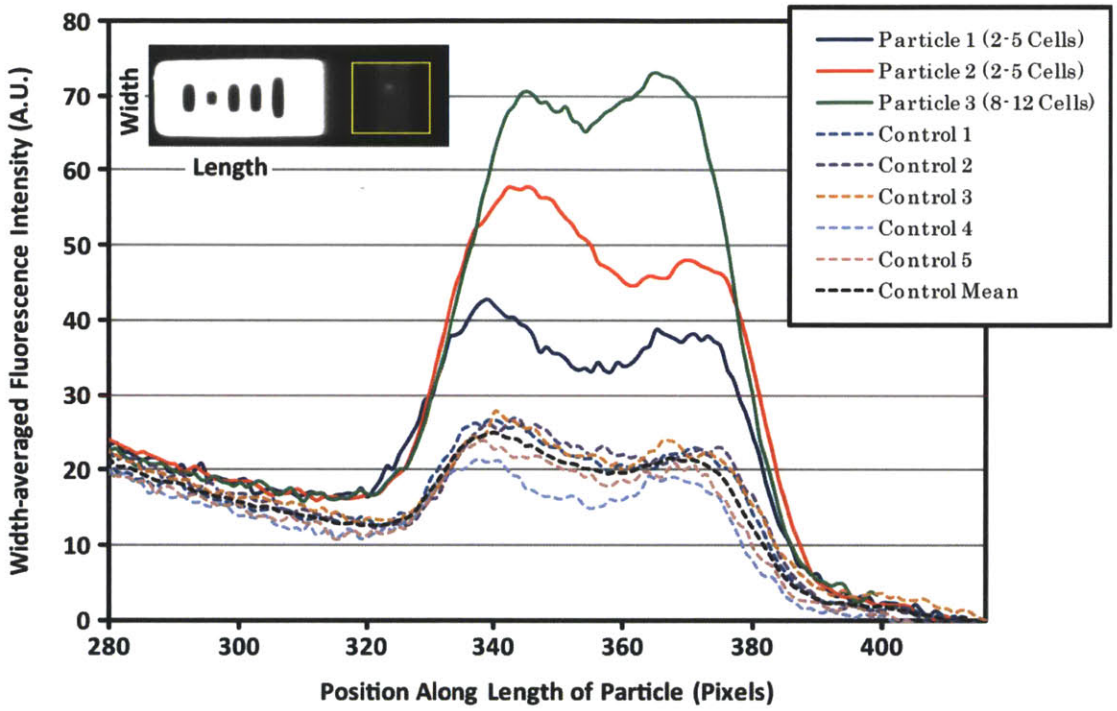

Figure 6.9: *Width-averaged fluorescence profiles of probe region of miR-21 particles in confinement assay. Solid curves represent particles incubated within a type 2b well with the indicated range of HeLa cells and lysis buffer. Dotted curves represent control particles incubated without cells in 50 μL of the same lysis buffer and at the same temperature. Yellow box over the image represents the area of analysis depicted in plots. Cell ranges rather than absolute numbers are provided for well occupancy due to the inability to correlate each analyzed particle's identity with original well condition. Each quoted range reflects the minimum and maximum number of cells in particle-occupied wells in a specific trial prior to well sealing. Particle width in image is 70 μm.*

Additional HeLa cell trials were run with longer lysis/capture times (2 h and 24 h) at 37°C (to prevent dehydration of the PDMS wells). Compared to the results in Figure 6.9, there was a slight signal reduction in the 2-h trial, while the 24-h trial was largely inconclusive

due to poor particle recovery (although wells remained hydrated throughout the long lysis/capture step). Overall, the cell-based confinement assays demonstrated the feasibility of directly detecting miRNA from small numbers of cells, an achievement which can be built upon with the application of RCA as well as the development of more efficient methods for particle and cell loading.

It should be noted that there were several limitations in the protocol that prevented the collection of larger quantities of data. For example, roughly 50% of the well-immobilized particles would leave the PDMS and become stuck to the top glass slide upon removal of the slide, requiring the soft gel particles to be scraped from the glass surface and thereby increasing the risk of particle deformation. Furthermore, for the use of non-magnetic gel particles, loading efficiency was not as high as that observed with the four-probe magnetic particles, and as a result, 20–40% of particles deposited onto the PDMS failed to enter wells and were crushed upon placement of the top glass slide. In future iterations of this procedure, it would be greatly beneficial to use only magnetic particles and to develop a chemical treatment or blocking process that prevents particles from sticking to the top glass slide.

6.4 Cell Encapsulation Strategies

It has previously been shown that cells can be encapsulated within hydrogel microparticles during the SFL procedure by suspending them within the prepolymer mixtures prior to the loading of the microfluidic synthesis device [163]. We sought to leverage this ability in order to explore the possibility of lysing cells within a probe-laden gel region for enhanced miRNA capture efficiency. Based on previous observations of the relative rates of reaction and diffusion of miRNAs, it was postulated that released targets would bind to surrounding DNA probes before diffusing out of the gel, allowing for highly efficient target capture. As described in Section 2.3.9, the SFL procedure was modified to allow for the high-throughput encapsulation of cultured HeLa cells within encoded gel particles. By optimizing cell loading density, BSA concentration, and channel design, it was possible to achieve stable synthesis at throughputs of 5 particles/s, with approximately 20–30% of particles containing a single cell encapsulated within a probe-laden region.

In initial trials, particles incorporated with cells and probe for let-7a were harvested from the SFL device, filtered to remove unincorporated cells, incubated for 90 min at 55°C with a lysis buffer (TET with 350 mM NaCl and 2% SDS), and fluorescently labeled with the non-amplified ligation scheme. The lysis of the cells within the gel produced noticeable cavities that could be used to determine cell position within the particles during signal analysis (Figure 6.10 A). For cell-laden particles exposed to lysis buffer containing SDS, a relatively strong fluorescent signal was observed in the vicinity of the cavity, typically with a semi-circular appearance that disappeared about 10 μm from the edge of the cavity (Figure 6.10 B). This fluorescent signal was seen to be strongly retarded by the less porous gel regions synthesized from inert monomer (35% PEG-DA) (Figure 6.10 C), suggesting that the

labeled entities were larger than discrete miRNA targets (which would be expected to rapidly diffuse through the gel produced from the inert monomer). Furthermore, in many instances, the fluorescence was not symmetric about the cavity but rather exhibited a tendency to appear towards the interior of the particle (Figure 6.10 D). Importantly, the fluorescent signal was not observed in trials in which SDS was omitted from the incubation buffer, indicating that the signal was being generated by the labeling of intracellular contents that had been spilled out of the cell and not from cellular autofluorescence. However, further tests in which particles were immobilized and lysed in gel regions bearing no probe also exhibited fluorescence, a result which showed our signal was not being generated by labeling of the intended target.

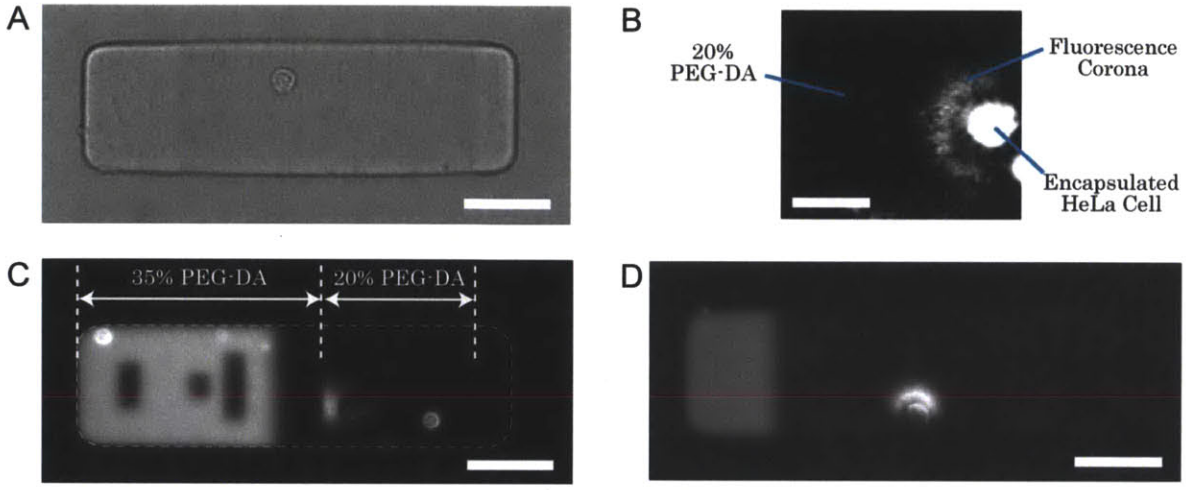

Figure 6.10: *Gel encapsulation of HeLa cells. (A) Image of the cavity left by a single cell within the gel particle after the lysis procedure. (B) Fluorescence image of the area surrounding a cavity after cell lysis and ligation labeling of lysis products. In this case, the PEG-DA gel is incorporated with DNA probe for let-7a. (C) Encoded gel particle with an encapsulated cell that was lysed and produced a spread of fluorescently-labeled material that was abruptly retarded by the particle's less porous 35% PEG-DA region. (D) Example of the the tendency for cells to lyse and spill fluorescently-labeled material towards the interior of the gel particle. Fluorescent signal on the left side of the particle is from Rh-Ac incorporated during synthesis to serve as an orientation marker. Scale bars in A, C, and D are 50 μm; scale bar in B is 20 μm.*

To determine the source of the fluorescent signal, we performed additional experiments that modulated the lysis buffer and labeling conditions in a knockout fashion (*i.e.*, one deviation from standard protocol per trial). No signal was observed when SA-PE was omitted from the protocol, nor was signal observed when only universal adapter was excluded in a separate trial. In a third trial, the exclusion of T4 DNA ligase produced the previously observed levels of cell-based fluorescence. Finally, a considerable reduction in fluorescent signal was seen when NaCl concentration within the lysis buffer was reduced

from 350 to 250 mM. Together, these results suggested that the fluorescent signal was arising from the salt-mediated, non-specific binding of the biotinylated universal adapter to some entity that was being released from the cell upon lysis. Because fluorescent signal dropped significantly near less porous regions of the gel, it was postulated that these unknown entities were large agglomerations of proteins and possibly nucleic acids that had not been sufficiently denatured or disrupted by the use of only SDS.

A further experiment was performed in which PK was added to the lysis buffer at 200 μg/mL in an effort to digest undesirable protein complexes that could be soaking up the labeling reagents. Although the addition of this reagent seemed to eliminate the majority of the non-specific fluorescent signal when combined with an Alexa-dye-modified adapter (rather than the biotinylated adapter), there was no conclusive proof that miRNA target was being efficiently labeled with the ligation scheme. It is possible that the majority of the small miRNA targets diffused out of the particle and into the bulk solution before they were liberated from their carrier proteins. This would have prevented immediate binding with the gel-embedded probes, leading to considerable dilution in the surrounding 50-μL reaction volume. While the encapsulation experiments did not produce the desired detection results, they did establish a new route to populating microwells with particles and cells. It was clear that cells remained intact within the gel structure, and thus this should be a feasible way of simultaneously delivering cultured cells and gel particles to the nanoliter volumes of the confinement assay.

Chapter 7

Outlook

The work presented in this thesis has transformed the gel particle motif into a practical research tool that can be exploited for a variety of future studies. Although the experiments detailed in this thesis focus on the detection of miRNA, a number of significant advances have also recently been made with the gel particle platform in the analysis of other classes of biological molecules, namely proteins and mRNA transcripts [175, 214, 239, 240]. The gel particle technology has now matured to the point at which it may be truly classified as an "enabling tool", allowing for the elucidation of biological processes that are difficult if not impossible to probe with existing technologies. The ability to rapidly profile focused sets of diverse biological molecules directly in complex mixtures and physiological samples with high sensitivity and specificity offers tremendous opportunities for the development of streamlined assays that simplify research protocols in diagnostics, drug discovery, and personalized medicine. In addition to opening avenues to discovery-based research in the biological sciences, this work has generated several intriguing technological leads that can be built upon for further advances in the fields of microfluidics and molecular analysis.

At this point, I would like to acknowledge Dr. Daniel Pregibon and Dr. David Appleyard for their contributions to this thesis. In addition to initiating the encoded hydrogel microparticle project, Dr. Pregibon conceived the idea of the microfluidic scanner and contributed the majority of the initial research for the ligation labeling scheme. The achievements made in this thesis would not have been possible without his help. Dr. Appleyard was integral in the development and testing of the detection elements of the

microfluidic scanner. He was responsible for the laser setup utilized for scanning, as well as the optimization of the amplification circuit used to capture signal from the PMT. Finally, I would like to acknowledge Vincent Auyeung for supplying HeLa cells during the lysate experiments and for providing valuable advice on interpreting the results.

7.1 High-throughput Single-cell Analysis

Although we have demonstrated the isolation of cells and gel particles in microwells for enhanced miRNA detection applications, the experiments to date have been simple proofs of concept that analyze only small populations of 1–10 cells per trial. To fully realize the potential of the confinement assay, it will be necessary to develop a more robust system for loading wells with particles and 100–1000 cells for each trial. Previous work with microengraving suggests that PDMS-based microwells can be rapidly loaded with cells by simple deposition/settling processes [97, 112], but the efficient delivery of two entities (cell and particle) to each of hundreds or thousands of wells will require substantial technical innovation. The injection of cells and particles into wells with integrated microfluidic channels and valves remains a possibility, although the addition of such features would greatly increase the complexity of the process [96]. Recent unpublished work by Ki Wan Bong in the Doyle lab suggests that particles can be photolithographically synthesized in picoliter droplets. This synthesis route provides an isolated liquid-phase reaction volume for each particle, which if properly combined with a cell input, could offer a more high-throughput confinement strategy. Similarly, in recent work by the Mathies group, the dual encapsulation of cells and sensing entities in microfluidically generated agarose emulsions has been demonstrated for PCR-based gene detection with single cells [108]. In addition, the incorporation of a dielectric material such as polystyrene into the particles could potentially be used to guide well loading, as shown by work with dielectrophoretic trapping within electroactive microwell arrays [107, 241].

One alternative strategy that would avoid the challenge of delivering two entities to each reaction volume is the photolithographic fabrication of gel particles or structures within the sensing wells themselves. With appropriate monomer rinsing cycles and precise registration of photomasks with either a microscope-based system or a cleanroom mask aligner, it should be possible to synthesize well-bound gels with multiple adjacent chemistries for small-scale multiplexing of hundreds to thousands of cells. After exposure to lysed cells, these gels could be labeled and imaged within the wells, or a chemical treatment could be used to detach them from the wells so they may be processed in a manner identical to that used for the particles in previous experiments. It should also be possible to pattern a glass containment slide with gel pads containing multiple, spatially-segregated probe types using a flow-through patterning method like that employed in the creation of single-cell barcode chips in the Fan and Heath labs [96, 114]. This probe-laden slide could then be placed over the wells during incubation to capture multiple miRNA targets lysed from individual cells. Unlike the aforementioned dual delivery strategies, these two probe-

patterning methods ensure that every well featured in the assay contains a sensing element, thereby greatly augmenting the efficiency of the process.

In the exploration of new techniques for particle-based single cell analysis, there are several features of the current experimental protocol that could be altered to enhance performance. The design detailed in Chapter 6 should be regarded as a first attempt that was optimized only with respect to those parameters that could be easily altered within a limited timeframe (buffer conditions, incubation conditions, and workflow). It should be possible to improve particle/cell loading by more carefully designing the master wafer from which PDMS molds are produced. In particular, the spacing between wells can be reduced significantly to improve loading efficiency, and the incorporation of drainage channels to remove excess liquid could improve sealing and assay reproducibility [112]. Perhaps the greatest challenge that was faced in experiments with microwells was the hydrophobicity of the PDMS surface and the accompanying difficulty in spreading aqueous buffers to utilize as many wells as possible. Although plasma treatment of the PDMS can temporarily render the elastomer surface hydrophilic, only small doses of treatment could be used when depositing the gel particles, and this weak treatment only marginally improved wettability. Future work should explore and seek to eliminate the irreversible bond between plasma-treated PDMS and the gel microparticles through the use of surface treatments or the inclusion of more effective blocking agents in the incubation buffer [242]. Furthermore, there are a variety of techniques for the controlled lysis of isolated cells (*i.e.*, optical, electrical, acoustic, and mechanical lysis) that may prove more useful than the current chemical lysis, which is relatively slow and causes the denaturation of cellular proteins that may be interesting to capture in native form in future assay schemes [243].

In addition to the analysis of the lysis products of cells, it is also important to consider the design of sensing systems that can capture and quantify the molecular species that are secreted from intact single cells or small groups of cells. Indeed, there are many fundamental questions regarding the mechanism and purpose of miRNA exportation from cells, with some researchers hypothesizing that exosomal transport of these biomolecules may constitute a significant means of genetic exchange between cells [127, 132, 133]. The use of arrays of well-immobilized gel particles could enable focused profiling experiments on the frequency of exportation in different cell types, and the combination of miRNA and protein probes in a single particle type or well could potentially enable an unprecedented study of the stoichiometry of protein and nucleic acid secretion. Such a study would provide valuable insight into the nature of the exportation process and could even determine whether it is a controlled process that is directed by the cell for signaling purposes or whether it is a more random event that is used to eject cytoplasmic waste material.

Preliminary work in encapsulating cells within gel particles during SFL may also provide useful starting points for future single-cell analysis [163]. Localizing cells to gel microparticles embedded with probe molecules enables the delivery of only one entity to microwells for easier confinement assays, and cell-laden particles can be produced at

relatively high throughputs (~1 particle with an encapsulated single cell produced each second during modified SFL procedure). Although we focused solely on encapsulation within PEG-based gels and used the gel as a medium for lysis and capture, it should be possible to use other materials such as agarose and gelatin methacrylate to maintain long-term cell viability for secretion, stimulation, or proliferation studies [158, 244]. With the proper choice of materials and handling conditions, this approach could transform the particles into miniature culture environments that could potentially be combined through directed self-assembly to approximate more complex biological microenvironments.

Regardless of the confinement method, the direct and high-throughput detection of biomolecules on a single-cell level provides a range of opportunities for biological discovery. Leveraging our experience in the detection of miRNA, mRNA, and cytokines, it should be possible to develop novel biomolecule assays that allow for the characterization of expression and secretion heterogeneity over hundreds or even thousands of cells in a single trial. This type of data would be tremendously valuable in the miRNA field, where very few comprehensive studies of single-cell expression have been conducted [225]. Perhaps the greatest opportunity for discovery lies in the application of such profiling technologies to rare cell types such as circulating tumor cells (CTCs) [95]. Because of the cost and technical difficulties in isolating rare cell types, technologies that can efficiently analyze single cells without wasting sample in processing and preparation steps will play an important role in future studies of rare cells. Preliminary experiments with well-immobilized gel particles suggest that it is straightforward to analyze small numbers of cells (1–10), a practice that can sometimes be cumbersome or cost-inefficient for systems designed only to handle hundreds or thousands of cells.

7.2 Enhanced Techniques for miRNA Analysis

The detection sensitivity achieved in this thesis has proven sufficient for the direct analysis of miRNAs from small quantities of raw prostate-cancer-associated serum (miR-141) and from groups of 2–10 HeLa cells (miR-21). However, in both cases, this detection has been restricted to miRNAs with abnormally high copy numbers. As mentioned earlier, miR-141 is significantly upregulated in the serum of prostate cancer patients, while miR-21 is the most highly expressed miRNA in HeLa cells. To improve sensitivity and achieve robust profiling in these clinically important sample types, it will be necessary to introduce further innovation in the design of the particles and the reporting techniques employed for target quantification. Such advances will provide the ability to probe the expression of a greater variety of miRNAs (*i.e.*, upregulated **and** downregulated species) and will potentially provide better precision in measurement by minimizing non-specific binding and experimental noise.

The RCA labeling procedure has enabled the quantification of single-molecule binding events, and thus any future attempt to augment sensitivity should focus primarily on improving the capture efficiency of the particles. The use of an LNA-based probe has the

potential to lower the dissociation rate of the probe-target complex, thereby lowering the dissociation constant and improving the affinity for the intended target. Aside from altering the design of the probe species, there is also the option of capturing all RNA species in a sample on boronic acid polymers and then releasing the captured molecules into a smaller volume containing probe-bearing particles. This approach is similar to the confinement assay described in Chapter 6 in that it concentrates the target molecules for better capture efficiency. This so-called "bait" strategy would fit well into the current workflow of the particle system, as the hydrophobic bait molecules could potentially be integrated into one of the "blank" regions of the gel particle by loading them into oil-based nanoemulsions that can then be encapsulated during SFL [237]. Even more sophisticated core-shell structures and vertically-layered particles could be achieved through the use of hydrodynamic focusing lithography (HFL) [166]. In addition, the pseudo-selective capture and release of the RNA diol groups by the boronic acid groups of the polymer can be reversibly triggered by simple temperature changes that are already encountered in the current assay workflow [245]. This baiting approach could be particularly valuable in concentrating low-abundance miRNAs from whole blood, serum, urine, and other easily accessible biological fluids [246].

Although we have aimed for direct detection without target amplification in this thesis for reasons of simplicity, it may be beneficial in some instances to employ stem-loop RT-PCR methods for the augmentation of target copy number. The combination of PCR and gel-particle detection should be straightforward, particularly if the primer sequences are taken from previously optimized and validated multiplexing setups such as the 450-plex Megaplex reaction [142]. While this approach will require extraction of total RNA, the enhanced sensitivity that it provides may prove useful in applications in which sample is severely limited. Furthermore, the exquisite detection specificity imparted by the use of stem-loop primers could be helpful in improving discrimination of closely related sequences, such as let-7 family members and precursor/mature molecules [139]. When implemented with optimized sets of primers, this practice of "pre-amplifying" target with PCR for subsequent capture on immobilized capture probes can offer an unprecedented combination of sensitivity, specificity, throughput, and flexibility. The uncoupling of the PCR method from the traditional plate and card formats and their accompanying reading instruments has several advantages, many of which have been leveraged by Illumina in the development of the BeadArray technology [35, 59]. This system leverages the advantages of bead-based arrays (high-throughput processing of samples in parallel and rapid probe-set modification) and PCR amplification for rapid miRNA profiling in as little as 100 ng of total RNA input. However, it should be noted that the BeadArray's use of solid glass microcarriers limits the capture efficiency of the PCR amplicons, and the development of an analogous strategy for our hydrogel particles is likely to yield significantly lower limits of detection.

To streamline the assay workflow, it may be beneficial to investigate additional reporting methods. Although RCA provides single-molecule reporting resolution, it requires several more steps than the non-amplified scheme and can significantly extend processing time,

particularly with the bio-dNTP labeling strategy. It may be possible to achieve similar gains in sensitivity with a shorter workflow by using enzymatic amplification. Preliminary experiments with the use of a standard biotinylated adapter and streptavidin-conjugated horseradish peroxidase (SA-HRP) showed that the Amplex UltraRed substrate could be efficiently converted into a chemiluminescent species at a rate that appeared to scale with the input miRNA target amount (Figure 7.1). While this strategy could be easily employed in a single-plex, well-based format for colorimetric reporting, the ability to use such amplification in a one-pot multiplexed reaction would require a more judicious choice of substrate. In order for the luminescence generated by the SA-HRP attached to a particular particle to remain associated with that particle (and its code), it would be necessary to choose a substrate that will be converted into a product that will readily partition into the gel network [47]. With the recent creation of mesoporous hydrogel particles embedded with oil-based nanoemulsions [158], it should be possible to soak up hydrophobic conversion products with high efficiency for rapid fluorescent signal localization. High-sensitivity label-free reporting methods based on nanomechanical and electronic properties have also been developed in recent years for rapid miRNA detection [12, 145, 247], and it would be worthwhile to investigate the utility of such strategies in the context of the gel particle system.

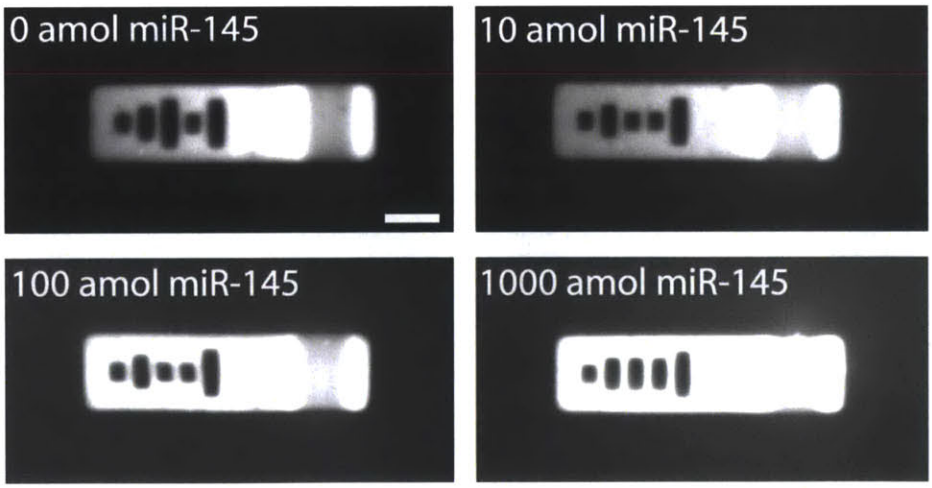

Figure 7.1: *Fluorescence images of particles exposed to different amounts of synthetic miR-145 target, labeled with SA-HRP, and exposed to Amplex UltraRed substrate. Fluorescence intensity was seen to rise in the surrounding solution and within the hydrogel as target level was increased. It is important to note that the low porosity regions of the particle (code and inert) seem to capture the fluorescent enzymatic product more readily than the probe region, suggesting that chemical composition of the particle can be tuned to localize the reporter molecule in future iterations of this assay. Scale bar is 50 μm.*

The biotinylated dNTPs used for labeling in the second generation of the RCA detection method provide lower background signal in complex samples and mixtures containing SDS and PK. Unfortunately, these modified dNTPs are incorporated very inefficiently and thus require overnight extension reactions to generate enough fluorescence for spot counting. The workflow of the assay and the intensity of the RCA spots would be improved with an alternative modified nucleotide chemistry that is more readily incorporated into the DNA extension by the type B Phi29 polymerase. It has recently been shown that several other type B polymerases incorporate 5-octadiynyl dUTP and 5-octadiynyl dCTP with high efficiency [248, 249]. Once incorporated into DNA, these alkyne-modified nucleotides can be easily linked to azide labels with high specificity via standard click chemistry methods. By clicking fluorescently modified azides to the DNA concatemer, it may be possible to attain higher levels of spot fluorescence with much shorter extension times. Furthermore, this method of labeling nucleotides in long single-stranded DNA concatemers could be employed for more fundamental studies of DNA stretching [250, 251]. The tethered RCA product could be stretched through the hydrogel network with an applied electric field, and its relaxation could be monitored with fluorescence microscopy to determine the gel pore size and other information related to the stretching mechanics.

7.3 Mixed-content Assays

As mentioned earlier, the encoded hydrogel particle platform has been adapted for the detection of a wide range of biomolecules, including DNA [52, 174], miRNA [179, 180, 205, 232], mRNA [240], and proteins [175, 214, 239]. For the development of next-generation assays for diagnostics and discovery, it may be valuable to profile multiple *types* of molecules in a single assay and perhaps even on the same particle. These "mixed-content" assays would enable, for example, the simultaneous measurement of miRNAs and their putative protein targets, allowing for more efficient profiling of biological function by compressing workflow and reducing both reagent and sample consumption [252, 253]. This approach would also offer more direct solutions in clinical diagnostics by enabling the profiling of more diverse biomarker panels. For instance, a single particle bearing an antibody probe for prostate-specific antigen and a separate DNA probe for miR-141 could be used to more robustly analyze serum samples in the study of prostate cancer. Mixed-content work could further elucidate the correlation of protein and miRNA content in exosomes and the relationship between miRNA, mRNA transcript, and protein expression in a variety of biological contexts. The highly focused set of virally-encoded miRNAs is another excellent target ensemble for the multiplexing capacity of the gel particles, and the ability to simultaneously measure 10–50 of these targets as well as their putative viral and cellular mRNA targets could provide insight into viral pathogenesis [123, 124].

Although there are established protocols for the sensitive detection of multiple classes of biomolecules on the gel particles, there are several notable differences between the methods used, particularly in the incubation temperatures and buffer conditions. It should be possible to reconcile temperature differences by using the lowest temperature from a group

of protocols (to avoid denaturation and/or melting of probe-target complex) and then increasing the duration of the incubation to enable the most complete capture possible. Specificity and sensitivity can be further adjusted by modulating salt concentration within the incubation buffer and other factors such as probe design. We have previously shown that aptamer species selected under dissimilar SELEX (systematic evolution of ligands by exponential enrichment) conditions can function effectively together in a single optimized incubation buffer [239]. It should be possible to use the same design principles distilled from that study to formulate buffers and reporting strategies that can simultaneously capture and label DNA, miRNA, mRNA, and proteins with high efficiency. In addition, it should also be straightforward to adapt the RCA reporting scheme for the labeling of single-molecule binding events of proteins and mRNAs by attaching appropriate DNA primer sequences to the reporter antibodies and label extenders that are employed for target quantification.

Bibliography

[1] Petricoin, E. F. and Liotta, L. A., "Clinical applications of proteomics," *J. Nutr.* **133**, 2476S-2484S (2003).

[2] Peck, D., Crawford, E. D., Ross, K. N., Stegmaier, K., Golub, T. R., and Lamb, J., "A method for high-throughput gene expression signature analysis," *Genome Biol.* **7**, R61 (2006).

[3] Lamb, J., Crawford, E. D., Peck, D., Modell, J. W., Blat, I. C., Wrobel, M. J., Lerner, J., Brunet, J., Subramanian, A., Ross, K. N., Reich, M., Hieronymus, H., Wei, G., Armstrong, S. A., Haggarty, S. J., Clemons, P. A., Wei, R., Carr, S. A., Lander, E. S., and Golub, T. R., "The connectivity map: Using gene-expression signatures to connect small molecules, genes, and disease," *Science* **313**, 1929-1935 (2006).

[4] Zichi, D., Eaton, B., Singer, B., and Gold, L., "Proteomics and diagnostics: Let's get specific, again," *Curr. Opin. Chem. Bio.* **12**, 78-85 (2008).

[5] Kalow, W., "Pharmacogenetics and pharmacogenomics: Origin, status, and the hope for personalized medicine," *Pharmacogenomics* **6**, 162-165 (2006).

[6] Verrills, N. M., "Clinical proteomics: Present and future prospects," *Clin. Biochemist Rev.* **27**, 99-116 (2006).

[7] Fodor, S. P., Rava, R. P., Huang, X. C., Pease, A. C., Holmes, C. P., and Adams, C. L., "Multiplexed biochemical assays with biological chips," *Nature* **364**, 555-556 (1993).

[8] Vignali, D. A. A., "Multiplexed particle-based flow cytometric assays," *J. Immunol. Methods* **243**, 243-255 (2000).

[9] Sassolas, A., Leca-Bouvier, B. D., and Blum, L. J., "DNA biosensors and microarrays," *Chem. Rev.* **108**, 109-139 (2008).

[10] Fotin, A. V., Drobyshev, A. L., Proudnikov, D. Y., Perov, A. N., and Mirzabekov, A. D., "Parallel thermodynamic analysis of duplexes on oligodeoxyribonucleotide microchips," *Nuc. Acids Res.* **26**, 1515-1521 (1998).

[11] Jennings, T. L., Rahman, K. S., Fournier-Bidoz, S., and Chan, W. C. W., "Effects of microbead surface chemistry on DNA loading and hybridization efficiency," *Anal. Chem.* **80**, 2849-2856 (2008).

[12] Husale, S., Persson, H. H. J., and Sahin, O., "DNA nanomechanics allows direct digital detection of complementary DNA and microRNA targets," *Nature* **462**, 1075-1078 (2009).

[13] He, L., Musick, M. D., Nicewarner, S. R., Salinas, F. G., Benkovic, S. J., Natan, M. J., and Keating, C. D., "Colloidal Au-enhanced surface plasmon resonance for ultrasensitive detection of DNA hybridization," *J. Am. Chem. Soc.* **122**, 9071-9077 (2000).

[14] Alexandre, I., Hamels, S., Dufour, S., Collet, J., Zammatteo, N., De Longueville, F., Gala, J., and Remacle, J., "Colorimetric silver detection of DNA microarrays," *Anal. Biochem.* **295**, 1-8 (2001).

[15] Cho, E., Collett, J., Szafranska, A., and Ellington, A., "Optimization of aptamer microarray technology for multiple protein targets," *Anal. Chim. Acta* **564**, 82-90 (2006).

[16] Hudson, M. E., Pozdnyakova, I., Haines, K., Mor, G., and Snyder, M., "Identification of differentially expressed proteins in ovarian cancer using high-density protein microarrays," *Proc. Natl. Acad. Sci. U.S.A.* **104**, 17494-17499 (2007).

[17] Peluso, P., Wilson, D. S., Do, D., Tran, H., Venkatasubbaiah, M., Quincy, D., Heidecker, B., Poindexter, K., Tolani, N., Phelan, M., Witte, K., Jung, L. S., Wagner, P., and Nock, S., "Optimizing antibody immobilization strategies for the construction of protein microarrays," *Anal. Biochem.* **312**, 113-124 (2003).

[18] Gresham, D., Dunham, M. J., and Botstein, D., "Comparing whole genomes using DNA microarrays," *Nat. Rev. Genet.* **9**, 291-302 (2008).

[19] Rubina, A. Y., Kolchinsky, A., Makarov, A. A., and Zasedatelev, A. S., "Why 3-D? Gel-based microarrays in proteomics," *Proteomics* **8**, 817-831 (2008).

[20] Petersen, M. and Wengel, J., "LNA: A versatile tool for therapeutics and genomics," *Trends Biotechnol.* **21**, 74-81 (2003).

[21] Rubina, A. Y., Pan'kov, S. V., Dementieva, E. I., Pen'kov, D. N., Butygin, A. V., Vasiliskov, V. A., Chudinov, A. V., Mikheikin, A. L., Mikhailovich, V. M., and Mirzabekov, A. D., "Hydrogel drop microchips with immobilized DNA: Properties and methods for large-scale production," *Anal. Biochem.* **325**, 92-106 (2004).

[22] Kashkin, K. N., Strizhkov, B. N., Gryadunov, D. A., Surzhikov, S. A., Grechishnikova, I. V., Kreindlin, E. Y., Chupeeva, V. V., Evseev, K. B., Turygin, A. Y., and Mirzabekov, A. D., "Detection of single-nucleotide polymorphisms in the p53 gene by LDR/RCA in hydrogel microarrays," *Mol. Biol. (Moscow, Russian Federation, English Edition)* **39**, 30-39 (2005).

[23] Kolchinsky, A. M., Gryadunov, D. A., Lysov, Y. P., Mikhailovich, V. M., Nasedkina, T. V., Turygin, A. Y., Rubina, A. Y., Barsky, V. E., and Zasedatelev, A. S., "Gel-based microchips: History and prospects," *Mol. Biol.* **38**, 4-13 (2004).

[24] Zubtsov, D. A., Savvateeva, E. N., Rubina, A. Y., Pan'kov, S. V., Konovalova, E. V., Moiseeva, O. V., Chechetkin, V. R., and Zasedatelev, A. S., "Comparison of surface and hydrogel-based protein microchips," *Anal. Biochem.* **368**, 205-213 (2007).

[25] Sorokin, N. V., Chechetkin, V. R., Pan'kov, S. V., Somova, O. G., Livshits, M. A., Donnikov, M. Y., Turygin, A. Y., Barsky, V. E., and Zasedatelev, A. S., "Kinetics of hybridization on surface oligonucleotide microchips: Theory, experiment, and comparison with hybridization on gel-based microchips," *J. Biomol. Struct. Dyn.* **24**, 57-66 (2006).

[26] Wilson, R., Cossins, A. R., and Spiller, D. G., "Encoded Microcarriers for high-throughput multiplexed detection," *Angew. Chem. Int. Ed.* **45**, 6104-6117 (2006).

[27] Fulton, R. J., McDade, R. L., Smith, P. L., Kienker, L. J., and Kettman Jr., J. R., "Advanced multiplexed analysis with the Flowmetrix system," *Clin. Chem.* **43**, 1749-1756 (1997).

[28] Han, M., Gao, X., Su, J. Z., and Nie, S., "Quantum-dot-tagged microbeads for multiplexed optical coding of biomolecules," *Nat. Biotechnol.* **19**, 631-635 (2001).

[29] Fenniri, H., Chun, S., Ding, L., Zyrianov, Y., and Hallenga, K., "Preparation, physical properties, on-bead binding assays and spectroscopic reliability of 25 barcoded polystyrene-poly(ethylene glycol) graft copolymers," *J. Am. Chem. Soc.* **125**, 10546-10560 (2003).

[30] Chovan, T. and Guttman, A., "Microfabricated devices in biotechnology and biochemical processing," *Trends Biotechnol.* **20**, 116-122 (2002).

[31] Evans, M., Sewter, C., and Hill, E., "An encoded particle array tool for multiplex bioassays," *Assay Drug Dev. Technol.* **1**, 199-207A (2003).

[32] Zhi, Z., Morita, Y., Hasan, Q., and Tamiya, E., "Micromachining microcarrier-based biomolecular encoding for miniaturized and multiplexed immunoassay," *Anal. Chem.* **75**, 4125-4131 (2003).

[33] Nicewarner-Pena, S. R., Freeman, R. G., Reiss, B. D., He, L., Pena, D. J., Walton, I. D., Cromer, R., Keating, C. D., and Natan, M. J., "Submicrometer metallic barcodes," *Science* **294**, 137-141 (2001).

[34] Braeckmans, K., Smedt, S. C. D., Roelant, C., Leblans, M., Pauwels, R., and Demeester, J., "Encoding microcarriers by spatial selective photobleaching," *Nat. Mater.* **2**, 169-173 (2003).

[35] http://www.illumina.com

[36] Xiao, X. Y., Li, R., Zhuang, H., Ewing, B., Karunaratne, K., Lillig, J., Brown, R., and Nicolaou, K. C., "Solid-phase combinatorial synthesis using MicroKan reactors, Rf tagging, and directed sorting," *Biotechnol. BIoeng.* **71**, 44-50 (2000).

[37] Meiring, J. E., Schmid, M. J., Grayson, S. M., Rathsack, B. M., Johnson, D. M., Kirby, R., Kannappan, R., Manthiram, K., Hsia, B., Hogan, Z. L., Ellington, A. D., Pishko, M. V., and Willson, C. G., "Hydrogel biosensor array platform indexed by shape," *Chem. Mater.* **16**, 5574-5580 (2004).

[38] Meiring, J. E., Lee, S., Costner, E. A., Schmid, M. J., Michaelson, T. B., Willson, C. G., and Grayson, S. M., "Pattern recognition of shape-encoded hydrogel biosensor arrays," *Opt. Eng.* **48**, (2009).

[39] Vaino, A. R. and Janda, K. D., "Euclidean shape-encoded combinatorial chemical libraries," *Proc. Natl. Acad. Sci. U.S.A.* **97**, 7692-7696 (2000).

[40] Lee, H., Kim, J., Kim, H., and Kwon, S., "Colour-barcoded magnetic microparticles for multiplexed bioassays," *Nature Mater.* **9**, 745-749 (2010).

[41] http://www.luminexcorp.com

[42] http://www.millipore.com

[43] Carson, R. T. and Vignali, D. A. A., "Simultaneous quantification of fifteen cytokines using a multiplexed flow cytometric assay," *J. Immunol. Methods* **227**, 41-44 (1999).

[44] Birtwell, S. and Morgan, H., "Microparticle encoding technologies for high-throughput multiplexed suspension assays," *Integr. Biol.* **1**, 345-362 (2009).

[45] Cederquist, K. B., Dean, S. L., and Keating, C. D., "Encoded anisotropic particles for multiplexed bioanalysis," *Nanomed. Nanobiotechnol.* **2**, 578-600 (2010).

[46] Finkel, N. H., Lou, X. H., Wang, C. Y., and He, L., "Barcoding the microworld," *Anal. Chem.* **76**, 353A-359A (2004).

[47] Lee, W., Choi, D., Kim, J., and Koh, W., "Suspension arrays of hydrogel microparticles prepared by photopatterning for multiplexed protein-based bioassays," *Biomed. Microdevices* **10**, 813-822 (2008).

[48] Sha, M. Y., Walton, I. D., Norton, S. M., Taylor, M., Yamanaka, M., Natan, M. J., Xu, C., Drmanac, S., Huang, S., Borcherding, A., Drmanac, R., and Penn, S., "Multiplexed SNP genotyping using nanobarcode particle technology," *Anal. Bioanal. Chem.* **384**, 658-666 (2006).

[49] Bong, K. W., Chapin, S. C., and Doyle, P. S., "Magnetic barcoded hydrogel microparticles for multiplexed detection," *Langmuir* **46**, 8008-8014 (2010).

[50] Kellar, K. L. and Iannone, M. A., "Multiplexed microsphere-based flow cytometric assays," *Exp. Hematol.* **30**, 1227-1237 (2002).

[51] Kellar, K. L. and Douglass, J. P., "Multiplexed microsphere-based flow cytometric immunoassays for human cytokines," *J. Immunol. Methods* **279**, 277-285 (2003).

[52] Pregibon, D. C., Toner, M., and Doyle, P. S., "Multifunctional encoded particles for high-throughput biomolecule analysis," *Science* **315**, 1393-1396 (2007).

[53] Hurley, J. D., Engle, L. J., Davis, J. T., Welsh, A. M., and Landers, J. E., "A simple, bead-based approach for multi-SNP molecular haplotyping," *Nuc. Acids Res.* **32**, e186 (2004).

[54] McBride, M. T., Gammon, S., Pitesky, M., O'Brien, T. W., Smith, T., Alrich, L., Langlois, R. G., Colston, B., and Venkateswaran, K. S., "Multiplexed liquid arrays for simultaneous detection of simulants of biological warfare agents," *Anal. Chem.* **75**, 1924-1930 (2003).

[55] Luo, Y., "Selectivity assessment of kinase inhibitors: Strategies and challenges," *Curr. Opin. Mol. Ther.* **7**, 251-255 (2005).

[56] Morgan, E., Varro, R., Sepulveda, H., Ember, J. A., Apgar, J., Wilson, J., Lowe, L., Chen, R., Shivraj, L., Agadir, A., Campos, R., Ernst, D., and Gaur, A., "Cytometric bead array: A multiplexed assay platform with applications in various areas of biology," *Clin. Immunol.* **110**, 252-266 (2004).

[57] Tarnok, A., Hambsch, J., Chen, R., and Varro, R., "Cytometric bead array to measure six cytokines in twenty-five microliters of serum," *Clin. Chem.* **49**, 1000-1002 (2003).

[58] Dames, A., England, J., and Colby, E., "WO Patent 00/16893," (2000).

[59] Chen, J., Lozach, J., Garcia, E. W., Barnes, B., Luo, S., Mikoulitch, I., Zhou, L., Schroth, G., and Fan, J. B., "Highly sensitive and specific microRNA expression profiling using BeadArray technology," *Nuc. Acids Res.* **36**, e87 (2008).

[60] Chung, T. D. and Kim, H. C., "Recent advances in miniaturized microfluidic flow cytometry for clinical use," *Electrophoresis* **28**, 4511-4520 (2007).

[61] Huh, D., Gu, W., Kamotani, Y., Grotberg, J. B., and Takayama, S., "Microfluidics for flow cytometric analysis of cells and particles," *Physiol. Meas.* **26**, R73-R98 (2005).

[62] Simonnet, C. and Groisman, A., "High-throughput and high-resolution flow cytometry in molded microfluidic devices," *Anal. Chem.* **78**, 5653-5663 (2006).

[63] Yang, A. S. and Hsieh, W. H., "Hydrodynamic focusing investigation in a micro-flow cytometer," *Biomed. Microdevices* **9**, 113-122 (2006).

[64] Simonnet, C. and Groisman, A., "Two-dimensional hydrodynamic flow focusing in a simple microfluidic device," *Appl. Phys. Lett.* **87**, 114104 (114101-114103) (2005).

[65] Chang, C. C., Huang, Z. X., and Yang, R. J., "Three-dimensional hydrodynamic focusing in two-layer polydimethylsiloxane (PDMS) microchannels," *J. Micromech. Microeng.* **17**, 1479-1486 (2007).

[66] Chau, L. K., Osborn, T., Wu, C. C., and Yager, P., "Microfabricated silicon flow-cell for optical monitoring of biological fluids," *Anal. Sci.* **15**, 721-724 (1999).

[67] Chung, S., Park, S. J., Kim, J. K., Chung, C., Han, D. C., and Chang, J. K., "Plastic microchip flow cytometer based on 2- and 3-dimensional hydrodynamic flow focusing," *Microsyst. Technol.* **9**, 525-533 (2003).

[68] Chan, S. D. H., Luedke, G., Valer, M., Buhlmann, C., and Preckel, T., "Cytometric analysis of protein expression and apoptosis in human primary cells with a novel microfluidic chip-based system," *Cytometry A* **55**, 119-125 (2003).

[69] Yao, B., Luo, G. A., Feng, X., Wang, W., Chen, L., and Wang, Y., "A microfluidic device based on gravity and electric force driving for flow cytometry and fluorescence activated cell sorting," *Lab Chip* **4**, 603-607 (2004).

[70] Fu, L. M., Yang, R. J., Lin, C. H., Pan, Y. J., and Lee, G. B., "Electrokinetically driven micro flow cytometers with integrated fiber optics for on-line cell/particle detection," *Anal. Chim. Acta* **507**, 163-169 (2003).

[71] McClain, M. A., Culbertson, C. T., Jacobsen, S. C., and Ramsey, J. M., "Flow cytometry of Escherichia coli on microfluidic devices," *Anal. Chem.* **73**, 5334-5338 (2001).

[72] McClain, M. A., Culbertson, C. T., Jacobsen, S. C., Allbritton, N. L., Sims, C. E., and Ramsey, J. M., "Microfluidic devices for the high-throughput chemical analysis of cells," *Anal. Chem.* **75**, 5646-5655 (2003).

[73] Lee, G. B., Hung, C. I., Ke, B. J., Huang, G. R., Hwei, B. H., and Lai, H. F., "Hydrodynamic focusing for a micromachined flow cytometer," *Trans. ASME I* **123**, 672-679 (2001).

[74] Balslev, S., Jorgensen, A. M., Bilenberg, B., Morgensen, K. B., Snakenborg, D., Geschke, O., Kutter, J. P., and Kirstensen, A., "Lab-on-a-chip with integrated optical transducers," *Lab Chip* **6**, 213-217 (2006).

[75] Chung, K., Crane, M. M., and Lu, H., "Automated on-chip rapid microscopy, phenotyping and sorting of *C. elegans*," *Nat. Meth.* **5**, (2008).

[76] Wang, A., El-Ali, J., Perch-Nielsen, I. R., Mogensen, K. B., Snakenborg, D., Kutter, J. P., and Wolff, A., "Microchip flow cytometer with integrated polymer optical elements for measurement of scattered light," *Lab Chip* **4**, 372-377 (2004).

[77] Johnson, M. E. and Landers, J. P., "Fundamentals and practice for ultrasensitive laser-induced fluorescence detection in microanalytical systems," *Electrophoresis* **25**, 3513-3527 (2004).

[78] Niehren, S., Kinzelbach, W., Seeger, S., and Wolfrum, J., "An all-solid-state flow cytometer for counting fluorescent microspheres," *Anal. Chem.* **67**, 2666-2671 (1995).

[79] Ferris, M. M., McCabe, M. O., Doan, L. G., and Rowlen, K. L., "Rapid enumeration of respiratory viruses," *Anal. Chem.* **74**, 1849-1856 (2002).

[80] Gawad, S., Batard, P., Seger, U., Metz, S., and Renaud, P., *MicroTAS Conf. Proc., Kluwer Academic Publ., Japan* 649-651 (2002).

[81] Chun, H., Chung, T. D., and Kim, H. C., "Cytometry microchip using polymer-based saltbridge electrodes," *Conf. Proc. IEEE Eng. Med. Biol. Soc.* **4**, 2584-2586 (2004).

[82] Chun, H., Chung, T. D., and Kim, H. C., "Cytometry and velocimetry on a microfluidic chip using polyelectrolytic salt bridges," *Anal. Chem.* **77**, 2490-2495 (2005).

[83] Kleppe, K., Ohtsuka, E., Kleppe, R., Molineux, I., and Khorana, H. G., "Studies on polynucleotides: XCVI. Repair replications of short synthetic DNA's as catalyzed by DNA polymerases," *J. Mol. Biol.* **56**, 341-361 (1971).

[84] Newton, C. R., Graham, A., Heptinstall, L. E., Powell, S. J., Summers, C., Kalsheker, N., Smith, J. C., and Markham, A. F., "Analysis of any point mutation in DNA. The amplification refractory mutation system (ARMS)," *Nuc. Acids Res.* **17**, 2503-2516 (1989).

[85] Herman, J. G., Graff, J. R., Myohanen, S., Nelkin, B. D., and Baylin, S. B., "Methylation-specific PCR: A novel PCR assay for methylation status of CpG islands," *Proc. Natl. Acad. Sci. U.S.A.* **93**, 9821-9826 (1996).

[86] Bustin, S. A., "Quantification of mRNA using real-time reverse transcription PCR (RT-PCR): Trends and problems," *J. Mol. Endocrinol.* **29**, 23-39 (2002).

[87] Fredriksson, S., Gullberg, M., Jarvius, J., Olsson, C., Pietras, K., Gustafsdottir, S. M., Ostman, A., and Landegren, U., "Protein detection using proximity-dependent DNA ligation assays," *Nat. Biotechnol.* **20**, 473-477 (2002).

[88] Heid, C. A., Stevens, J., Livak, K. J., and Williams, P. M., "Real time quantitative PCR," *Genome Res.* **6**, 986-994 (1996).

[89] http://www.appliedbiosystems.com

[90] Squires, T. M., Messinger, R. J., and Manalis, S. R., "Making it stick: Convection, reaction and diffusion in surface-based biosensors," *Nat. Biotechnol.* **26**, 417-426 (2008).

[91] Wheeler, A. R., Throndset, W. R., Whelan, R. J., Leach, A. M., Zare, R. N., Liao, Y. H., Farrell, K., Manger, I. D., and Daridon, A., "Microfluidic device for single-cell analysis," *Anal. Chem.* **75**, 3581-3586 (2003).

[92] Wang, D. and Bodovitz, S., "Single cell analysis: The new frontier in 'omics'," *Trends Biotechnol.* **28**, 281-290 (2010).

[93] Di Carlo, D. and Lee, L. P., "Dynamic single-cell analysis for quantitative biology," *Anal. Chem.* **78**, 7918-7925 (2006).

[94] Toriello, N. M., Douglas, E. S., Thaitrong, N., Hsiao, S. C., Francis, M. B., Bertozzi, C. R., and Mathies, R. A., "Integrated microfluidic bioprocessor for single-cell gene expression analysis," *Proc. Natl. Acad. Sci. U.S.A.* **105**, 20173-20178 (2008).

[95] Nagrath, S., Sequist, L. V., Maheswaran, S., Bell, D. W., Irimia, D., Ulkus, L., Smith, M. R., Kwak, E. L., Digumarthy, S., Muzikansky, A., Ryan, P., Balis, U. J.,

Tompkins, R. G., Haber, D. A., and Toner, M., "Isolation of rare circulating tumour cells in cancer patients by microchip technology," *Nature* **450**, 1235-1239 (2007).

[96] Ma, C., Fan, R., Ahmad, H., Shi, Q., Comin-Anduix, B., Chodon, T., Koya, R. C., Liu, C., Kwong, G. A., Radu, C. G., Ribas, A., and Heath, J. R., "A clinical microchip for evaluation of single immune cells reveals high functional heterogeneity in phenotypically similar T cells," *Nat. Med.* **17**, 738-743 (2011).

[97] Love, J. C., Ronan, J. L., Grotenbreg, G. M., van der Veen, A. G., and Ploegh, H. L., "A microengraving method for rapid selection of single cells producing antigen-specific antibodies," *Nat. Biotechnol.* **24**, 703-707 (2006).

[98] Voldman, J., Gray, M. L., Toner, M., and Schmidt, M. A., "A microfabrication-based dynamic array cytometer," *Anal. Chem.* **74**, 3984-3990 (2002).

[99] http://www.fluidigm.com

[100] Clarke, M. F., Dick, J. E., Dirks, P. B., Eaves, C. J., Jamieson, C. H. M., Jones, D. L., Visvader, J., Weissman, I. L., and Wahl, G. M., "Cancer stem cells - Perspectives on current status and future directions: AACR workshop on cancer stem cells," *Cancer Res.* **66**, 9339-9344 (2006).

[101] Pinkel, D., Segraves, R., Sudar, D., Clark, S., Poole, I., Kowbel, D., Collins, C., Kuo, W., Chen, C., Zhai, Y., Dairkee, S. H., Ljung, B., Gray, J. W., and Albertson, D. G., "High resolution analysis of DNA copy number variation using comparative genomic hybridization to microarrays," *Nat. Genet.* **20**, 207-211 (1998).

[102] Rettig, J. R. and Folch, A., "Large-scale single-cell trapping and imaging using microwell arrays," *Anal. Chem.* **77**, 5628-5634 (2005).

[103] Wood, D. K., Weingeist, D. M., Bhatia, S. N., and Engelward, B. P., "Single cell trapping and DNA damage analysis using microwell arrays," *Proc. Natl. Acad. Sci. U.S.A.* **107**, 10008-10013 (2010).

[104] Di Carlo, D., Aghdam, N., and Lee, L. P., "Single-cell enzyme concentrations, kinetics, and inhibition analysis using high-density hydrodynamic cell isolation arrays," *Anal. Chem.* **78**, 4925-4930 (2006).

[105] http://www.arryx.com

[106] Voldman, J., "Electrical forces for microscale cell manipulation," *Annu. Rev. Biomed. Eng.* **8**, 425-454 (2006).

[107] Kim, S. H., Yamamoto, T., Fourmy, D., and Fujii, T., "Electroactive microwell arrays for highly efficient single-cell trapping and analysis," *Small* **7**, 3239-3247 (2011).

[108] Novak, R., Zeng, Y., Shuga, J., Venugopalan, G., Fletcher, D. A., Smith, M. T., and Mathies, R. A., "Single-cell multiplex gene detection and sequencing with microfluidically generated agarose emulsions," *Angew. Chem., Int. Ed.* **50**, 390-395 (2011).

[109] Marcus, J. S., Anderson, W. F., and Quake, S. R., "Microfluidic single-cell mRNA isolation and analysis," *Anal. Chem.* **78**, 3084-3089 (2006).

[110] Thorsen, T., Maerkl, S. J., and Quake, S. R., "Microfluidic large scale integration," *Science* **298**, 580-584 (2002).

[111] Han, Q., Bradshaw, E. M., Nilsson, B., Hafler, D. A., and Love, J. C., "Multidimensional analysis of the frequencies and rates of cytokine secretion from single cells by quantitative microengraving," *Lab Chip* **10**, 1391-1400 (2010).

[112] Ogunniyi, A. O., Story, C. M., Papa, E., Guillen, E., and Love, J. C., "Screening individual hybridomas by microengraving to discover monoclonal antibodies," *Nat. Protocols* **4**, 767-782 (2009).

[113] Gong, Y., Ogunniyi, A. O., and Love, J. C., "Massively parallel detection of gene expression in single cells using subnanoliter wells," *Lab Chip* **10**, 2334-2337 (2010).

[114] Fan, R., Vermesh, O., Srivastava, A., Yen, B. K. H., Qin, L. D., Ahmad, H., Kwong, G. A., Liu, C. C., Gould, J., Hood, L., and Heath, J. R., "Integrated barcode chips for rapid, multiplexed analysis of proteins in microliter quantities of blood," *Nat. Biotechnol.* **26**, 1373-1378 (2008).

[115] Lee, R. C., Feinbaum, R. L., and Ambros, V., "The *C. elegans* heterochronic gene *lin-4* encodes small RNAs with antisense complementarity to *lin-14*," *Cell* **75**, 843-854 (1993).

[116] Bartel, D. P., "MicroRNAs: Genomics, biogenesis, mechanism, and function," *Cell* **116**, 281-297 (2004).

[117] Esquela-Kerscher, A. and Slack, F. J., "Oncomirs - microRNAs with a role in cancer," *Nat. Rev. Cancer* **6**, 259-269 (2006).

[118] He, L. and Hannon, G. J., "MicroRNAs: Small RNAs with a big role in gene regulation," *Nat. Rev. Genet.* **5**, 522-531 (2004).

[119] Winter, J., Jung, S., Keller, S., Gregory, R. I., and Diederichs, S., "Many roads to maturity: MicroRNA biogenesis pathways and their regulation," *Nat. Cell Biol.* **11**, 228-234 (2009).

[120] Provost, P., "MicroRNAs as a molecular basis for mental retardation, Alzheimer's and prion diseases," *Brain Res.* **1338**, 58-66 (2010).

[121] Small, E. M., Frost, R. J. A., and Olson, E. N., "MicroRNAs add a new dimension to cardiovascular disease," *Circulation* **121**, 1022-1032 (2010).

[122] Chable-Bessia, C., Meziane, O., Latreille, D., Triboulet, R., Zamborlini, A., Wagschal, A., Jacquet, J., Reynes, J., Levy, Y., Saib, A., Bennasser, Y., and Benkirane, M., "Suppression of HIV-1 replication by microRNA effectors," *Retrovirology* **6**, 1-11 (2009).

[123] Cullen, B. R., "Viruses and microRNAs," *Nat. Genet.* **38**, S25-S30 (2006).

[124] Cullen, B. R., "Viral and cellular messenger RNA targets of viral microRNAs," *Nature* **457**, 421-425 (2009).

[125] Lu, J., Getz, G., Miska, E. A., Alvarez-Saavedra, E., Lamb, J., Peck, D., Sweet-Cordero, A., Ebert, B. L., Mak, R. H., Ferrando, A. A., Downing, J. R., Jacks, T., Horvitz, H. R., and Golub, T. R., "MicroRNA expression profiles classify human cancers," *Nature* **435**, 834-838 (2005).

[126] Ramaswamy, S., Tamayo, P., Rifkin, R., Mukherjee, S., Yeang, C., Angelo, M., Ladd, C., Reich, M., Latulippe, E., Mesirov, J. P., Poggio, T., Gerald, W., Loda, M., Lander, E. S., and Golub, T. R., "Multiclass cancer diagnosis using tumor gene expression signatures," *Proc. Natl. Acad. Sci. U.S.A.* **98**, 15149-15154 (2001).

[127] Arroyo, J. D., Chevillet, J. R., Kroh, E. M., Ruf, I. K., Pritchard, C. C., Gibson, D. F., Mitchell, P. S., Bennett, C. F., Pogosova-Agadjanyan, E. L., Stirewalt, D. L., Tait, J. F., and Tewari, M., "Argonaute2 complexes carry a population of circulating microRNAs independent of vesicles in human plasma," *Proc. Natl. Acad. Sci. U.S.A.* **108**, 5003-5008 (2011).

[128] Mitchell, P. S., Parkin, R. K., Kroh, E. M., Fritz, B. R., Wyman, S. K., Pogosova-Agadjanyan, E. L., Peterson, A., Noteboom, J., O'Briant, K. C., Allen, A., Lin, D. W., Urban, N., Drescher, C. W., Knudsen, B. S., Stirewalt, D. L., Gentleman, R., Vessella, R. L., Nelson, P. S., Martin, D. B., and Tewari, M., "Circulating microRNAs as stable blood-based markers for cancer detection," *Proc. Natl. Acad. Sci. U.S.A.* **105**, 10513-10518 (2008).

[129] Cortez, M. A., Bueso-Ramos, C., Ferdin, J., Lopez-Berestein, G., Sood, A. K., and Calin, G. A., "MicroRNAs in body fluids - The mix of hormones and biomarkers," *Nat. Rev. Clin. Oncol.* **8**, 467-477 (2011).

[130] Keller, A., Leidinger, P., Bauer, A., ElSharawy, A., Haas, J., Backes, C., Wendschlag, A., Giese, N., Tjaden, C., Ott, K., Werner, J., Hackert, T., Ruprecht, K., Huwer, H., Huebers, J., Jacobs, G., Rosenstiel, P., Dommisch, H., Schaefer, A., Muller-Quernheim, J., Wullich, B., Keck, B., Graf, N., Reichrath, J., Vogel, B., Nebel, A., Jager, S. U., Staehler, P., Amarantos, I., Boisguerin, V., Staehler, C., Beier, M., Scheffler, M., Buchler, M. W., Wischhusen, J., Haeusler, S. F. M., Dietl, J., Hofmann, S., Lenhof, H., Schreiber, S., Katus, H. A., Rottbauer, W., Meder, B., Hoheisel, J. D., Franke, A., and Meese, E., "Toward the blood-borne miRNome of human diseases," *Nat. Methods* **8**, 841-843 (2011).

[131] Jiang, W., Chen, X., Liao, M., Li, W., Lian, B., Wang, L., Meng, F., Liu, X., Chen, X., Jin, Y., and Xia, L., "Identification of links between small molecules and miRNAs in human cancers based on transcriptional responses," *Sci. Rep.* **2**, Article No. 282 (2012).

[132] Pegtel, D. M., Cosmopoulos, K., Thorley-Lawson, D. A., van Eijndhoven, M. A. J., Hopmans, E. S., Lindenberg, J. L., de Gruijl, T. D., Wurdinger, T., and Middeldorp,

J. M., "Functional delivery of viral microRNAs via exosomes," *Proc. Natl. Acad. Sci. U.S.A.* **107**, 6328-6333 (2010).

[133] Valadi, H., Ekstrom, K., Bossios, A., Sjostrand, M., Lee, J. J., and Lotvall, J. O., "Exosome-mediated transfer of mRNAs and microRNAs is a novel mechanism of genetic exchange between cells," *Nat. Cell Biol.* **9**, (2007).

[134] Baker, M., "MicroRNA profiling: separating signal from noise," *Nat. Methods* **7**, 687-692 (2010).

[135] Bissels, U., WIld, S., Tomiuk, S., Holste, A., Hafner, M., Tuschl, T., and Bosio, A., "Absolute quantification of microRNAs by using a universal reference," *RNA* **15**, 2375-2384 (2009).

[136] Li, W. and Ruan, K., "MicroRNA detection by microarray," *Anal. Bioanal. Chem.* **394**, 1117-1124 (2009).

[137] Wang, B., Howel, P., Bruheim, S., Ju, J., Owen, L. B., Fodstad, O., and Xi, Y., "Systematic evaluation of three microRNA profiling platforms: Microarray, beads array, and quantitative real-time PCR array," *PLoS ONE* **6**, e17167 (2011).

[138] Wang, H., Ach, R. A., and Curry, B., "Direct and sensitive miRNA profiling from low-input total RNA," *RNA* **13**, 151-159 (2007).

[139] Chen, C., Ridzon, D. A., Broomer, A. J., Zhou, Z., Lee, D. H., Nguyen, J. T., Barbisin, M., Xu, N. L., Mahuvakar, V. R., Andersen, M. R., Lao, K. Q., Livak, K. J., and Guegler, K. J., "Real-time quantification of microRNAs by stem-loop RT-PCR," *Nuc. Acids Res.* **33**, e179 (2005).

[140] Tang, F., Hajkova, P., Barton, S. C., Lao, K., and Surani, M. A., "MicroRNA expression profiling of single whole embryonic stem cells," *Nuc. Acids Res.* **34**, e9 (2006).

[141] Tang, F., Hajkova, P., Barton, S. C., O'Carroll, D., Lee, C., Lao, K., and Surani, M. A., "220-plex microRNA expression profile of a single cell," *Nat. Protocols* 1, 1154-1159 (2006).

[142] Mestdagh, P., Feys, T., Bernard, N., Guenther, S., Chen, C., Speleman, F., and Vandesompele, J., "High-throughput stem-loop RT-qPCR miRNA expression profiling using minute amounts of input RNA," *Nuc. Acids Res.* **36**, e143 (2008).

[143] Sempere, L. F., Freemantle, S., Pitha-Rowe, I., Moss, E., Dmitrovsky, E., and Ambros, V., "Expression profiling of mammalian microRNAs uncovers a subset of brain-expressed microRNAs with possible roles in murine and human neuronal differentiation," *Genome Biol.* **5**, R13 (2004).

[144] Persat, A. and Santiago, J. G., "MicroRNA profiling by simultaneous selective isotachophoresis and hybridization with molecular beacons," *Anal. Chem.* **83**, 2310-2316 (2011).

[145] Wanunu, M., Dadosh, T., Ray, V., Jin, J., McReynolds, L., and Drndic, M., "Rapid electronic detection of probe-specific microRNAs using thin nanopore sensors," *Nat. Nanotechnol.* **5**, 807-814 (2010).

[146] Lusi, E. A., Passamano, M., Guarascio, P., Scarpa, A., and Schiavo, L., "Innovative electrochemical approach for an early detection of microRNAs," *Anal. Chem.* **81**, 2819-2822 (2009).

[147] Yang, S. W. and Vosch, T., "Rapid detection of microRNA by a silver nanocluster DNA probe," *Anal. Chem.* **83**, 6935-6939 (2011).

[148] Li, J., Schachermeyer, S., Wang, Y., Yin, Y., and Zhong, W., "Detection of microRNA by fluorescence amplification based on cation-exchange in nanocrystals," *Anal. Chem.* **81**, 9723-9729 (2009).

[149] Creighton, C. J., Reid, J. G., and Gunaratne, P. H., "Expression profiling of microRNAs by deep sequencing," *Briefings Bioinf.* **10**, 490-497 (2009).

[150] Kolishetti, N., Dhar, S., Valencia, P. M., Lin, L. Q., Karnik, R., Lippard, S. J., Langer, R., and Farokhzad, O. C., "Engineering of self-assembled nanoparticle platform for precisely controlled combination drug threapy," *Proc. Natl. Acad. Sci. U.S.A.* **107**, 17939-17944 (2010).

[151] Mei, Q., Fredrickson, C. K., Simon, A., Khnouf, R., and Fan, Z. H., "Cell-free protein synthesis in microfluidic array devices," *Biotecnol. Prog.* **23**, 1305-1311 (2008).

[152] Cho, M., Xiao, Y., Nie, J., Stewart, R., Csordas, A. T., Oh, S. S., Thomson, J. A., and Soh, H. T., "Quantitative selection of DNA aptamers through microfluidic selection and high-throughput sequencing," *Proc. Natl. Acad. Sci. U.S.A.* **107**, 15373-15378 (2010).

[153] Dendukuri, D., Pregibon, D. C., Collins, J., Hatton, T. A., and Doyle, P. S., "Continuous-flow lithography for high-throughput microparticle synthesis," *Nature Mater.* **5**, 365-369 (2006).

[154] Dendukuri, D., Hatton, T. A., and Doyle, P. S., "Synthesis and self-assembly of amphiphilic polymeric microparticles," *Langmuir* **23**, 4669-4674 (2007).

[155] Decker, C. and Jenkins, A. D., "Kinetic approach of O_2 inhibition in ultraviolet-induced and laser-induced polymerizations," *Macromolecules* **18**, 1241-1244 (1985).

[156] Love, J. C., Wolfe, D. B., Jacobs, H. O., and Whitesides, G. M., "Microscope projection photolithography for rapid prototyping of masters with micro-scale features for use in soft lithography," *Langmuir* **17**, 6005-6012 (2001).

[157] Dendukuri, D. and Doyle, P. S., "The synthesis and assembly of polymeric microparticles using microfluidics," *Adv. Mater.* **21**, 4071-4086 (2009).

[158] Helgeson, M. E., Chapin, S. C., and Doyle, P. S., "Hydrogel microparticles from lithographic processes: novel materials for fundamental and applied colloid science," *Curr. Opin. Colloid Interface Sci.* **16**, 106-117 (2011).

[159] Deen, W. M., *Analysis of Transport Phenomena*, Oxford University Press, New York, 1st Edn., 270-278 (1998).

[160] Dendukuri, D., Gu, S. S., Pregibon, D. C., Hatton, T. A., and Doyle, P. S., "Stop-flow lithography in a microfluidic device," *Lab Chip* **7**, 818-828 (2007).

[161] Bong, K. W., Chapin, S. C., Pregibon, D. C., Baah, D., Floyd-Smith, T. M., and Doyle, P. S., "Compressed-air flow system," *Lab Chip* **11**, 743-747 (2011).

[162] Hwang, D. K., Oakey, J., Toner, M., Arthur, J., Anseth, K., Lee, S., Zeiger, A., Van Vliet, K., and Doyle, P. S., "Stop-flow lithography for the production of shape-evolving degradable microgel particles," *J. Am. Chem. Soc.* **131**, 4499-4504 (2009).

[163] Panda, P., Ali, S., Lo, E., Chung, B. G., Hatton, T. A., Khademhosseini, A., and Doyle, P. S., "Stop-flow lithography to generate cell-laden microgel particles," *Lab Chip* **8**, 1056-1061 (2008).

[164] Tan, W. S., Lewis, C. L., Horelik, N. E., Pregibon, D. C., Doyle, P. S., and Yi, H. M., "Hierarchical assembly of viral nanotemplates with encoded microparticles via nucleic acid hybridization," *Langmuir* **24**, 12483-12488 (2008).

[165] Bong, K. W., Pregibon, D. C., and Doyle, P. S., "Lock release lithography for 3D and composite microparticles," *Lab Chip* **9**, 863-866 (2009).

[166] Bong, K. W., Bong, K. T., Pregibon, D. C., and Doyle, P. S., "Hydrodynamic focusing lithography," *Angew. Chem., Int. Ed.* **49**, 87-90 (2010).

[167] Bong, K. W., Xu, J., Kim, J., Chapin, S. C., Strano, M. S., Gleason, K. K., and Doyle, P. S., "Non-polydimethylsiloxane devices for oxygen-free flow lithography," *Nat. Commun.* In Press.

[168] Shepherd, R. F., Panda, P., Bao, Z., Sandhage, K. H., Hatton, T. A., Lewis, J. A., and Doyle, P. S., "Stop-flow lithography of colloidal, glass, and silicon microcomponents," *Adv. Mater.* **20**, 4734-4739 (2008).

[169] Kim, H., Ge, J., Kim, J., Choi, S., Lee, H., Lee, H., Park, W., Yin, Y., and Kwon, S., "Structural colour printing using a magnetically tunable and lithographically flexible photonic crystal," *Nat. Photonics* **3**, 534-540 (2009).

[170] Chung, S. E., Park, W., Shin, S., Lee, S. A., and Kwon, S., "Guided and fluidic self-assembly of microstuctures using railed microfluidic channels," *Nature Mater.* **7**, 581-587 (2008).

[171] Chung, S. E., Park, W., Park, H., Yu, K., Park, N., and Kwon, S., "Optofluidic maskless lithography system for real-time synthesis of photopolymerized microstructures in microfluidic channels," *Appl. Phys. Lett.* **91**, (2007).

[172] DeForest, C. A. and Anseth, K. S., "Cytocompatible click-based hydrogels with dynamically tunable properties through orthogonal photoconjugation and photocleavage reactions," *Nat. Chem.* **3**, 925-931 (2011).

[173] Anseth, K. S., Brannon-Peppas, L., and Bowman, C. N., "Mechanical properties of hydrogels and their experimental determination," *Biomaterials* **17**, 1647-1657 (1996).

[174] Pregibon, D. C., "Enabling technologies for multiplexed biomolecule analysis and cell sorting," *Ph.D. Thesis, Massachusetts Institute of Technology* (2008).

[175] Appleyard, D. C., Chapin, S. C., Srinivas, R. L., and Doyle, P. S., "Bar-coded hydrogel microparticles for protein detection: Synthesis, assay, and scanning," *Nat. Protocols* **6**, 1761-1774 (2011).

[176] Schopf, E. and Chen, Y., "Attomole DNA detection assay via rolling circle amplification and single molecule detection," *Anal. Biochem.* **397**, 115-117 (2010).

[177] Kohro-Kawata, J., Wener, M. H., and Mannik, M., "The effect of high salt concentration on detection of serum immune complexes and autoantibodies to C1q in patients with systemic lupus erythematosus," *J. Rheumatol* **29**, 84-89 (2002).

[178] Freshney, R., *Culture of animal cells: A manual of basic technique*, Alan R. Liss, Inc., New York, 117 (1987).

[179] Suh, S. K., Chapin, S. C., Hatton, T. A., and Doyle, P. S., "Synthesis of magnetic hydrogel microparticles for bioassays and tweezer manipulation in microwells," *Microfluid. Nanofluid.* In Press.

[180] Pregibon, D. C. and Doyle, P. S., "Optimization of encoded hydrogel particles for nucleic acid quantification," *Anal. Chem.* **81**, 4873-4881 (2009).

[181] Crosland-Taylor, P. J., "A device for counting small particles suspended in a fluid through a tube," *Nature* **171**, 37-38 (1953).

[182] Faivre, M., Abkarian, M., Bickraj, K., and Stone, H. A., "Geometrical focusing of cells in a microfluidic device: An approach to separate blood plasma," *Biorheology* **43**, 147-159 (2006).

[183] Halpern, D. and Secomb, T. W., "Viscous motion of disc-shaped particles through parallel-sided channels with near-minimal widths," *J. Fluid Mech.* **231**, 545-560 (1991).

[184] Halpern, D. and Secomb, T. W., "The squeezing of red blood cells through parallel-sided channels with near-minimal widths," *J. Fluid Mech.* **244**, 307-322 (1992).

[185] Fitz-Gerald, J. M., "Mechanics of red-cell motion through very narrow capillaries," *Proc. R. Soc. B* **174**, 193-227 (1969).

[186] Secomb, T. W. and Skalak, R., "A two-dimensional model for capillary flow of an asymmetric cell," *Microvasc. Res.* **24**, 194-203 (1982).

[187] Volinia, S., Calin, G. A., Liu, C. G., Ambs, S., Cimmino, A., Petrocca, F., Visone, R., Iorio, M., Roldo, C., Ferracin, M., Prueitt, R. L., Yanaihara, N., Lanza, G., Scarpa, A., Vecchione, A., Negrini, M., Harris, C. C., and Croce, C. M., "A microRNA expression signature of human solid tumors defines cancer gene targets," *Proc. Natl. Acad. Sci. USA* **103**, 2257-2261 (2006).

[188] Wark, A. W., Lee, H. J., and Corn, R. M., "Multiplexed detection methods for profiling microRNA expression in biological samples," *Angew. Chem., Int. Ed.* **47**, 644-652 (2008).

[189] Brunker, S. E., Cederquist, K. B., and Keating, C. D., "Metallic barcodes for multiplexed bioassays," *Nanomedicine* **2**, 695-710 (2007).

[190] Broder, G. R., Ranasinghe, R. T., She, J. K., Banu, S., Birtwell, S. W., Cavalli, G., Galitonov, G. S., Holmes, D., Martins, H. F. P., MacDonald, K. F., Neylon, C., Zheludev, N., Roach, P. L., and Morgan, H., "Diffractive micro bar codes for encoding of biomolecules in multiplexed assays," *Anal. Chem.* **80**, 1902-1909 (2008).

[191] Horan, P. K. and L.L. Wheeless, J., "Quantitative single cell analysis and sorting," *Science* **198**, 149-157 (1977).

[192] Chapin, S., Pregibon, D., and Doyle, P., "High-throughput flow alignment of barcoded hydrogel microparticles," *Lab Chip* **9**, 3100-3109 (2009).

[193] Brazas, R. M., Enos, J. M., Duzeski, J. L., Schifreen, R. S., and Watt, M. V., "Accuracy of microarray-based microRNA expression profiling using direct versus enzymatic labeling," *J. Mol. Diagn.* **8**, 671 (2006).

[194] Shingara, J., Keiger, K., Shelton, J., Laosinchai-Wolf, W., Powers, P., Conrad, R., Brown, D., and Labourier, E., "An optimized isolation and labeling platform for accurate microRNA expression profiling," *RNA* **11**, 1461-1470 (2005).

[195] Bullard, D. R. and Bowater, R. P., "Direct comparison of nick-joining activity of the nucleic acid ligases from bacteriophage T4," *Biochem. J.* **398**, 135-144 (2006).

[196] Cheng, Y., Zhang, X., Li, Z., Jiao, X., Wang, Y., and Zhang, Y., "Highly sensitive determination of microRNA using target-primed and branched rolling-circle amplification," *Angew. Chem., Int. Ed.* **48**, 3268-3272 (2009).

[197] Bloomston, M., Frankel, W. L., Petrocca, F., Volinia, S., Alder, H., Hagan, J. P., Liu, C. G., Bhatt, D., Taccioli, C., and Croce, C. M., "MicroRNA expression patterns to differentiate pancreatic adenocarcinoma from normal pancreas and chronic pancreatitis," *JAMA* **297**, 1901-1908 (2007).

[198] Calin, G. A. and Croce, C. M., "MicroRNA signatures in human cancer," *Nat. Rev. Cancer* **6**, 857-866 (2006).

[199] Yanaihara, N., Caplen, N., Bowman, E., Seike, M., Kumamoto, K., Yi, M., Stephens, R. M., Okamoto, A., Yokota, J., Tanaka, T., Calin, G. A., Liu, C. G., Croce, C. M., and Harris, C. C., "Unique microRNA molecular profiles in lung cancer diagnosis and prognosis," *Cancer Cell* **9**, 189-198 (2006).

[200] Takagi, T., Iio, A., Nakagawa, Y., Naoe, T., Tanigawa, N., and Akao, Y., "Decreased expression of microRNA-143 and -145 in human gastric cancers," *Oncol.* **77**, 12-21 (2009).

[201] Jiang, J., Lee, E. J., Gusev, Y., and Schmittgen, T. D., "Real-time expression profiling of microRNA precursors in human cancer cell lines," *Nuc. Acids Res.* **33**, 5394-5403 (2005).

[202] Lee, E. J., Baek, M., Gusev, Y., Brackett, D. J., Nuovo, G. J., and Schmittgen, T. D., "Systematic evaluation of microRNA processing patterns in tissues, cell lines, and tumors," *RNA* **14**, 35-42 (2008).

[203] Jiang, Q., Wang, Y., Hao, Y., Juan, L., Teng, M., Zhang, X., Li, M., Wang, G., and Liu, Y., "miR2Disease: A manually curated database for microRNA deregulation in human disease," *Nuc. Acids Res.* **37**, D98-D104 (2008).

[204] Zhou, Y., Huang, Q., Gao, J., Lu, J., Shen, X., and Fan, C., "A dumbbell probe-mediated rolling circle amplification strategy for highly sensitive microRNA detection," *Nuc. Acids Res.* **38**, e156 (2010).

[205] Chapin, S. C., Appleyard, D. C., Pregibon, D. C., and Doyle, P. S., "Rapid microRNA profiling on encoded gel microparticles," *Angew. Chem., Int. Ed.* **50**, 2289-2293 (2011).

[206] Lodes, M. J., Caraballo, M., Suciu, D., Munro, S., Kumar, A., and Anderson, B., "Detection of cancer with serum miRNAs on an oligonucleotide microarray," *PLoS ONE* **4**, e6229 (2009).

[207] Brase, J. C., Wuttig, D., Kuner, R., and Sültmann, H., "Serum microRNAs as non-invasive biomarkers for cancer," *Mol. Cancer* **9**, 306-314 (2010).

[208] Asaga, S., Kuo, C., Nguyen, T., Terpenning, M., Giuliano, A. E., and Hoon, D. S. B., "Direct serum assay for microRNA-21 concentrations in early and advanced breast cancer," *Clin. Chem. (Washington, DC, U.S.)* **57**, 84-91 (2011).

[209] Fang, S., Lee, H. J., Wark, A. W., and Corn, R. M., "Attomole microarray detection of microRNAs by nanoparticle-amplified SPR imaging measurements of surface polyadenylation reactions," *J. Am. Chem. Soc.* **128**, 14044-14046 (2006).

[210] Jonstrup, S. P., Koch, J., and Kjems, J., "A microRNA detection system based on padlock probes and rolling circle amplification," *RNA* **12**, 1747-1752 (2006).

[211] Li, N., Jablonowski, C., Jin, H., and Zhong, W., "Stand-alone rolling circle amplification combined with capillary electrophoresis for specific detection of small RNA," *Anal. Chem.* **81**, 4906-4913 (2009).

[212] Yao, B., Li, J., Huang, H., Sun, C., Wang, Z., Fan, Y., Chang, Q., Li, S., and Xi, J., "Quantitative analysis of zeptomole microRNAs based on isothermal ramification amplification," *RNA* **15**, 1787-1794 (2009).

[213] Blanco, L., Bernad, A., Lázaro, J. M., Martín, G., Garmendia, C., and Salas, M., "Highly efficient DNA synthesis by the phage phi29 DNA polymerase," *J. Biol. Chem.* **264**, 8935-8940 (1989).

[214] Appleyard, D. C., Chapin, S. C., and Doyle, P. S., "Multiplexed protein quantification with barcoded hydrogel microparticles," *Anal. Chem.* **83**, 193-199 (2011).

[215] Fire, A. and Xu, S., "Rolling replication of short DNA circles," *Proc. Natl. Acad. Sci. U.S.A.* **92**, 4641-4645 (1995).

[216] Liu, D., Daubendiek, S. L., Zillman, M. A., Ryan, K., and Kool, E. T., "Rolling circle DNA synthesis: Small circular oligonucleotides as efficient templates for DNA polymerase," *J. Am. Chem. Soc.* **118**, 1587-1594 (1996).

[217] Zhao, W., Ali, M. M., Brook, M. A., and Li, Y., "Rolling circle amplification: Applications in nanotechnology and biodetection with functional nucleic acids," *Angew. Chem., Int. Ed.* **47**, 6330-6337 (2008).

[218] Nallur, G., Luo, C., Fang, L., Cooley, S., Dave, V., Lambert, J., Kukanskis, K., Kingsmore, S., Lasken, R., and Schweitzer, B., "Signal amplification by rolling circle amplification on DNA microarrays," *Nuc. Acids. Res.* **29**, e118 (2001).

[219] Levicky, R. and Horgan, A., "Physiochemical perspectives on DNA microarray and biosensor technologies," *Trends Biotechnol.* **23**, 143-149P (2005).

[220] Yan, J., Song, S., Li, B., Zhang, Q., Huang, Q., Zhang, H., and Fan, C., "An on-nanoparticle rolling-circle amplification platform for ultrasensitive protein detection in biological fluids," *Small* **6**, 2520-2525 (2010).

[221] Lizardi, P. M., Huang, X., Zhu, Z., Bray-Ward, P., Thomas, D. C., and Ward, D. C., "Mutation detection and single-molecule counting using isothermal rolling-circle amplification," *Nat. Genet.* **19**, 225-232 (1998).

[222] Jarvius, J., Melin, J., Goransson, J., Stenberg, J., Fredriksson, S., Gonzalez-Rey, C., Bertilsson, S., and Nilsson, M., "Digital quantification using amplified single-molecule detection," *Nat. Methods* **3**, 725-727 (2006).

[223] Rissin, D. M., Kan, C. W., Campbell, T. G., Howes, S. C., Fournier, D. R., Song, L., Piech, T., Patel, P. P., Chang, L., Rivnak, A. J., Ferrell, E. P., Randall, J. D., Provuncher, G. K., Walt, D. R., and Duffy, D. C., "Single-molecule enzyme-linked immunosorbent assay detects serum proteins at subfemtomolar concentrations," *Nat. Biotechnol.* **28**, 595-599 (2010).

[224] Rissin, D. M., Fournier, D. R., Piech, T., Kan, C. W., Campbell, T. G., Song, L., Chang, L., Rivnak, A. J., Patel, P. P., Provuncher, G. K., Ferrell, E. P., Howes, S. C., Pink, B. A., Minnehan, K. A., Wilson, D. H., and Duffy, D. C., "Simultaneous

detection of single molecules and singulated ensembles of molecules enables immunoassays with broad dynamic range," *Anal. Chem.* **83**, 2279-2285 (2011).

[225] Petriv, O. I., Kuchenbauer, F., Delaney, A. D., Lecault, V., White, A., Kent, D., Marmolejo, L., Heuser, M., Berg, T., Copley, M., Ruschmann, J., Sekulovic, S., Benz, C., Kuroda, E., Ho, V., Antignano, F., Halim, T., Giambra, V., Krystal, G., Takei, C. J. F., Weng, A. P., Piret, J., Eaves, C., Marra, M. A., Humphries, R. K., and Hansen, C. L., "Comprehensive microRNA expression profiling of the hematopoietic hierarchy," *Proc. Natl. Acad. Sci. U.S.A.* **107**, 15443-15448 (2010).

[226] White, A. K., Vanlnsberghe, M., Petriv, O. I., Hamidi, M., Sikorski, D., Marra, M. A., Piret, J., Aparicio, S., and Hansen, C. L., "High-throughput microfluidic single-cell RT-qPCR," *Proc. Natl. Acad. Sci. U.S.A.* **108**, 13999-14004 (2011).

[227] Spiller, D. G., Wood, C. D., Rand, D. A., and White, M. R. H., "Measurement of single-cell dynamics," *Nature* **465**, 736-745 (2010).

[228] Kalisky, T. and Quake, S. R., "Single-cell genomics," *Nat. Meth.* **8**, 311-314 (2011).

[229] Chao, T. and Ros, A., "Microfluidic single-cell analysis of intracellular compounds," *J. R. Soc. Interface* **5**, S139-S150 (2008).

[230] Tay, S., Hughey, J. J., Lee, T. K., Lipniacki, T., Quake, S. R., and Covert, M. W., "Single-cell NF-κB dynamics reveal digital activation and analogue information processing," *Nature* **466**, 267-271 (2010).

[231] Lu, J. and Tsourkas, A., "Imaging individual microRNAs in single mammalian cells *in situ*," *Nuc. Acids Res.* **37**, e100 (2009).

[232] Chapin, S. C. and Doyle, P. S., "Ultrasensitive multiplexed microRNA quantification on encoded gel microparticles using rolling circle amplification," *Anal. Chem.* **83**, 7179-7185 (2011).

[233] Allawi, H. T., Dahlberg, J. E., Olson, S., Lund, E., Olson, M., Ma, W., Takova, T., Neri, B. P., and Lyamichev, V. I., "Quantitation of microRNAs using a modified Invader assay," *RNA* **10**, 1153-1161 (2004).

[234] Jen, C., Hsiao, J., and Maslov, N. A., "Single-cell chemical lysis on microfluidic chips with arrays of microwells," *Sensors* **12**, 347-358 (2012).

[235] http://www.eppendorf.com

[236] http://www.agilent.com

[237] Helgeson, M. E., Moran, S. E., An, H. Z., and Doyle, P. S., "Mesoporous organohydrogels from thermogelling photocrosslinkable nanoemulsions," *Nat. Mater.* **11**, 344-352 (2012).

[238] Lim, L. P., Lau, N. C., Weinstein, E. G., Abdelhakim, A., Yekta, S., Rhoades, M. W., Burge, C. B., and Bartel, D. P., "The microRNAs of *Caenorhabditis elegans*," *Genes & Dev.* **17**, 991-1008 (2003).

[239] Srinivas, R. L., Chapin, S. C., and Doyle, P. S., "Aptamer-functionalized microgel particles for protein detection," *Anal. Chem.* **83**, 9138-9145 (2011).

[240] Choi, N. W., Kim, J., Chapin, S. C., Duong, T., Donohue, E., Pandey, P., Broom, W., Hill, W. A., and Doyle, P. S., "Multiplexed detection of mRNA using porosity-tuned hydrogel microparticles," In Preparation.

[241] Choi, S. and Park, J. K., "Microfluidic system for dielectrophoretic separation based on a trapezoidal electrode array," *Lab Chip* **5**, 1161-1167 (2005).

[242] Makamba, H., Kim, J. H., Lim, K., Park, N., and Hahn, J. H., "Surface modification of poly(dimethylsiloxane) microchannels," *Electrophoresis* **24**, (2003).

[243] Brown, R. B. and Audet, J., "Current techniques for single-cell lysis," *J. R. Soc. Interface* **5**, S131-S138 (2008).

[244] Nichol, J. W., Koshy, S. T., Bae, H., Hwang, C. M., Yamanlar, S., and Khademhosseini, A., "Cell-laden microengineered gelatin methacrylate hydrogels," *Biomaterials* **31**, 5536-5544 (2010).

[245] Elmas, B., Onur, M. A., Senel, S., and Tuncel, A., "Temperature controlled RNA isolation by N-isopropylacrylamide-vinylphenyl boronic acid copolymer latex," *Colloid Polym. Sci.* **280**, 1137-1146 (2002).

[246] Longo, C., Patanarut, A., George, T., Bishop, B., Zhou, W., Fredolini, C., Ross, M. M., Espina, V., Pellacani, G., Petricoin, E. F., Liotta, L. A., and Luchini, A., "Core-shell hydrogel particles harvest, concentrate, and preserve labile low abundance biomarkers," *PLoS ONE* **4**, e4763 (2009).

[247] Venkatesan, B. M. and Bashir, R., "Nanopore sensors for nucleic acid analysis," *Nat. Nanotechnol.* **6**, 615-624 (2011).

[248] Gierlich, J., Gutsmiedl, K., Gramlich, P. M. E., Schmidt, A., Burley, G. A., and Carell, T., "Synthesis of highly modified DNA by a combination of PCR with alkyne-bearing triphosphates and click chemistry," *Chem.-Eur. J.* **13**, 9486-9494 (2007).

[249] El-Sagheer, A. H. and Brown, T., "Click chemistry with DNA," *Chem. Soc. Rev.* **39**, 1388-1405 (2010).

[250] Reiß, E., Holzel, R., and Bier, F. F., "Synthesis and stretching of rolling circle amplification products in a flow-through system," *Small* **5**, 2316-2322 (2009).

[251] Brockman, C., Kim, S. J., and Schroeder, C. M., "Direct observation of single flexible polymers using single stranded DNA," *Soft Matter* **7**, 8005-8012 (2011).

[252] Ponomarev, E. D., Veremeyko, T., and Barteneva, N. S., "Visualization and quantitation of the expression of microRNAs and their target genes in neuroblastoma single cells using imaging cytometry," *BMC Research Notes* **4**, 517 (2011).

[253] Mansfield, J. R., "Cellular context in epigenetics: Quantitative multicolor imaging and automated per-cell analysis of miRNAs and their putative targets," *Methods* **52**, 271-280 (2010).